Mechanisms and Effects of Heat Generation at the Tips of Dynamic Cracks and Notches in Metals

Thesis by
James Joseph Mason

In Partial Fulfillment of the Requirements
for the Degree of
Doctor of Philosophy

California Institute of Technology
Pasadena, CA 91125

1993
Submitted May 14, 1993

Acknowlegments

The completion of this work would certainly have been impossible without the help of my advisor, Prof. A.J. Rosakis. I am indebted to him for his support, advice and—sometimes much needed—encouragement throughout the completion of the work summarized here. There are always problems with performing experiments that are too mundane to be mentioned in a proper Doctoral Dissertation or that are simply unrelated to the report of scientific results. However, it is often these problems that are the most trying and difficult to overcome. I am grateful to Ares Rosakis for his availability and always reliable support when such problems arose.

Furthermore, this work could not have been completed without the friendship of several of my fellow graduate students. I am especially grateful to have entered the doctoral program at California Institute of Technology at the same time as Yiannis (John) Lambros, Philippe Geubelle and Guillaume Vendroux. Companionship and comradery were easy to come by in the company of these men. And many mutually helpful discussions were had between us. I would also like to recognize the help of Dr. Carl Shultheiz. His availability and willingness to share his experiences at CalTech often proved to be extremely timesaving during the progress of this work.

Lastly, I cannot overlook the contribution of my wife, Maria, throughout this sometimes trying experience. Her loving support and leadership in our life together have allowed me concentrate 100% of my abilities on the completion of this doctoral degree. Together we shall always enjoy the benefits of our work.

Abstract

A high-speed InSb infrared detector array and the method of Coherent Gradient Sensing (CGS) are used in several experimental configurations to explore the mechanisms and effects of heat generation in dynamic fracture and deformation.

First, the dependence of the measured dynamic crack tip temperature upon crack tip speed is investigated for cracks propagating dynamically in AISI 4340 carbon steel. Then, the dynamic crack tip temperature in a titanium alloy (Ti-10V-2Fe-3Al) is measured in order to examine the role of material parameters in determining the crack tip temperature at different crack growth speeds. It is seen that the crack tip temperature increases when crack tip velocities are increased from 600 m/s to 900 m/s in 4340 steel. The extent of the active plastic zone at the surface of the specimen, however, decreases with increasing crack velocity. When the results for temperature measurements in steel are compared with those for titanium, it is seen that the material parameters that are most important are the dynamic yield strength, which determines the amount of plasticity, and the heat capacity of the material. Conductivity has little effect.

Next, the nature of hyperbolic heat conduction at the tip of a dynamic crack is investigated. A mathematical model is developed to predict the temperature field around a dynamically propagating crack tip for a material that follows a hyperbolic heat conduction law. A Green's function for the governing partial differential equation is derived. The model is solved for a variety of experimental conditions by numerical integration of the Green's function. Various possible effects of hyperbolic heat conduction around a crack tip are explored. The model is then used to simulate the experimental conditions typically observed in dynamic fracture. Because conduction is minimal around the dynamically propagating crack tip, no effects of hyperbolic heat conduction are observed. It is also observed that the temperature field around the dynamic crack tip is adiabatic.

Since adiabatic conditions are observed around a propagating crack tip, an important parameter which governs the distribution and intensity of crack tip heating is the fraction of plastic work rate converted to heat, β. For this investigation β is not treated as a mere parameter, the possibility of the existence of a constitutive relationship between this parameter and strain at high strain-rates is investigated using the Kolsky bar as a loading apparatus. It is found that the conversion of plastic work to heat at high strain-rates is similar to that at low strain rates for aluminum and for steel and that β remains a constant independent of strain at high strains for both these materials. For rate sensitive titanium, β is observed to be a function of strain possibly due to twinning deformation.

It is known that heat generation can lead to the formation of shear bands especially in dynamic fracture experiments. The formation of a shear band at the tip of a notch or crack in C-300 steel is examined using the method of CGS. First, the CGS method is used to verify a model of the notch tip stress intensity factor, K_{II}, as a function of time. Good agreement is found between the experimental measurement of K_{II} and the predicted value for PMMA impacted at 5 m/s. Then the method is used to investigate the formation of shear bands at the tip of a notch under the same conditions. A Dugdale crack model is used to interpret the results, and it is seen that the shear stress decreases from 1.6 GPa to 1.3 GPa as the shear band propagates. This result is in good agreement with measurements made using the Kolsky bar.

Contents

Part I:

Mechanisms of Plastic Heating at the Tip of a Dynamic Crack and the Resultant Temperature Rise

Part II:

An Effect of Heating at a Dynamic Crack Tip; The Formation of a Shear Instability

CHAPTER 1

Preliminaries

1.1 Motivation

In dynamic fracture mechanics it is often postulated that for most structural materials a unique relationship exists between the critical crack tip driving force required for crack growth, K_{Ic}^{d}, and the crack growth velocity, $\dot{a}$. (Here, a is the crack length and the dot implies differentiation with respect to time.) This relationship is considered to be a "material property" such that by using it in an engineering problem with a specific driving force, one may solve the equation of motion for the crack tip and produce a quantitative prediction of the crack length as a function of time. (Freund, 1990) Relationships between K_{Ic}^{d} and $\dot{a}$ have been examined experimentally as well as theoretically, and a typical example of an experimentally determined relationship can be seen in Figure 1.1. The general shape of the curve shows a flat region at low velocities where the crack tip driving force is relatively independent of velocity. Accelerating the crack when it is propagating in this regime requires only a small change in driving force, K_{I}^{d}. In contrast, at higher velocities, the curve exhibits a steeply rising section where the driving force is highly sensitive to changes in velocity, and a significant increase in crack velocity requires a hefty increase in the driving force.

This general behavior can be qualitatively modeled by implementing either elastic or plastic deformation constitutive laws for the material at the crack tip. The steep rise in the curve is then attributed to the inertia of the material at the crack tip. (Freund and Douglas, 1982; Freund, 1990 and Deng and Rosakis, 1990) However, the predicted maximum attainable crack speed for these models is too high unless some broad

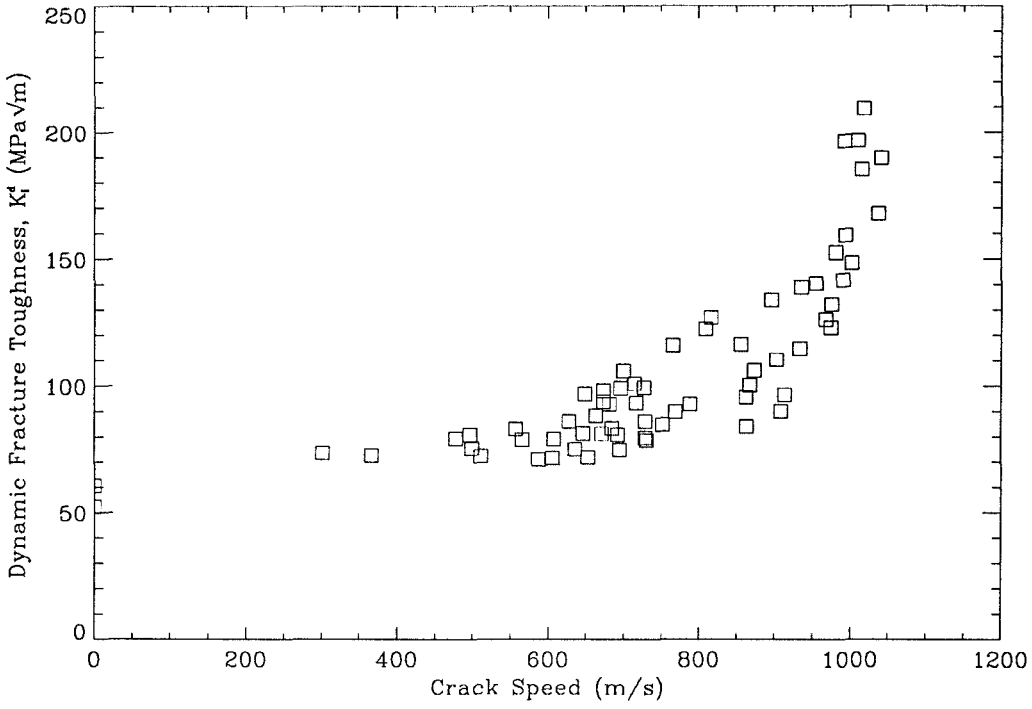

FIGURE 1.1 The dynamic fracture toughness of 4340 steel as reported by Zehnder and Rosakis (1990)

assumptions are made about the mechanisms of the material failure at the dynamic crack tip in the form of a "growth criterion." (Freund and Douglas, 1982) Usually large amounts of plasticity at the crack tip are allowed in order for the inertial model to match experimental data. As a result, there is some question as to whether thermal softening might be an important part of the observed behavior through its effect upon the "growth criterion." It is known that plastic deformation occurs at the crack tip in ductile metals during dynamic fracture and that the same deformation leads to the generation of heat. Consequently, a significant temperature rise can occur at a dynamically propagating crack tip for high velocities causing the crack tip material to soften and become "locally" more ductile than it is at lower velocities. The greater ductility would result in more plasticity and an increase in inertial resistance to crack propagation at the crack tip.

Table 1.1

Some Analytical and Numerical Predictions of the Temperature Rise at the Tip of a Dynamically Propagating Crack

Reference	Material	Crack Speed (m/s)	Maximum Temperature (°C)
Rice and Levy, 1969	Steel	900	1400
	Titanium	900	>10,000
Kuang and Atluri, 1985	Steel	762	700
Sung and Achenbach, 1987	Steel	300	700
Douglas and Mair, 1987	Steel	1500	1
	Titanium	1500	50
Malali, 1988	Steel	1500	528
	Titanium	1500	11,500
Krishna Kumar et al., 1991	Steel	320-1600	150-400

In order to asses the role of thermal softening in dynamic crack propagation, it is obviously necessary to examine the magnitude and nature of the temperature field around the a dynamically propagating crack tip. In fact, several authors *have* attempted to predict the temperature rise at the tip of a dynamically propagating crack, and a brief summary of some of their results may be found in Table 1.1. It is seen that the overall prediction of temperature rise can vary dramatically depending upon the material properties and the assumptions of the model. Experimental measurement of the actual temperature rise provides better illumination. Zehnder and Rosakis (1991) report the experimentally measured temperature field for 4340 steel propagating at 900 m/s. The maximum temperature reported by these authors is 500°C. However, their work did not investigate the role of material parameters and the effect of crack tip velocity upon the temperature field.

In addition to crack tip temperature field measurements, true understanding of the crack tip material deformation and resultant temperature rise requires some knowledge of the mechanics of the conversion of plastic work to heat at the tip. In the predictions reported in Table 1.1, it is often assumed that a fixed percentage of plastic work is converted to heat during all stages of deformation. However, it has also been reported elsewhere that the amount of plastic work converted to heat actually depends upon strain and, possibly, strain rate. Although much work has been performed on the understanding of the conversion of plastic work to heat at low strain rates (Bever et al., 1973) not much has been reported about the same phenomenon at high strain rates. At a crack tip strain rates can be as high as 10^5, (Zehnder and Rosakis, 1991) and it is clear that some investigations of the conversion of plastic work to heat at high strain rates would be highly applicable to the analysis of the dynamic crack tip heating problem.

In contrast, another vein of interest in crack tip temperature fields is predicated by knowledge that large, adiabatic temperature rises during dynamic-plastic deformation *can* lead to unstable deformation processes that, otherwise, would not be expected. Duffy (1984), for example, has observed the early onset of shear localization in dynamic torsion experiments. This effect is widely attributed to the effects of temperature rise, i.e., thermal softening, during dynamic plastic deformation. (*Mechanics of Materials,* 1993) It is suspected that similar effects may be occurring in dynamic fracture. In one case in particular (Kalthoff, 1987), it seems that dynamic failure mode selection may depend entirely upon the rate of loading and the competition between thermal softening effects and strain or strain rate hardening effects (Lee, 1990). Experimental investigation into this phenomenon would benefit from temperature measurement and full field deformation measurements at the crack tip.

It is intended that this work be an accurate representation of experimental inves-

tigations into the issues discussed up to this point. Although some lengthy theoretical developments are available in these area, it is important to complement such work with experimental investigation in hopes of properly indicating the critical parameters or dominant mechanisms in action. Thus, ideally, the current understanding of such a phenomenon can be either verified, enhanced or disqualified.

1.2 Experimental Methods

A brief summary and brief historical development of the experimental methods employed are included here in order to familiarize the reader with the nature of the work contained within this thesis.

Zehnder and Rosakis (1991) used an InSb infrared detector array, shown in Figure 1.2, to measure crack tip temperature fields in 4340 steel, and the same method is used here. This method has been used and developed by several authors in the past. Most notably, Duffy (1984) used a very similar arrangement during investigations of shear localization in torsional Kolsky bar experiments. The primary feature of the present system is that it utilizes reflecting lenses to focus the infrared image of the object on the detectors. First indication of such a focussed system may be found in Moss and Pond (1975). Before that several authors used unfocussed IR detectors, most notably in the study of visco-elastic fracture, to produce measurements of maximum temperature during dynamic, low-speed fracture (Fuller et al., 1975). Details of the workings of the temperature measurement system may be found in Chapter 2. It suffices to say that a calibration procedure is used to correlate the output voltage of the detectors to a given temperature. The calibration makes knowledge of the intimate details of the infrared radiation emission and transmission procedures unnecessary. Stated simply, a carefully measured, material specific voltage is assigned to a carefully, yet independently, measured temperature for a full range of possible experimental temperatures for every material studied. Conversion of the voltage to temperature is then performed using the

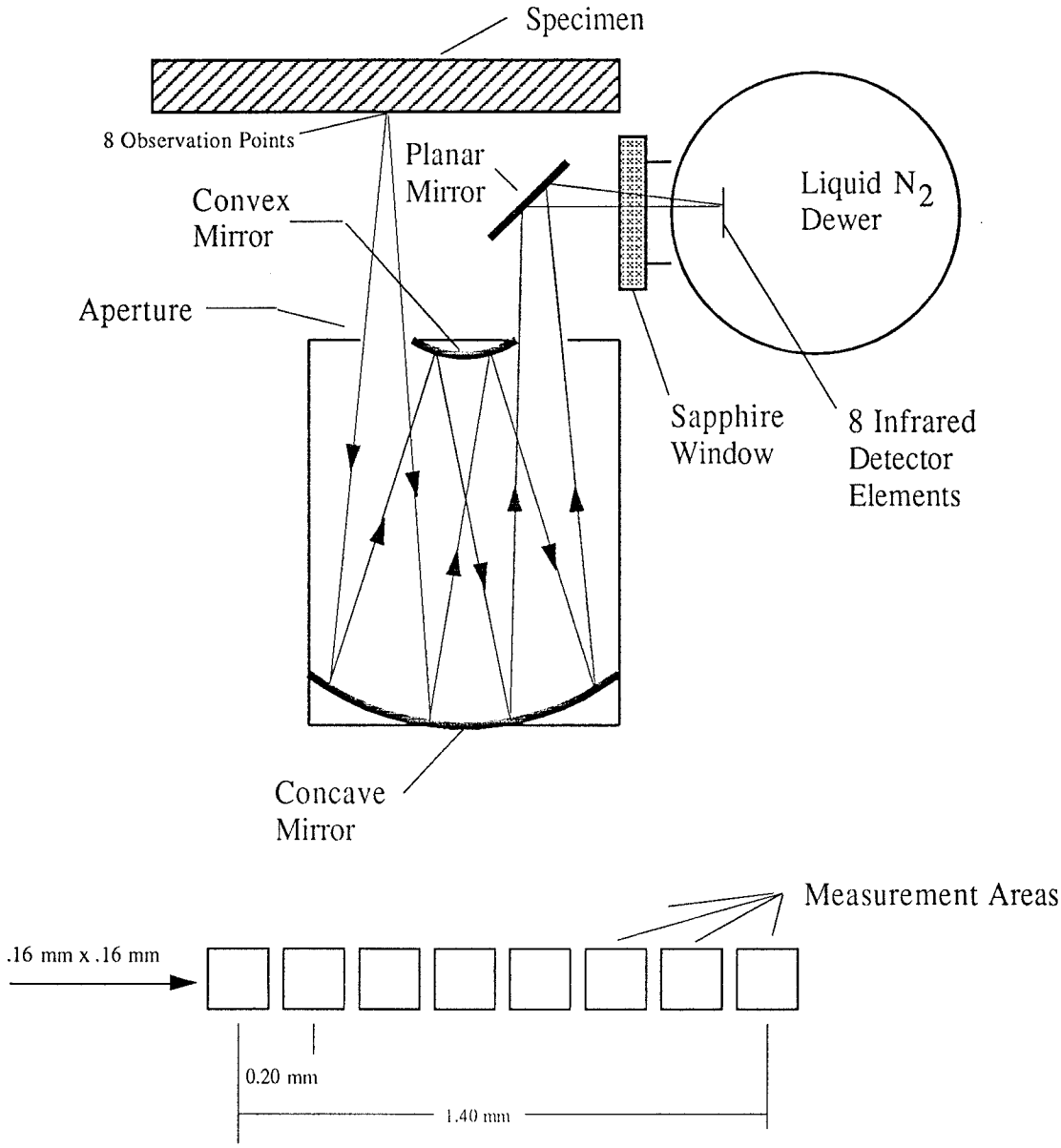

FIGURE 1.2 A schematic representation of the InSb infrared detector array and focussing system used to measure temperature.

calibration curve as a reference.

In Chapter 4 a Kolsky bar is used to measure high strain-rate behavior of materials. This apparatus is well known and quite well documented. Originally introduced by Kolsky (1949), it has now reached wide use and a review of its operation may be found in the *Metals Handbook* (Follansbee, 1985).

In Part II of this thesis temperature measurements are combined with deformation measurement during high-speed dynamic failure in order to produce a better understanding of the formation of shear localizations at a dynamic crack or notch tip. There are several methods by which to measure dynamic crack tip deformations—the most common of these are discussed in Chapter 5—however, the coherent gradient sensor (CGS) is used here. This method employs a simple interferometer to measure the gradient of hydrostatic stress around the crack or notch tip. Correlations are then made between the fringe pattern and the expected deformation field. The system was only recently introduced by Tippur et al. (1989), but it has a number of advantages over the usual methods as discussed in detail in Chapter 5. (See Rosakis, 1993.) A complete explanation of the working principle of CGS can be found in the same chapter.

1.3 Organization

It is the purpose of this treatise to investigate the cause, the nature and the effects of the temperature rise at the tip of a dynamic crack. In the interest of clarity, a dynamic crack is defined here following Freund's (1990) definition of the field of dynamic fracture mechanics:

> "Dynamic fracture mechanics is the subfield of fracture mechanics concerned with fracture phenomena for which the role of material inertia becomes significant."

Likewise, a dynamic crack shall be any crack "for which the role of material inertia becomes significant." This implies that the term "dynamic crack" may describe either a

stationary crack loaded by stress waves or a crack propagating at a significant fraction of the material Rayleigh wave speed, c_R i.e. $0.3c_r < \dot{a} < 0.6c_r$. Examples of both of these types of dynamic cracks are examined here, and the term "dynamic crack" will be used in reference to both.

The presentation of the work is organized in the following way.

1.3.1 Part I

In the first chapter of this work investigations into the effects of crack tip velocity and material parameters upon the maximum temperature and the temperature field around the tip of a dynamic crack are reported. A difference is found between the temperature fields around the crack tips propagating at 900 m/s and 600 m/s in 4340 steel. And, some investigation into the temperature fields around a crack propagating in a titanium alloy are reported. Discussion of the salient features of this work are contained within the Chapter.

During the completion and analysis of the results reported in Chapter 1, it was suggested in the literature that the temperature field around a dynamically propagating crack tip might demonstrate some effects of a secondary heat conduction law (Tzou 1990). In Chapter 2 an investigation into the possible effects of "hyperbolic heat conduction" around a dynamically propagating crack tip is reported. It was necessary to derive the travelling point source solution of the hyperbolic heat conduction equation before any report of possible effects of this type of heat conduction could be analyzed. It was thought that an observed difference between the temperature fields around the crack tips propagating at 900 m/s and 600 m/s in 4340 steel (as reported in Chapter 1) might be due to hyperbolic heat conduction. However, as demonstrated in Chapter 2, it easy to show that this is not true.

Throughout Chapters 1 and 2 it is assumed that 90% of plastic work is converted to heat during all phases of deformation. However, it is known that this simplifying

assumption is not, in general, valid at low strain-rates (Bever et al., 1973) and at high strain-rates virtually no conclusive investigations have been performed. Therefore, in Chapter 3 an investigation into the conversion of plastic work to heat at high strain-rates is reported. The work explores a new method by which to measure the rate of conversion of plastic work to heat. This method uses both the IR detector array shown in Figure 1.2 and the Kolsky bar. Since the deformation occurs over very short times in the Kolsky bar, no time is allowed for conductive cooling—this point is verified both through models and experimental results—and the analysis of the results is greatly simplified making it rather trivial to extract information about the rate of conversion of plastic work to heat at high strain-rates.

1.3.2 Part II

In Part I the investigation is aimed at reporting the nature and the cause of the temperature rise at a dynamic crack tip. In Part II the focus of the work changes to explore the effects of such a temperature rise. Namely, it is of interest to examine the effect of thermal softening at the tip of a dynamically loaded crack upon failure mode selection. Recently, Kalthoff (1987) has reported that when a pre-notched steel plate is loaded asymmetrically and dynamically in mode-II type deformation, the resulting failure growth path varies with impact velocity. In some cases the failure behaves following a maximum hoop stress type criterion and in other cases the failure is better described by a maximum shear stress failure criterion. This phenomenon is examined here in two stages; first CGS is used in transmission on PMMA specimens to examine the nature of the elastic deformation field at the crack tip, then CGS is used in reflection of steel plates to examine the deformation field around a shear band emanating from a dynamically loaded pre-notch or pre-crack.

Because CGS is a new method there is some concern about the validity of using it in a dynamic mixed-mode deformation situation. Consequently, it is necessary to

provide certain proof that the method can be used under such conditions. In Chapter 5 an investigation into the feasibility and validity of using the coherent gradient sensor on the pre-notched geometry of Kalthoff was preformed. High-speed photography was used to record the interferograms at short time intervals, and, thus, examine the time dependence of the crack tip deformation field. The measurements made with CGS were compared to an elastic solution for the crack tip deformation field for a model material, PMMA (Lee, 1990).

In Chapter 6 the method of CGS was used to produce deformation information for the phenomenon reported by Kalthoff (1987). An air gun is used to asymmetrically impact a thin steel pre-notched plate on its edge. Again, high-speed photography and CGS are used to record the time evolution of the crack tip deformation field on one side of the plate. The deformation field fringe patterns are interpreted using a Dugdale mode-II model resulting in measurements of the time histories of shear band length and the average shear stress on the shear band. The measured shear stress is compared to the measured shear stress for shear bands formed in the Kolsky bar.

References

1. M.B. Bever, D.L. Holt and A.L. Titchener (1973), The stored energy of cold work, *Prog. Mat. Sci.*, **17,** 1

2. X. Deng and A.J. Rosakis (1991), Dynamic crack propagation in elastic-perfectly plastic solids under plane stress conditions, *J. Mech. Phys. Sol.*, **39,** no. 5, 683

3. A.S. Douglas and H.U. Mair (1987), The temperature field surrounding a dynamically propagating mode-III crack, *Scr. Met.*, **21,** 479

4. J. Duffy (1984), Temperature measurements during the formation of shear bands in a structural steel, in: G.J. Dvorak and R.T. Shield, eds., *Mechanics of Material Behavior,* Elsevier Science Pub. B.V., Amsterdam, 75

5. P.S. Follansbee (1985), The split Hopkinson bar, *Metals Handbook; 9th Edition,* American Society for Metals, Metals Park, OH, **8,** 198

6. L.B. Freund and A.S. Douglas (1982), The influence of inertia on elastic-plastic antiplane shear crack growth, *J. Mech. Phys. Sol.*, **30,** 59

7. L.B. Freund (1990), *Dynamic Fracture Mechanics,* Cambridge University Press, New York, NY

8. K.N.G. Fuller, P.G. Fox and J.E. Field, The temperature rise at the tip of fast moving cracks in glassy polymers, *Proc. R. Soc. Lond. A,* **341,** 537

9. J.F. Kalthoff (1987), Shadow optical analysis of dynamic shear fracture, *SPIE Vol. 814, Photomechanics and Speckle Metrology,* 531

10. R. Krishna Kumar, R. Narasimhan and O. Prabhakar (1991), Temperature rise in a viscoplastic material during dynamic crack growth, *Int. J. Fracture,* **48,** 23

11. H. Kolsky (1949), An investigation of the mechanical properties of materials at very high rates of loading, *Proc. Royal Soc. B,* **62,** 676

12. Z.-B. Kuang and S. Atluri (1985), Temperature field due to a moving heat source: a moving mesh finite element analysis, *J. Appl. Mech.*, **52,** 277

13. Y.J. Lee (1990), *Problems associated with dynamic fracture under high strain-rate loading,* Ph.D. Thesis, Division of Engineering, Brown University, Providence, RI

14. P.N. Malali (1988), *Thermal fields generated by dynamic mode-III fracture in ductile materials,* M.S. Thesis, The Johns Hopkins University, Baltimore, MD

15. *Mechanics of Materials,* (1993), Shear Band Special Issue, June, 1993.

16. G.L. Moss and R.B. Pond (1975), Inhomogeneous thermal changes in copper during plastic elongation, *Met. Trans. A,* **6A,** 1223

17. J.R. Rice and N. Levy (1969), Local heating by plastic deformation at a crack tip, in: A.S. Argon ed., *Physics of Strength and Plasticity,* M.I.T. Press, Cambridge, MA, 277

18. A.J. Rosakis (1993), Two optical techniques sensitive to gradients of optical path difference: The method of caustics and the coherent gradient sensor (CGS), in *Experimental Techniques in Fractures III,* J.S. Epstein, Ed., Society for Experimental Mechanics, Inc., Bethel, CT, Ch. 10

19. J.C. Sung and J.D. Achenbach (1987), Temperature at a propagating crack tip in a viscoplastic material, *J. Thermal Stresses,* **10,** 243

20. H.V. Tippur, S. Krshnaswamy and A.J. Rosakis (1989), A coherent gradient sensor for crack tip deformation measurements: analysis and experimental results, Caltech SM Report 89-1, *see Int. J. Fracture,* **48,** 193

21. D.Y. Tzou (1990), Thermal shock waves induced by a moving crack, *J. Heat Transfer,* **112,** 21

22. A.T. Zehnder and A.J. Rosakis (1990), Dynamic Fracture Initiation and Propagation in 4340 Steel Under Impact Loading, *Int. J. Fracture,* **43,** 271

Part I:

Mechanisms of Plastic Heating at the Tip of a Dynamic Crack and the Resultant Temperature Rise

CHAPTER 2

On the Dependence of the Dynamic Crack Tip Temperature Fields in Metals Upon Crack Tip Velocity and Material Parameters

Overview

Although various approximations have been used to analytically predict the temperature rise at a dynamic crack tip and its relation to the crack tip velocity or the material properties, few experimental investigations of these effects exist. Here, the method of using a high-speed infrared detector array to measure the temperature distribution at the tip of a dynamically propagating crack tip is outlined, and the results from a number of experiments on different metal alloys are reviewed. First the effect of crack tip velocity is reviewed, and it is seen that the maximum temperature increases with increasing velocity and that a significant change in the geometry of the temperature distribution occurs at higher velocities in steel due to the opening of the crack faces behind the crack tip. Next, the effect of thermal properties is examined, and it is seen that, due to adiabatic conditions at the crack tip, changes in thermal conductivity do not significantly affect the temperature field. Changes in density and heat capacity are more likely to produce significant differences in temperature than changes in thermal conductivity. Finally, the effect of heat upon the crack tip deformation is reviewed, and it is seen that the generation of heat at the crack tip in steel leads to the formation of a shear band at 45° to the surface of the specimen. In titanium, no conclusive evidence of shear band formation is seen.

2.1 Introduction

It is known that in ductile metals plasticity ahead of a dynamically propagating or dynamically loaded crack can lead to the generation of heat resulting in a significant temperature rise at the crack tip. Such increases in thermal energy can lead to changes in fracture toughness, changes in fracture mode and instabilities in the resulting deformation. For example, it has been observed that heat generated in dynamic deformations can result in the decomposition of thermally unstable materials(Fox and Sonria-Ruiz, 1970) and localized melting in titanium alloys(Bryant et al., (1986). If the conditions of the deformation are approximated by neglecting heat conduction (by assuming that adiabatic heating conditions prevail) and by neglecting the thermo-elastic effect, the temperature rise due to dynamic plasticity is given quite simply by

$$\Delta T(t) = \frac{1}{\rho c_p} \int_{-\infty}^{t} \beta \sigma_{ij}(\tau) \dot{\epsilon}_{ij}^{p}(\tau) d\tau \tag{2.1}$$

where $\Delta T(t)$ is the temperature rise, β is the fraction of work converted to heat—roughly .85-1.00 (Taylor and Quinney, 1934; Bever et al., 1973)—ρ is the density (assumed independent of temperature), c_p is the specific heat (also assumed independent of temperature), and σ_{ij} and $\dot{\epsilon}_{ij}^{p}$ are the Cartesian stress and plastic strain-rate tensor components. The temperature field in this case corresponds exactly with the plastic deformation field; when the plastic work density is higher the temperature is higher, and there is no temperature rise at a point if no plasticity occurs there.

While the assumption of adiabatic heating and the negligence of the thermo-elastic effect may significantly simplify the problem of calculating the temperature rise in dynamic deformation experiments, the conduction of heat is not completely absent in any realistic situation and elasticity is always present. If the effects of heat conduction and thermo-elasticity are included in the analysis, the standard heat (or diffusion) equation is invariably invoked,

$$\alpha \nabla^2 T - \frac{\partial T}{\partial t} = -\frac{\dot{W}^{p}}{\rho c_p} + \frac{\kappa}{\rho c_p} \frac{E}{(1-2\nu)} T_o \dot{\epsilon}_{kk}^{e} \tag{2.2a}$$

where $\alpha = k/\rho c_p$, k is the thermal conductivity,

$$\dot{W}^{vp} = \beta \sigma_{ij} \dot{\epsilon}^p_{ij}, \tag{2.2b}$$

T_o is the initial, ambient temperature, κ is the thermal expansion coefficient, E is Young's modulus, ν is Poisson's ratio, and $\dot{\epsilon}^e_{kk}$ is the rate of elastic dilatation. On the right-hand side of this equation are two terms characterizing two sources of heat in a deformation; the first term characterizes heat generated by plastic deformation (Taylor and Quinney, 1934: Bever et al., 1973) while the second term characterizes thermo-elastic cooling due to elastic dilatation (Sneddon and Berry, 1958). The solution of this coupled heat equation is greatly dependent upon the geometry of the problem at hand. For a crack of length a, propagating at a constant velocity, $\dot{a}$, it is beneficial to use a coordinate system that is translating with the crack tip. This results in a reformulation of Eq (2.2a);

$$\alpha \nabla^2 T + \dot{a} \frac{\partial T}{\partial x_1} = -\frac{\dot{W}^{vp}}{\rho c_p} \tag{2.3}$$

where thermo-elastic effects have been neglected, x_1 is the coordinate parallel to the crack faces and x_2 is perpendicular to the crack faces with the origin at the crack tip. The solution of Eq (2.3) for a point source of heat in two dimensions is given by Carslaw and Jaeger (1959) as

$$T_p(x_1, x_2) = \frac{\dot{Q}}{2\pi k} \exp\left[-\frac{\dot{a} x_1}{2\alpha}\right] K_0\left(\frac{\dot{a} r}{2\alpha}\right) \tag{2.4}$$

where $r = \sqrt{x_1^2 + x_2^2}$ and K_0 is the modified Bessel's function of the zeroth order. To predict the temperature field around a propagating crack tip the point source solution is used as a Green's function to be integrated over the area of the plastic work zone, A_p. Assuming the plastic work zone is self-similar throughout the thickness of the specimen and letting $\dot{Q} = \dot{W}^{vp} d\xi_1 d\xi_2$, the temperature field due to a experimental plastic zone is given by

$$T(x_1, x_2) = \int_{A_p} T_p(x_1 - \xi_1, x_2 - \xi_2) \dot{W}^{vp}(\xi_1, \xi_2) d\xi_1 d\xi_2. \tag{2.5}$$

Because of the logarithmic singularity of the modified Bessel's function at $r = 0$, the solution given by Eq (2.5) is finite and well behaved. Note that the assumption of a through-thickness, self-similar plastic work zone is rarely true where experimental temperature measurements are made—at the surface—due to the stress free surface boundary condition. Also note that knowledge of the active plastic zone size and shape, $\dot{W}^p(x_1, x_2)$. is required in Eq (2.5). Exactly determining this function in closed form for most real materials is virtually impossible. Approximations are used, or numerical calculation are substituted.

In order to apply Eq (2.1) or Eq (2.5) to known problems—that is, in order to exactly determine the extent of heating and the shape of a temperature field for known dynamic loading—a constitutive equation is required to specify a relation between stress, σ_{ij}, temperature, T, strain, ϵ_{ij}, and strain-rate $\dot{\epsilon}_{ij}$. This constitutive law would be used in Eq (2.2b) in conjunction with Eqs (2.1) or (2.5) to find the temperature field solution. Specifically lacking in the studies of dynamic deformation and heat generation are investigations of the constitutive behavior of materials. The dependence of stress upon temperature is not easily quantified; it is known that the rate of heating can have significant effects making it experimentally difficult to test at high temperatures. Also, the dependence of stress upon strain and temperature is associated with the history of temperature and strain as well as their current value. (It is well known that thermo-mechanical treatment can drastically alter the response of the material.) Furthermore, in dynamic testing arrangements such as the split Hopkinson bar (Follansbee, 1985) or plate impact tests (Clifton and Klopp, 1985), where dynamic constitutive laws are usually investigated experimentally, the temperature is not known and, in fact, effects attributed to a change in strain-rate could very well be due to heating. This leaves an investigator with little hope of precisely modelling the temperature field in most experimental situations. Theorists are forced to *assume* a constitutive relation, usually

a general one to incorporate most possibilities, and produce results for purely theoretical materials. Fortunately, for metals some common characteristics may be included in the constitutive law to qualitatively reproduce experimental behavior. First, most metals work-harden; with increasing plastic strain the resistance of the material to further plastic strain increases. Second, many metals strain-rate harden; increasing the plastic strain-rate results in increased resistance to further plastic straining. And, lastly, most metals thermally soften; increasing the temperature results in a decrease in the resistance to further plastic straining.

A number of theoretical investigations have taken the approach outlined above by directly assuming a constitutive law or by assuming a shape and size for the dynamic plastic zone at a crack tip. In most calculations the emphasis is placed upon calculating the maximum temperature so that it can be ascertained as to whether heating effects are important. Decoupled mechanical and thermal fields are usually evaluated. A summary can be found in Table 1.1. It should be noted that there is a sensitivity of the maximum temperature to the shape of the active plastic zone in the above calculations. By changing the plastic work rate distribution large differences in the maximum temperature may be induced. However, it suffices to say that temperature rises at the crack tip are expected to be significant.

Weichert and Schönert (1974, 1978a, and 1978b) have produced the temperature fields, and not just the maximum temperature, for square plastic work zones, as well as circles, of constant intensity. They predict temperatures rises of 3000°C for brittle materials such as quartz and glass by using a direct numerical integration technique to evaluate Eq (2.5). For the case of a propagating crack in metals the theoretical temperature field calculated by the same method for an experimental approximation of the plastic work zone (Mason and Rosakis, 1992) is shown in Fig 2.1. Notice that the contours of constant temperature extend straight back from the theoretical plastic

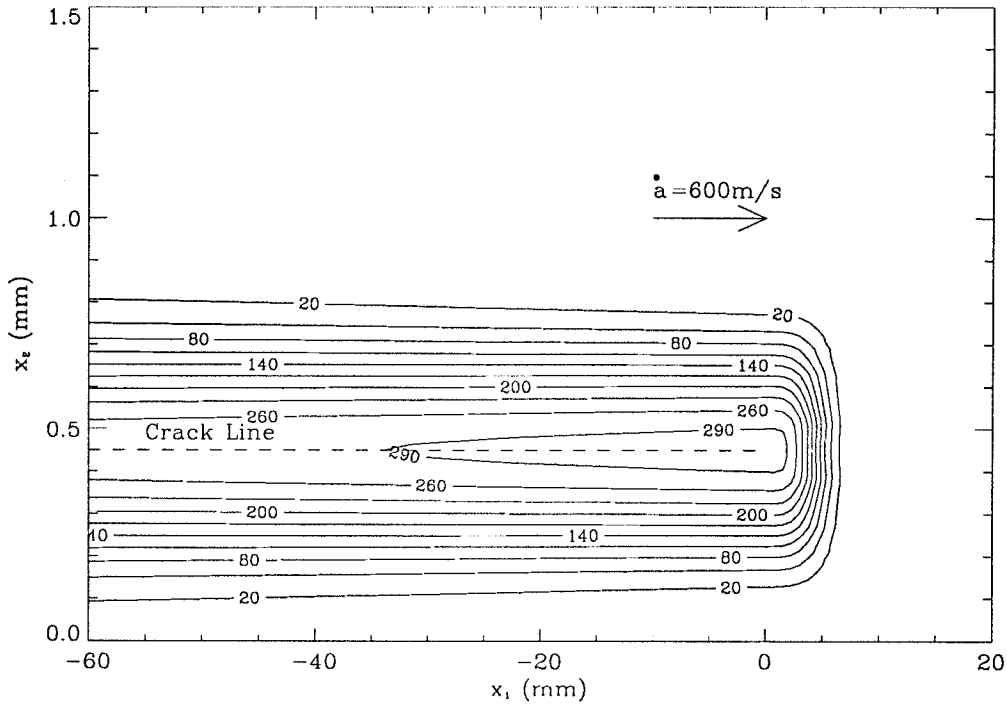

FIGURE 2.1 Theoretical calculation of the temperature field around a propagating crack tip in steel (Mason and Rosakis, 1992). A convolution of the the form in Eq (2.5) is used in conjunction with an approximation to the experimentally measured plastic work zone shown in Figs 6 and 7.

zone eventually curving toward the negative x_1 axis some distance behind the crack tip. This solution differs from the adiabatic solution in that the temperature is forced to zero at $r = \infty$ due to the boundary conditions of the point source solution in Eq (2.4).

There has been some suggestion that hyperbolic heat conduction may play a factor when crack speeds become significant with respect to the shear wave speed in the material (Tzou, 1990a and 1990b). However, closer examination shows that the simplified theory of hyperbolic heat conduction produces the same prediction as seen in Fig 2.1 for typical experimental conditions and crack speeds below the wave speed of heat propagation. When the crack speed is above the wave speed of heat propagation hyperbolic heat conduction theory predicts a temperature field that is drastically different than the experimentally observed fields (Mason and Rosakis, 1992).

While most of the investigations mentioned above include work hardening in the constitutive equation, few include strain-rate hardening or visco-plasticity, and none include thermal softening. It is thermal softening that commonly produces instabilities and anomalous behavior in dynamic plasticity experiments. As in a standard uniaxial tension test where geometric softening (due to the reduction in area of the test sample) competes with the inherent work hardening of the material until an instability, a neck, results, in dynamic tests thermal softening competes with work hardening and strain-rate hardening. In a dynamic plasticity test the generation of heat, which increases the temperature, T, can increase the amount of softening until an instability occurs resulting in the localization of the deformation to a single plane and the formation of a shear band. Adiabatic shear band formation has been observed for decades; for a review of the subject see Hutchinson (1984). In a torsional split Hopkinson bar experiment, Duffy and coworkers (Marchand and Duffy, 1988; Hartley et al., 1987; and Duffy 1984) and Giovanola (1988a and 1988b) were able to form shear bands in pure shear on several steels. They observed two stages of shear and temperature localization. First, localization by means of a thermal instability model is observed. This localization is due to the competition between thermal softening and strain or strain-rate hardening. Next, localization occurs on a smaller scale related to microvoid formation and coalescence. Using infrared detectors, temperatures as high as 450°C have been measured in the shear bands (Marchand and Duffy, 1988; Hartley et al., 1987; and Duffy 1984).

2.2 Experimental Methods

The measurement of the temperature field at a dynamic crack tip (a crack tip that is either propagating or dynamically loaded) requires some specific properties from the measurement apparatus. First, it is necessary that the measurement technique does not significantly alter the deformation field or the temperature field. Thus, it must be a non-

destructive technique; drilling a hole for a thermocouple, for example, is not feasible. Second, it is necessary that the system be capable of fast response times. For a crack propagating at 900 m/s the temperature could rise from zero to its maximum in 2 μs. A rise time of at least 1 μs in the measuring system is required. Candidate methods include; thermocouples on the surface, thermally sensitive films and infrared detector.

Thermocouples have been used by Fuller et al. (1975), Shockey et al. (1983), Klemm (1989) and Döll (1973) to make some measurements involving the temperature fields around dynamically propagating cracks. In studying PMMA, Doll attached thermocouples within one millimeter of the crack path, and, as the crack passed, a temperature was recorded. Shockey et al. also used thermocouples welded to the side of the prospective crack path. Fuller et al. combined thermocouples with temperature sensitive liquid crystal films and infrared temperature measurements, using InSb detectors, of the crack faces. Eq (2.1) was used along with extensive assumptions about the plastic zone to find the maximum temperature, T_{max}=230°C. Klemm used the thermocouples in the crack path to actually measure the temperature field in the 50 mm plastic zone for a ductile steel. A maximum temperature of 100°C is reported.

Coffey and Jacobs (1981) and Swallowe et al. (1986) used thermally sensitive films to measure the temperature of various polymers under impact loading and subsequent failure. Temperatures up to 700°C are reported.

Moss and Pond (1975) used infrared detectors to investigate the formation of inhomogeneities in the deformation of copper. Although other authors had used unfocused IR detectors to measure average temperature (Fuller et al., 1975), Moss and Pond were interested in the formation of Luders bands in copper and, thus, they were interested in measuring the local thermal changes in the material. They used a single GeCu infrared detector in conjunction with a Cassegrain mirror system to measure temperature at two close points on the sample relative to each other. They report a temperature rise of

18°C in the Luders band compared to the bulk. Duffy and coworkers (Marchand and Duffy, 1988; Hartley et al., 1987; and Duffy 1984) used a linear array of InSb detectors focused with a single convex mirror, later replaced by a Cassegrain microscope objective, to measure the temperature in dynamically shearing cylinders loaded in torsion. Maximum temperatures of 450°C are reported. The use of mirror elements in the optical systems by these authors is motivated by the desire to limit aberration. Because the detectors integrate energy over a wide range of wavelengths, it is necessary that the optical system focuses over that same range of wavelengths. Any refracting element would certainly produce unacceptable levels of chromatic aberration that would render the system inaccurate. The switch by Duffy and coworkers (Marchand and Duffy, 1988; Hartley et al., 1987; and Duffy 1984) and Fuller et al. (1975) to InSb detectors from the GeCu detector of Moss and Pond (1975) reflects the desire to produce the greatest sensitivity in the range of wavelengths expected in addition to maintaining the smallest rise time possible. InSb offers the best balance of these two objectives.

The difficulty with thermocouples is that they produce very small signals even when placed within 1mm of the crack path. Locating them directly in the crack path would still not suffice unless very large plastic zones were expected as in the case of Klemm (1989). Also, because of the finite size of the actual thermocouple junction, slow rise times, $> 1\mu s$, are characteristic. Thermally sensitive films suffer from calibration difficulties. The duration and temperature of exposure *both* contribute to the darkening of the film. It is necessary to assign a temperature value to various grey levels in a calibration before any quantitative results may be recorded, and there is always some ambiguity due to the effects of the length of exposure. Furthermore, both thermocouples and thermally sensitive films do not offer high spatial resolution. It is expected from Fig 2.1 that the temperature will be localized to a small area, thus thermocouple measurements are taken some distance away from the maximum temperature

and extrapolation is used. Thermally sensitive films blacken in the area of maximum temperature making the indiscernible grey-level patterns. Finally, thermocouples and thermally sensitive films offer only surface temperature measurements. No indication of the temperature within the solid is recorded. Infrared detectors offer an easy, but expensive, solution to the problems of measuring the temperature field at a crack tip with thermocouples or thermally sensitive films. Infrared detectors have fast response times, are non-destructive and are relatively easy to calibrate and utilize. One drawback to using infrared detectors, however, is that they too offer only surface temperature measurement.

The results reported here use the system employed by Zehnder and Rosakis (1991 and 1992) and Zehnder and Kallivayalil (1991). An Offner imaging system is used, instead of a Cassegrain system, in conjunction with a linear array of InSb detectors. Originally developed for use in micro-lithography,(Offner, 1975) the Offner optical system offers the ability to correct the image for third- and fifth-order abberations. Although such accuracy may not be required due to the finite detector size, the system is quite simple to set up, and it offers some desirable features. First, the system can be easily and inexpensively assembled from commercially available optical components. Suzuki (1983a and 1983b) has evaluated the proper separation distance of the two reflecting components that minimizes the abberations. Second, by choosing large components the system can be set up with a large aperture making the detection of small changes in temperature quite easy. Also, for the temperature measurement around dynamically propagating crack tips it is desirable to have the measuring equipment a safe distance from the fracture event. The Offner system can accommodate this requirement without difficulty. One drawback to the Offner system is that it has fixed magnification, 1:1, that cannot be changed without destroying the performance of the optical system. Also, the image is not formed on the system axis, and the use

of planar mirrors is required to make the image easily accessible. In contrast to the Offner system, the Cassegrain system *can* be used to produce variable magnification, and the detector array may be placed in line with the system so that no additional planar mirrors are required to view the image. However, drawbacks to the Cassegrain system include; obstructed aperture, small field of view and less aberration correction than the Offner system. Furthermore, the system is expensive if it is purchased commercially. There are several additional promising optical systems in the literature that provide a balance of the desirable features of both the Offner and the Cassegrain system(Rah and Lee, 1989, and Egdall, 1985). These systems use reflecting elements exclusively to eliminate chromatic aberration and have been corrected to produce almost diffraction limited performance. Unfortunately, they are not commercially available and require considerable sophistication to manufacture and assemble.

As noted before, the detectors integrate over a range of wavelengths. For InSb that range is 1 μm to 5.5 μm. The voltage produced by the detectors is related to the energy emitted by the specimen through an integral depending upon the emissivity of the material, $\epsilon(\lambda, T)$, the spectral response of the InSb detector, $R(\lambda)$, and the black body radiation function, $P(\lambda)$, where λ is the wavelength of the radiation.

$$v(T, T_o) = A A_D \beta \int_{1\mu m}^{5.5\mu m} R(\lambda)[P(\lambda. T)\epsilon(\lambda. T) - P(\lambda, T_o)\epsilon(\lambda, T_o)]d\lambda \qquad (2.6)$$

where A is the amplification, A_D is the detector area and β is the fraction of energy transmitted to the detectors by the optical system (related to the aperture). This relation when evaluated for InSb detectors produces a nearly linear relation on a log-log plot(Zehnder and Rosakis, 1991 and 1992). By simply heating a specimen, measuring its surface temperature with a thermocouple, and plotting the results on a log-log plot, one may establish a calibration curve for the detectors that eliminates the need to evaluate the emissivity of the sample, the spectral response of the detector and the black body radiation function. Using this calibration, the voltage record of a detector during

a test may be trivially converted into a temperature measurement.

In order to protect the infrared detector imaging system from the dangers of impact loading, dynamic cracks are produced by statically wedge loading a compact tension specimen with a blunt notch. The speed of the crack can be roughly controlled by changing the radius at the notch tip; a blunt notch produces a faster crack than a sharp notch. Dynamic cracks are produced by the storage of elastic energy at the notch tip prior to failure; as the load is increased more elastic energy is stored in the specimen. When a small crack initiates at the notch tip, the excess elastic energy drives the crack dynamically through the specimen. The notch radius is machined by conventional EDM techniques giving a reproducible notch root radius. A minimum radius of .25 mm is attainable resulting in a minimum crack speed of 600 m/s. Crack speed is measured by a series of conducting break-lines on the back surface of the sample (see Zehnder and Rosakis, 1991 and 1992, and Zehnder and Kallivayalil, 1991). Alternatively, dynamic cracks may also be produced in three-point bend impact (Kalthoff, 1985), or mode-II impact loading (Kalthoff, 1987, Lee and Freund, 1990 and Mason et al., 1992).

2.3 Results and Discussion

The results of four testing conditions are reviewed here. In Fig 2.2a the results of Zehnder and Rosakis (1991) are recalled, and in Fig 2.2b the results of a recent investigation by the authors are shown. The material in both experiments is the same, oil-quenched 4340 steel with hardness R_c =44 (see Tables 2.1-2.3), but the crack speed is 900 m/s in the Zehnder and Rosakis (1991) experiment while the crack speed is 600 m/s here. These results are representative of a number of experiments. In the latter case four separate experiments were performed, some with different apertures, to show the repeatability of the results. Temperature rises below 50°C fall below the noise level of the system. It can be seen that the two fields are significantly different. Most noticeable is the triangular arrangement of the temperature contours behind the crack

Table I: Tensile Properties				
Material and Condition	σ_y MPa	σ_u MPa	ϵ_u %	K_{Ic} MPa$\sqrt{m}$
4340, quenched[50]		1700		44
Ti, 0%—α[17]	1370	1390	0.35	56

Table II: Elastic Properties			
Material and Condition	E GPa	ν	ρ kg/m^3
4340, quenched[1]	210	.30	7830
Ti, 0%—α[3,32]	110	.32	4650

Table III: Thermal Properties				
Material and Condition	c_p J/kg°C	k W/m°C	α μm^2/s	κ μm/m°C
4340, quenched[1]	448	34.6	9.86	11.2
Ti, 0%—α[3,32]	490	10.9	4.78	9.7

(Values are taken from the indicated reference number.)

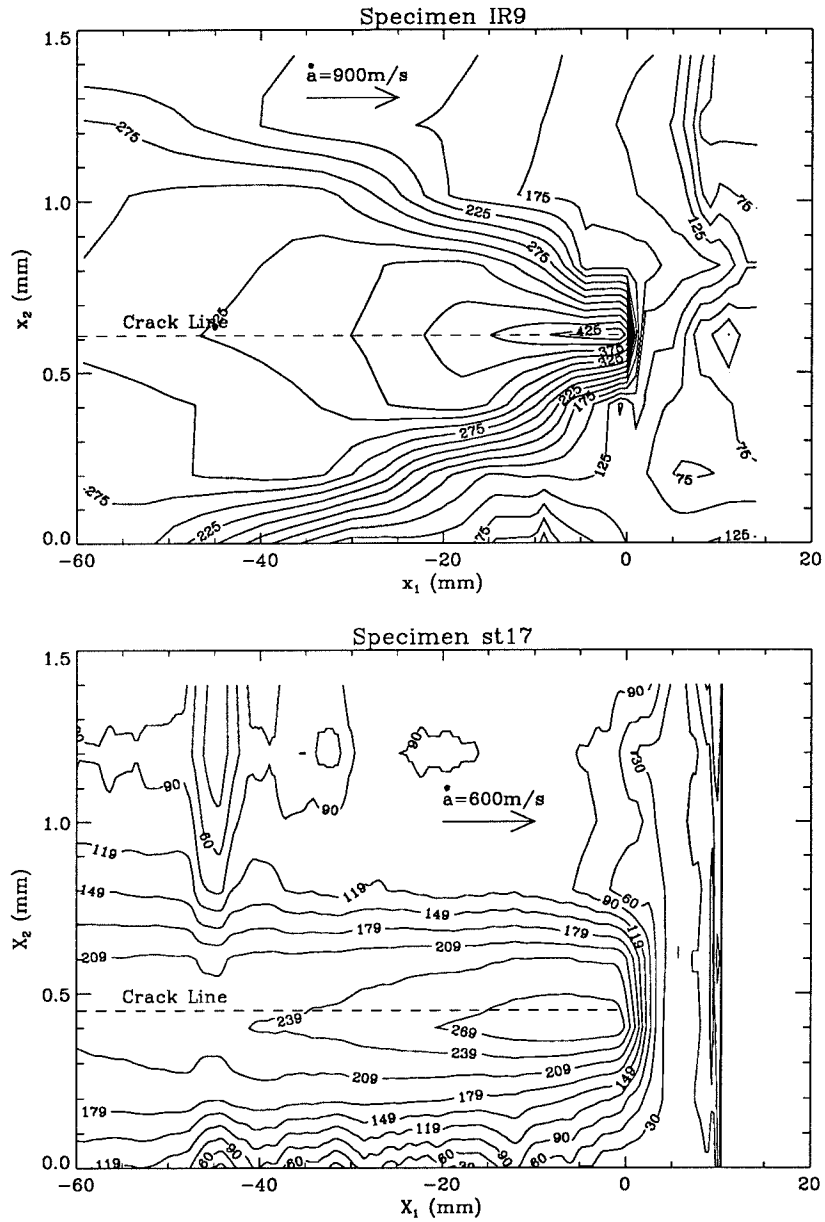

FIGURE 2.2 Temperature distribution measured experimentally using infrared detectors around a crack tip propagating in 4340 oil quenched steel at a velocity of 900 m/s (Zehnder and Rosakis, 1991) and 600 m/s. Maximum temperatures of approximately 450°C at 900 m/s and 300°C at 600 m/s are observed. The crack line location in the vertical direction is estimated from the symmetry of the results. The temperature rise at $x_2 \approx 1.2$ mm in the slower velocity experiment is due to the formation of another shear lip. Note that this formation occurs behind the crack tip at distances at least as large as 20 mm.

when $\dot{a}$ =900 m/s. Contours emanating from the crack tip expand outward initially before curving back to meet the negative x_1 axis. Similar contours are not seen for $\dot{a}$ =600 m/s or in Fig 2.1. At 600 m/s an interesting feature of the temperature field is seen along the horizontal line, x_2 =1.2. Here the temperature rise due to the formation of another "shear lip" is observed. This formation occurs behind the crack tip and is much less intense in terms of plastic work rate density. Examination of the specimen after failure reveals that the "other shear lip" follows a path parallel to the crack path. The maximum temperature for 900 m/s is 450°C while the maximum temperature for 600 m/s is 300°C. The crack tip positions are estimated from the crack tip displacement record. This method is not very accurate and the crack tip location uncertainty may be as much as .5 mm.

In Fig 2.3 the results of some experiments on two separate titanium alloys are shown. In the first case a Ti-10V-2Fe-3Al alloy was tested in the 0%-α state (Giovanola, 1989, see Tables 2.1-2.3). The crack speed is 380 m/s and the maximum temperature is greater than 400°C (the detectors saturated). In the second case the results of Zehnder and Kallivayalil (1991) for Beta-C titanium are shown. The crack speed is 400 m/s, and the maximum temperature is 260°C. The results for Ti-10V-2Fe-3Al bear resemblance to the results for 4340 at 600 m/s as well as the theoretical result shown in Fig 2.1. Contours extend directly back from the plastic zone roughly parallel to the crack faces eventually curving in to meet at the negative x_1 axis. In contrast, the contours in the experiment on Beta-C titanium emanate outwardly as for 4340 steel at 900 m/s. Further, the existence of a shear localization above the crack tip due to the stress state at the surface of the specimen (Zehnder and Rosakis, 1991) is seen. This "other shear lip" is seen to curve out of the field of view behind the crack tip unlike the "other shear lip" observed in the experiments on 4340 steel at 600 m/s. The shear lips formed in the testing of Beta-C titanium are much smaller than those formed in the testing

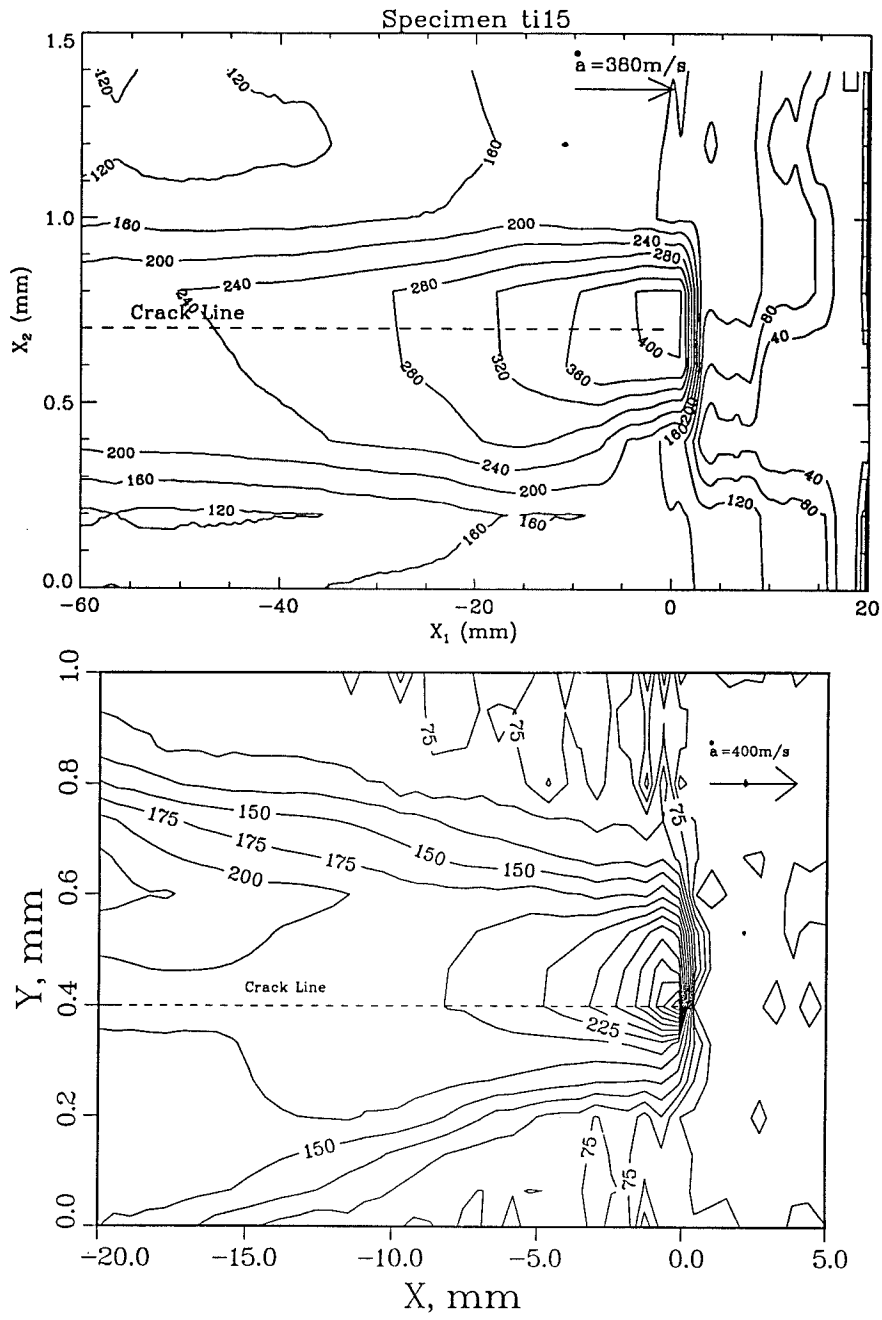

FIGURE 2.3 The temperature field around a crack tip propagating at 380 m/s in Ti-10V-2Fe-3Al alloy and 400 m/s in Beta-C Ti (Zehnder and Kallivayalil, 1991). Some of the detectors were saturated in the Ti 10V-2Fe-3Al test, but a maximum temperature of approximately 500°C may be extrapolated from the results. In the Beta-C Ti material a maximum temperature of 260°C is reported.

of Ti-10V-2Fe-3Al. In the Beta-C it can be seen in the figure that the shear lips are approximately .5 mm wide while in Ti-10V-2Fe-3Al examination after testing reveals that the shear lips can be as much as 4 mm wide.

Fractographic analysis of the shear lips offers some interesting comparisons. In Fig 2.4 the fracture surface of the steel specimen at $\dot{a}$ =600 m/s may be seen both in the flat fracture regime and in the shear lip. It can be seen that there is a drastic difference in the two surfaces. In the flat fracture regime, the surface is rough and the crack path is tortuous. Regions of microvoid coalescence may be observed. On the shear lip, smooth surfaces dominate. This fracture is similar to the fracture surface reported by Giovanola (1988a and 1988b) for a shear band in the same material with a different heat treatment. Giovanola reports the existence of "cobbled regions" as well as microvoid coalescence regions that are not seen here, but it is clear that the two fracture modes are the same. In the titanium, Fig 2.5, the flat fracture regime exhibits a tortuous crack path with regions of microvoid coalescence visible along the walls of the peaks and valleys, but in the shear lip fracture is dominated by microvoid coalescence. The voids on the shear lip are much larger than those in the bulk fracture region. None-the-less, it is clear that microvoid coalescence in shear is important in both regions. Thus, the two regions are similar.

2.3.1 Temperature Fields in Steel

The most striking difference between Figs 2.2a and 2.2b is the existence of triangular contours emanating from the crack tip in the temperature field at the higher velocity. Because the velocity of the crack is extremely high when compared to the material properties (the size of the plastic zone and $k/\rho c_p$) in both figures it is expected that *both* fields should reflect the qualitative behavior exhibited in Fig 2.1 (Mason and Rosakis, 1992). The contour lines should extend directly back from the plastic zone parallel to the crack faces until they eventually curve toward the negative x_1 axis some

(a)

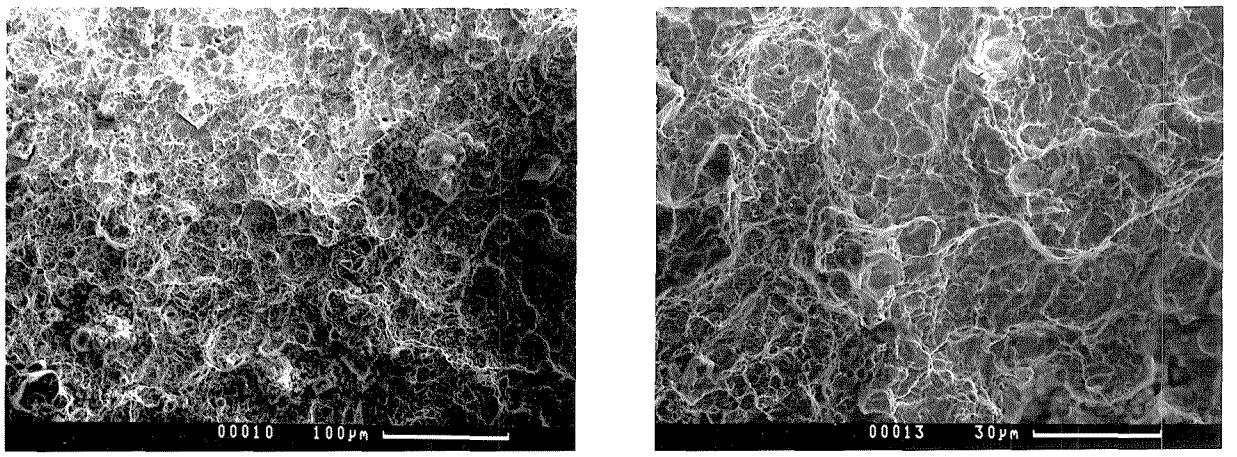

(b)

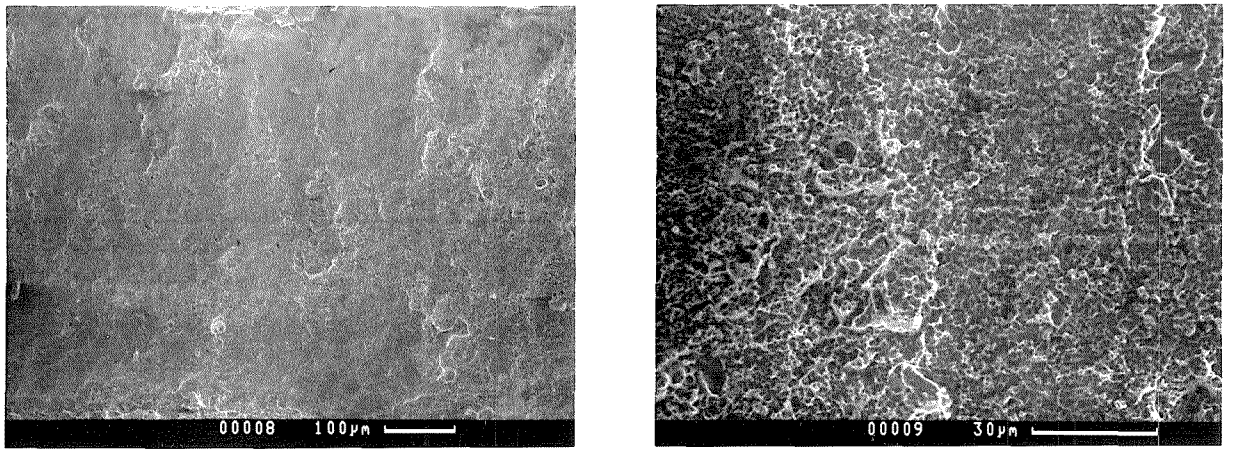

FIGURE 2.4 Examination of the fracture surfaces in steel reveals different fracture morphology (a) in the flat fracture region than (b) on the shear lips. The smoother fracture surface in the shear lips indicates the formation of a shear band as seen in Giovanola (1988a and 1988b).

(a)

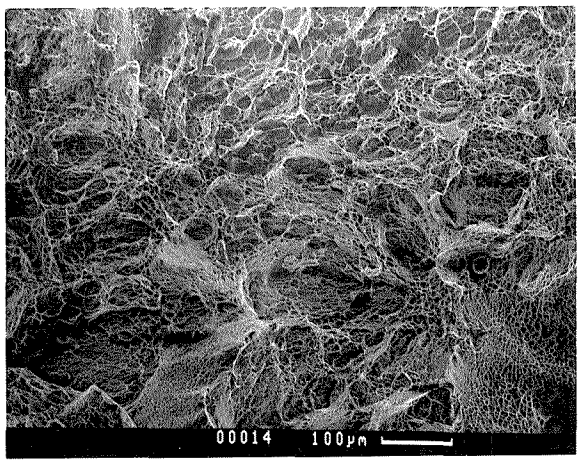

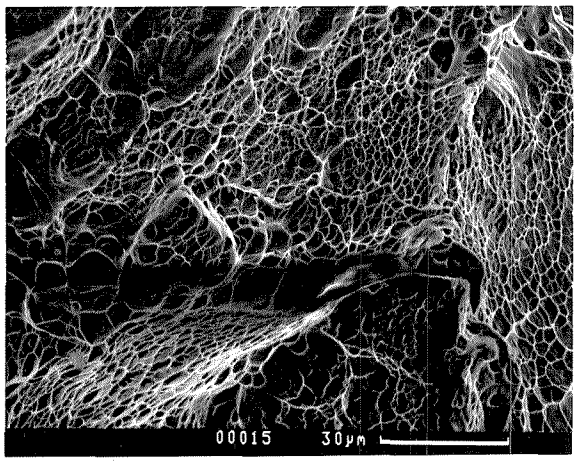

(b)

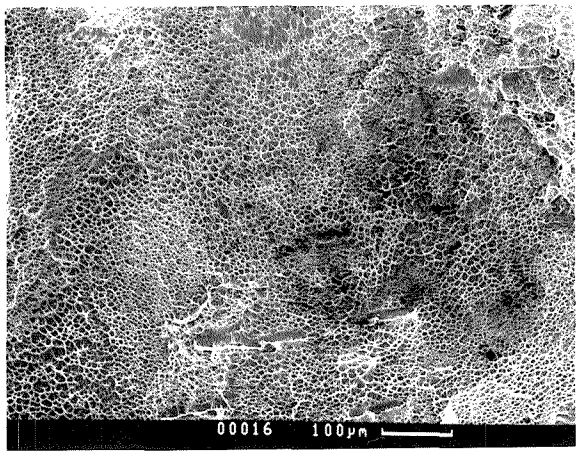

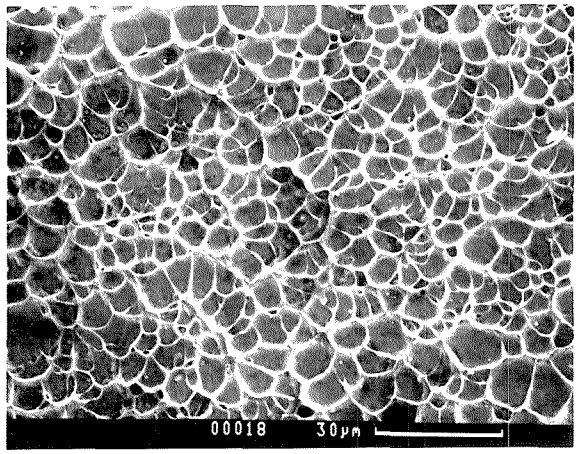

FIGURE 2.5 The fracture surfaces in Ti-10V-2Fe-3Al reveal very similar fracture in (a) the flat fracture region and (b) the shear lip. However, more evidence of ductile void growth is evident in the shear lip and a more tortuous path is seen in the flat fracture regime.

distance behind the crack tip. This behavior *is* seen in Fig 2.2b, but it is *not* seen in Fig 2.2a.

Owing to the heavy dependence of theoretical maximum temperatures upon the assumptions about the plastic zone, it was initially thought that the difference in contours between Figs 2.2a and 2.2b might be due to a difference in plastic zone. Unfortunately, estimates of the plastic zone show no difference between the plastic deformation at high and low velocities that could explain the change in the contours. Further, attempts to explain the difference in temperature field at high and low velocities using hyperbolic heat conduction have shown that this theory is not effective in modelling the observed behavior (Mason and Rosakis, 1992). It seems that the change in temperature field at the higher velocities is due to movement of the crack faces. It has been shown by Freund (1977) that, qualitatively, the crack opening velocity should be proportional to the crack velocity and the initial crack tip stress intensity factor. Clearly the crack tip velocity is higher in one case, but, also, the initial stress intensity factor may be as much as three times higher when $\dot{a} = 900$ m/s than when $\dot{a} = 600$ m/s (Rosakis and Zehnder, 1985). Combined, these two effects predict that the crack opening velocity in the 900 m/s test may be 5 times higher than that in the 600 m/s test. From the angle of the contours it is estimated that the average velocity of the crack faces in the x_2 direction is 7.5 m/s when the crack tip velocity is 900 m/s and less than 2 m/s when the crack tip velocity is 600 m/s resulting in a ratio of crack face velocities greater than 4. Inaccuracies are expected when comparing this simple theory with the experimental results. The specimen is much more complex in the experiment than in the theory and measurements of the initiation stress intensity factor were not made. Consequently, it is concluded here that crack opening is responsible for the change in temperature field at the higher velocity, however, no quantitative analysis of this effect is implied.

The plastic work rate ahead of the crack tip may be estimated by using Eq (2.3)

and neglecting conduction (Zehnder and Rosakis, 1991 and 1992, and Zehnder and Kallivayalil, 1991). Letting $\alpha = 0$ in this equation yields

$$-\rho c_p \dot{a} \frac{\partial T}{\partial x_1} = \beta \sigma_{ij} \dot{\epsilon}^p_{ij}. \tag{2.7}$$

Solving this relation for the experimental results in Fig 2.2 gives the results shown in Fig 2.6. For steel β is taken to be .9; this choice is justified by some preliminary results of a split Hopkinson pressure bar investigation of this material parameter (Mason et al., 1992). It is seen that the plastic zone is approximately twice as large in the lower velocity experiment as it is in the higher velocity experiment. The fact that they are almost exactly twice as large in the x_2 direction is due to discretization of the temperature field by the finite detectors. It can only be said that at the lower velocity there is a larger plastic zone then at the higher velocity. The maximum plastic work density rate in the high-speed test is 600×10^{12} J/m^{3}s while in the low-speed test the maximum is 200×10^{12} J/m^{3}s, a third as much. The change in maximum plastic work rate density and the change in the x_2 dimension of the plastic work zone in conjunction with the fractography seen in Fig 2.4 indicate that the shear lip is actually a shear band. A localization of the deformation is observed as crack velocity increases indicating the formation of an adiabatic shear band.

Estimation of the energy fraction consumed by the formation of the shear lips (Zehnder and Rosakis, 1991) shows that roughly the same fraction of energy is expended in the shear lips in both the high- and low-speed experiments. Values for the energy expended in the lips during low-speed fracture were, in general, slightly higher than the high-speed experimental results, but, within the large uncertainty of the calculation, the two are equal. Regardless, a surprisingly large percentage, 50%, of the energy of dynamic fracture is expended in the shear lips during fast fracture. This is surprising because the area of the shear lips accounts for only about 10% of the fracture surface area in both experiments.

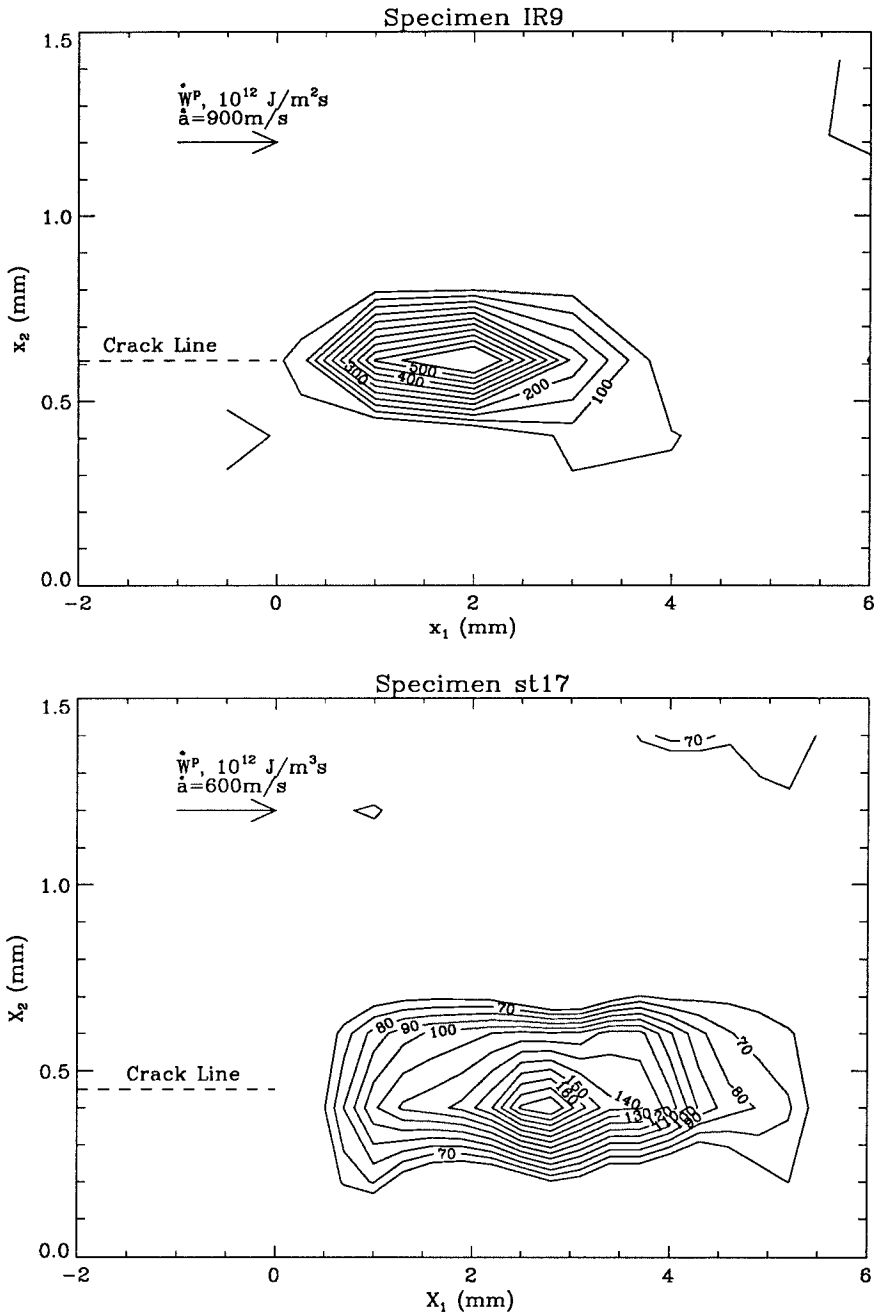

FIGURE 2.6 The plastic work zone as estimated from Eq (7) is shown for a crack propagating in oil-quenched 4340 steel at two velocities; 900 m/s and 600 m/s. It is seen that the plastic zone is elongated in the x_1 direction and that although the shape is the same at both velocities the zone at higher velocities is smaller reflecting a localization of plastic deformation as velocity increases.

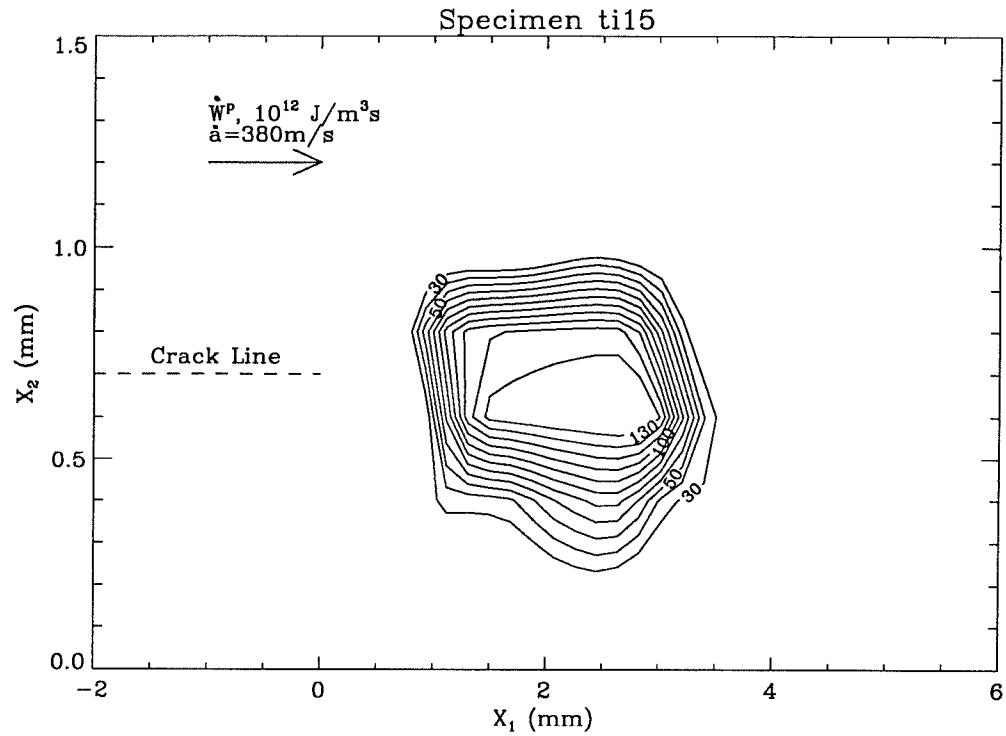

FIGURE 2.7 The plastic zone for Ti-10V-2Fe-3Al is estimated as in Eq (2.7). The zone shows similarity in shape to the results for 4340 steel in Fig 2.6. The magnitude of the plastic work is the same as for oil quenched 4340 steel with a crack propagating at 600 m/s, but the temperature is higher because the factor $\rho c_p \dot{a}$ is smaller in the Ti-10V-2Fe-3Al.

2.3.2 Temperature Fields in Titanium

In titanium the plastic zone is quite similar in size and shape to the plastic zones in steel; see Fig 2.7. The maximum plastic work rate density at 380 m/s is estimated—since the detectors saturated—to be approximately equal to the maximum plastic work rate density in 4340 steel at 600 m/s while the maximum temperature is greater than 400°C in Ti compared to 300°C in steel. Since adiabatic conditions apply at the crack tip (this is readily shown by comparing the magnitude of two terms on the left-hand side of Eq (2.3)), it is expected that Eq (2.7), which has no dependence upon thermal conductivity, k, should apply. Thus, the temperatures are *higher* in Ti than in steel when plastic work rates are roughly equal, however they are not higher because of the lower thermal conductivity. The temperature is actually higher because the factor

$\rho c_p \dot{a}$ is smaller in the titanium; in titanium $\rho c_p \dot{a} = 8.7 \times 10^8$ J/m^{2}s°C while in steel $\rho c_p \dot{a} = 21.0 \times 10^8$ J/m^{2}s°C, roughly twice that in titanium.

Bryant et al. (1986) indicate evidence of localized melting in the Ti-10V-2Fe-3Al alloy used here, but fractographic examination in Fig 2.5 gives no indication of melting in the shear lips or the flat fracture region. This may be due to differences in heat treatment.

In the experiments by Zehnder and Kallivayalil (1991) on Beta-C titanium the existence of a shear lip above the actual crack demonstrates that crack face opening has an effect on the measurement of temperature field. The shear lip is seen to curve out of the field of view. Since it is certain that near adiabatic conditions apply and that shear lip formation occurs parallel to the crack path, it is concluded that this movement is due to a translation of the crack faces rather than a change in the deformation. Thus, crack face opening effects are seen in Beta-C titanium at 400 m/s supporting the conclusion that crack face opening is seen in the steel tests at 900 m/s.

2.4 Conclusions

1. It is clear that the shear lip formed in oil-quenched 4340 steel is actually a shear band, a localization of the shear deformation to a narrow plane as a result of thermal softening in the material. At lower velocities the localization is less pronounced and the maximum temperature measured is lower. Fractography indicates a shear band fracture mode in the shear lip but not in the flat fracture regime.

2. The temperature field around a dynamically propagating crack tip in oil-quenched 4340 steel changes significantly when the crack velocity is increased from 600 m/s to 900 m/s. This effect is attributed to the faster crack opening rate at higher velocities. Conclusive evidence of crack face opening is seen

in the temperature fields of Zehnder and Kallivayalil for Beta-C titanium (Zehnder and Kallivayalil, 1991), and it is predicted by a simply theory that crack face opening will be much more significant at 900 m/s than at 600 m/s in 4340 steel.

3. In titanium the generation of heat at the tip of a dynamically propagating crack has been investigated. The maximum temperature in Ti-10V-2Fe-3Al for equivalent maximum plastic work rate densities is higher than in 4340 steel. Because of the adiabatic conditions at the crack tip this effect is not attributed to the lower thermal conductivity, rather it is attributed to lower crack speeds, the lower density and the lower heat capacity of titanium through the factor $\rho c_p \dot{a}$.

4. In Ti-10V-2Fe-3Al in the shear lips, failure is dominated by nucleation and growth of large micro-voids while in the bulk, flat-fracture region, failure occurs by the nucleation and growth of smaller micro-voids and a more tortuous crack path. Large micro-voids generate more plasticity than small voids, so it is expected that temperatures will be higher when microvoid growth is more extensive, in the shear lip.

References

1. *Aerospace Structural Metals Handbookm (1989),* Metals and Ceramics Information Center, Battelle Columbus Laboratories, Columbus, Ohio, Vol. 1, code 1206

2. M.B. Bever, D.L. Holt and A.L. Titchener (1973), The stored energy of cold work, *Prog. Mat. Sci.,* **17,** 1

3. J.D. Bryant, D.D. Makel and H.G.F. Wilsdorf (1986), Observations on the effect of temperature rise at fracture in two titanium alloys, *Mat. Sci. Engr.,* **77,** 85,

4. H.S. Carslaw and J.C. Jaeger (1959), *Conduction of Heat in Solids,* Oxford Press, London

5. R.J. Clifton and R.W. Klopp (1985), Pressure-shear plate impact testing, *Metals Handbook; 9th Edition,* American Society for Metals, Metals Park, OH, Vol. 8, 230

6. C.S. Coffey and S.J. Jacobs (1981), Detection of local heating in impact or shock experiments with thermally sensitive films, *J. Appl. Phys.,* **52,** 6991

7. W. Döll (1973), An experimental study of the heat generated in the plastic region of a running crack in different polymeric materials, *Engr. Frac. Mech.,* **5,** 259

8. A.S. Douglas and H.U. Mair (1987), The temperature-field surrounding a dynamically propagating mode-III crack, *Scripta Met.,* Vol. 21, p. 479, 1987

9. J. Duffy (1984), Temperature measurements during the formation of shear bands in a structural steel, G.J. Dvorak and R.T. Shield, eds., *Mechanics of Material Behavior,* Elsevier Science Pub. B.V., Amsterdam, 75

10. I.M. Egdall (1985), Manufacture of a three mirror wide-field optical system, *Optical Engr.,* **24,** 285

11. P.S. Follansbee (1985), The split Hopkinson bar, *Metals Handbook; 9th Edition,* American Society for Metals, Metals Park, OH, **8,** 198

12. P.G. Fox and J. Sonria-Ruiz (1970), Fracture-induced thermal decomposition in brittle crystalline solids, *Proc. R. Soc. London A,* **317,** 79

13. L.B. Freund (1977), A simple model of the double cantilever beam crack propagation specimen, *J. Mech. Phys. Sol.,* **25,** 69

14. K.N.G. Fuller, P.G. Fox and J.E. Field (1975), Temperature rise at the tip of fast moving cracks in glassy polymers, *Proc. Roy. Soc. London A,* **341,** 537

15. J.H. Giovanola (1988a), Adiabatic shear banding under pure shear loading, Part I., *Mechanics of Materials,* **7,** 59

16. J.H. Giovanola (1988b), Adiabatic shear banding under pure shear loading, Part II., *Mechanics of Materials,* **7,** 73

17. J.H. Giovanola, R.W. Klopp and J.W. Simons (1989), Effect of shear lips on dynamic crack propagation, *Proc. OJI International Seminar on Dynamic Fracture,* Toyohashi, Japan, August, 1989

18. K.A. Hartley, J. Duffy and R.H. Hawley (1987), Measurement of the temperature profile during shear band formation in steels deforming at high strain-rates, *J. Mech. Phys. Sol.,* **35,** 283

19. J.W. Hutchinson (1984), Introduction to the viewpoint on shear bands, *Scripta Met.,* **18,** 421

20. J.F. Kalthoff (1985), On the measurement of dynamic fracture toughnesses—a review of recent work, *Int. J. Frac.,* 27, 277

21. J.F. Kalthoff (1987), Shadow optical analysis of dynamic shear fracture, *Photomechanics and Speckle Metrology,* SPIE Vol. 814, 531

22. W. Klemm (1989), *Presented at the Joint American Society of Mechanical Engineers, Japan Society of Mechanical Engineers International Pressure Vessel and Piping Conference*

23. R. Krishna Kumar, R. Narasimhan and O. Prabhakar (1991), Temperature rise in a viscoplastic material during dynamic crack growth, *Int. J. Fracture,* **48,** 23

24. Z.-B. Kuang and S. Alturi(1985), Temperature field due to a moving heat source: a moving mesh finite element analysis, *J. Appl. Mech,* **52,** 277

25. Y.J. Lee and L.B. Freund (1990), Fracture initiation due to asymmetric impact loading of an edge cracked plate, *J. Appl. Mech.,* **57,** 104

26. Z.L. Li, J.L. Yang and H. Lee (1988), Temperature fields near a running crack tip, *Eng. Frac. Mech.,* **30,** 791

27. P.N. Malali (1988), Thermal Fields Generated by Dynamic Mode III Fracture in Ductile Materials, M.S. Thesis, The Johns Hopkins University, Baltimore, 1988

28. A. Marchand and J. Duffy (1988), An experimental study of the formation process of adiabatic shear bands in a structural steel, *J. Mech. Phys. Sol.,* **36,** 251

29. J.J. Mason, J. Lambros and A.J. Rosakis (1991), On the use of a coherent gradient sensor in dynamic mixed-mode fracture mechanics experiments, to appear *J. Mech. Phys. Sol.*

30. J.J. Mason and A.J. Rosakis (1992), The effect of hyperbolic heat conduction around a dynamically propagating crack tip, SM Report 92-3, Graduate Aeronautical Laboratories, California Inst. of Tech.

31. J.J. Mason, A.J. Rosakis and G. Ravichandran, The conversion of plastic work to heat around a dynamically propagating crack in metals, SM Report 92-17, Graduate Aeronautical Laboratories, California Inst. Tech., Pasadena, CA 91125, 1992

32. *Metals Handbook, 9th Edition* (1980), American Society for Metals, Metals Park, OH, Vol. 3, 397

33. G.L. Moss and R.B. Pond (1975), Inhomogeneous thermal changes in copper during plastic elongation, *Met. Trans. A,* **6A,** 1223

34. A. Offner (1975), New concepts in projection mask aligners, *Optical Engr.,* **14,** 130

35. S.Y. Rah and S.S. Lee (1989), Four-spherical-mirror zoom telescope continuously satisfying the aplanatic condition, *Optical Engr.,* **28,** 1014

36. J.R. Rice and N. Levy (1969), Local heating by plastic deformation at a crack tip, in A.S. Argon, ed., *Physics of Strength and Plasticity,* M.I.T. Press, Cambridge, MA, 277

37. A.J. Rosakis and A.T. Zehnder (1985), Dynamic fracture initiation and propagation in 4340 steel under impact loading, *Int. J. Frac.,* Vol. 27, p. 169, 1985

38. D.A. Schokey, J.F. Kalthoff, W. Klemm and S. Winkler (1983), Simultaneous measurements of stress intensity and toughness for fast cracks in steel, *Exp. Mech.,* **40,** 140

39. I.N. Sneddon and D.S. Berry (1958), The classical theory of elasticity, in S. Flugge, ed., *Handbuch der Physik,* Vol VI, Springer-Verlag, Berlin, 123

40. J.C. Sung and J.D. Achenbach (1987), Temperature at a propagating crack tip in a viscoplastic material, *J. Thermal Stresses,* **10,** 243

41. A. Suzuki (1983a), Complete analysis of a two-mirror unit magnification system, Part I., *Appl. Optics,* **22,** 3943

42. A. Suzuki (1983b), Complete analysis of a two mirror unit magnification system, Part II., *Appl. Optics,* **22,** 3950

43. G.M. Swallowe, J.E. Field and L.A. Horn (1986), Measurements of transient high temperatures during the deformation of polymers, *J. Mat. Sci.,* **26,** 4089

44. G.I. Taylor and M.A. Quinney (1934), The latent energy remaining in a metal after cold working, *Proc. Roy. Soc London A,* **143,** 307

45. D.Y. Tzou (1990a), Thermal shock waves induced by a moving crack, *J. Heat Transfer,* **112,** 21

46. D.Y. Tzou (1990b), Thermal shock waves induced by a moving crack—a heat flux formulation, *Int. J. Heat Transfer,* **33,** 877

47. R. Weichert and K. Schönert (1974), On the temperature rise at the tip of a fast running crack, *J. Mech. Phys. Sol.*, **22,** 127

48. R. Weichert and K. Schönert (1978a), Temperature distribution produced by a moving heat source, *Q. J. Mech. Appl. Math.*, **31,** 636

49. R. Weichert and K. Schönert (1978b), Heat generated a the tip of a moving crack, *J. Mech. Phys. Sol.*, **26,** 151

50. A.T Zehnder and A.J. Rosakis (1991) On the temperature distribution at the vicinity of dynamically propagating cracks in 4340 steel, *J. Mech. Phys. Sol.*, **39,** 385

51. A.T. Zehnder and A.J. Rosakis (1992), Temperature rise at the tip of dynamically propagating cracks: measurements using high-speed infrared detectors, to appear *Experimental Mechanics in Fracture,* **III**

52. A.T. Zehnder and J.A. Kallivayalil (1991), Temperature rise due to dynamic crack growth in Beta-C titanium, *Speckle Techniques, Birefringence Methods, and Applications to Solid Mechanics,* SPIE Vol. 1554A, 48

CHAPTER 3

The Effects of Hyperbolic Heat Conduction Around a Dynamically Propagating Crack Tip

Overview

Using infrared detectors, Zehnder and Rosakis (1991), Zehnder and Kallivayalil (1991) and Mason and Rosakis (1992), have recorded the temperature field around a dynamically propagating crack tip travelling at constant velocity in several metals. At the same time, Tzou (1990a, 1990b) has suggested that the temperature field around a propagating crack tip might exhibit some of the characteristics of hyperbolic heat conduction. In this paper a corrected solution of the hyperbolic heat conduction equation for a traveling point source is derived. Then an experimental estimate of the active plastic zone (heat generating zone) at a crack tip is used for various experimental conditions to examine the possible effects of hyperbolic heat conduction around a propagating crack tip. Finally, using the actual experimental conditions of Zehnder and Rosakis (1991), Zehnder and Kallivayalil (1991) and Mason and Rosakis (1992) it is shown that no effects of hyperbolic heat conduction are observed around a propagating crack tip. It is seen that, due to adiabatic conditions at the crack tip during these experiments, the solution of the hyperbolic heat equation is indistinguishable from the solution of the parabolic heat conduction equation for crack propagation in steel.

List of Symbols

$\mathbf{q}$	heat flux vector
k	thermal conductivity
T	temperature rise
S	heat source function
ρ	density
c_p	heat capacity
α	$k/\rho c_P$
v	thermal wave speed
$\dot{a}$	crack tip velocity
$\mathbf{z}$	stationary coordinates system
ξ	coordinates translating with the crack tip
M	thermal mach number, $\dot{a}/v$
κ	$\dot{a}/2\alpha\sqrt{\lvert 1-M^2\rvert}$
f	aspect ratio of the heat source zone
δ	size of heat source zone
Q	magnitude of heat source zone
$\mathbf{x}$	normalized coordinates translating with the crack tip
ψ	$\dot{a}\delta/2\alpha$
θ	$\rho c_p T/Q\delta$

3.1 Introduction

It is understood that the classical, or parabolic, heat conduction equation has an inherent pathology. That is, when a point source is introduced into a conducting medium, the parabolic heat conduction equation predicts that its presence is instantaneously felt throughout the medium. Often this pathology is referred to as "the infinite speed of heat propagation," and it has been addressed by Morse and Feshbach (1953) through the introduction of a new heat flux law. Usually, heat flux, $\mathbf{q}$, is related to the gradient of temperature by Fourier's Law,

$$\mathbf{q} = -k\nabla T.$$

When this relation is combined with the expression for the continuity of energy,

$$-\nabla \cdot \mathbf{q} + S = \rho c_p \dot{T},$$

where the dot refers to time differentiation, the parabolic heat conduction equation results,

$$\alpha \nabla^2 T - \dot{T} = -\frac{1}{\rho c_p} S. \tag{3.1}$$

(In this paper temperature, T, is implicitly taken as the change in temperature above ambient, $T = T_{\text{actual}} - T_{\text{ambient}}$.) If, instead of Fourier's Law, a new heat flux law is used,

$$\frac{\alpha}{v^2}\dot{\mathbf{q}} + \mathbf{q} = -k\nabla T,$$

then through similar manipulations the "hyperbolic" heat conduction equation results,

$$\alpha \nabla^2 T - \frac{\alpha}{v^2}\ddot{T} - \dot{T} = -\frac{1}{\rho c_p}\left(S + \frac{\alpha}{v^2}\dot{S}\right). \tag{3.2}$$

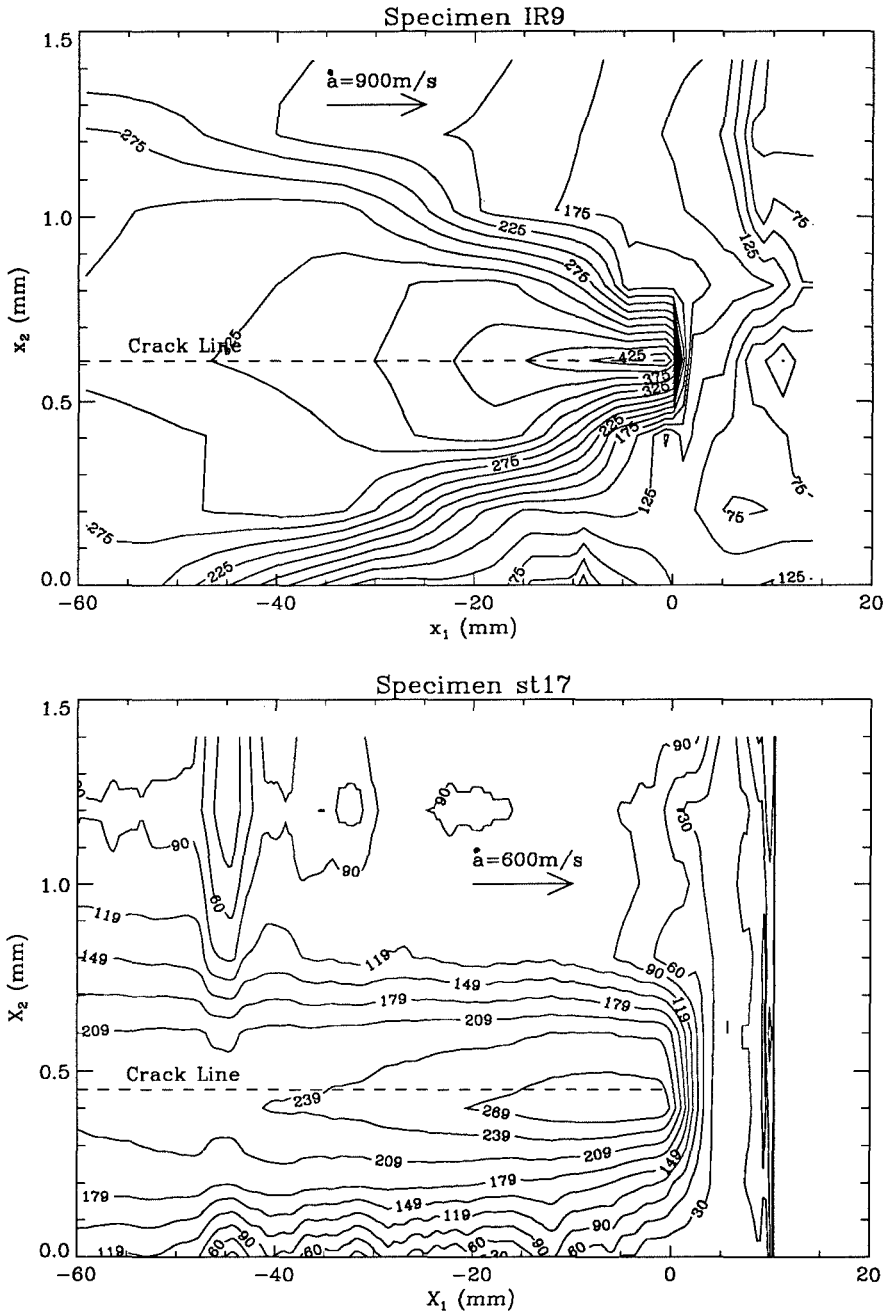

FIGURE 3.1 Temperature fields around a crack propagating in oil-quenched 4340 steel at two different velocities. The maximum temperature at higher velocities is 450°C (Zehnder and Rosakis, 1991) while the maximum temperature at 600 m/s is 300°C(Mason and Rosakis, 1991).

The introduction of the new heat conduction law has been justified by several authors, (for a review see Tzou (1990a,1990b)) and some experimental work has shown that this different heat conduction equation is more appropriate at large distances from a point source or at very short times after the introduction of a point source (Kaminski, 1990). An estimate for the speed of heat propagation in materials, v, may be found,(Baumeister and Hamill, 1969) and for steel this estimate predicts a speed of heat propagation on the order of 10^3 m/s.

Zehnder and Rosakis (1991) and Mason and Rosakis (1991) have measured the temperature at the tip of a dynamically propagating crack for crack tip velocities ranging from 600 to 900 m/s in 4340 steel. The temperature fields show a strong difference in their geometric nature, see Figure 3.1, and, since these velocities are comparable to the estimate for the wave speed of heat propagation, it is suggested that this difference may be due to hyperbolic heat conduction. In order to determine whether hyperbolic heat conduction is active in these experiments, it is the purpose of this investigation to produce theoretical temperature fields for the problem of a crack propagating in a hyperbolically conducting metal. It is fundamentally important to note that the propagation of a crack produces plastic deformation at the crack tip and that the plastic work generated during this deformation is mostly transformed into heat. Therefore, the problem of calculating the temperature field around a propagating crack tip is more correctly stated as the problem of calculating the temperature field around a propagating heat source zone with careful attention paid to the boundary conditions at the crack faces.

Several investigations of the temperature field around a propagating crack have been reported for parabolic heat conduction. (For a complete review of this field of work see Mason and Rosakis (1991).) The most pertinent here is the work of Weichert and Schonert (1978). These authors numerically calculated the temperature fields around

propagating heat source zones by integrating the solution of the parabolic heat conduction equation for a travelling point source over a rectangular heat source zone of constant magnitude. A similar methodology is used here. The dynamic crack is modelled two-dimensionally by a heat source zone, the crack tip plastic zone, propagating at a constant velocity with a trailing line of insulated crack faces. (The velocity is a significant fraction of the shear wave speed in the material making it a dynamic crack.) It is assumed that the crack faces do not open. It should be noted that in all theoretical investigations of the temperature field around a propagating crack tip the assumptions made about the plastic work zone and, consequently, the heat source zone have proven to be extremely important in the calculation of maximum temperature. Due to the complexity of the three-dimensional deformation where temperature measurements are performed (at the surface of the specimen), it is difficult to accurately describe the plastic work zone in closed form and most assumptions result in an oversimplification of the experimental problem. Consequently, in this work the shape of the plastic work zone is estimated from the experiments of Zehnder and Rosakis (1991) and Mason and Rosakis (1991) directly, eliminating over-simplification and, thus, more closely approximating the experimental data. The effects of shear lip formation, reverse plasticity upon material unloading, etc. are implicitly accounted for in the experimental approximation of the active plastic zone.

3.2 Theoretical Development

First it is necessary to find the solution of the hyperbolic heat conduction equation for a point source travelling at constant velocity. Although earlier attempts to provide solutions of Eq (3.2) for a traveling point source exist, (Tzou, 1989a and 1989b) the solution given here includes some corrections that significantly alter the behavior of the solution.

We are interested in solving the equation,

$$\nabla_{\mathbf{z}}^2 T - \frac{1}{v^2}\ddot{T} - \frac{1}{\alpha}\dot{T} = -\frac{1}{\rho c_p \alpha}\left[S(z_1 - \dot{a}t, z_2) + \frac{\alpha}{v^2}\dot{S}(z_1 - \dot{a}t, z_2)\right], \tag{3.3}$$

for a point source travelling at a constant velocity, $\dot{a}$, in the z_1 direction, i.e.,

$$S(z_1 - \dot{a}t, z_2) = \delta(z_1 - \dot{a}t)\delta(z_2).$$

Substituting for $S(z_1 - \dot{a}t, z_2)$, Eq (3.3) becomes:

$$\nabla_{\mathbf{z}}^2 T - \frac{1}{v^2}\ddot{T} - \frac{1}{\alpha}\dot{T} = -\frac{1}{\rho c_p \alpha}\left[\delta(z_1 - \dot{a}t)\delta(z_2) + \frac{\alpha}{v^2}\frac{\partial\delta(z_1 - \dot{a}t)}{\partial t}\delta(z_2)\right]. \tag{3.4}$$

It may be shown that the solution of this equation depends upon M^2, where $M = \dot{a}/v$, and that this dependence may be divided into three regimes, $M^2 < 1$, $M^2 = 1$ and $M^2 > 1$. The former and latter cases will be addressed here.

3.2.1 For the Case $M^2 < 1$

By employing the transformation,

$$\xi_1 = \frac{z_1 - \dot{a}t}{\sqrt{1 - M^2}},$$
$$\xi_2 = z_2$$

equation (3.4) may be expressed as

$$\nabla_{\xi}^2 T + \frac{\dot{a}}{\alpha\sqrt{1 - M^2}}\frac{\partial T}{\partial \xi_1} = -\frac{1}{\rho c_p \alpha}\left[\delta(\xi_1\sqrt{1 - M^2})\delta(\xi_2) - \frac{\alpha M^2}{\dot{a}\sqrt{1 - M^2}}\frac{\partial\delta(\xi_1\sqrt{1 - M^2})}{\partial \xi_1}\delta(\xi_2)\right]. \tag{3.5}$$

We guess a solution to Eq (3.5) of the form

$$T_p(\xi_1, \xi_2) = \exp\left[-\kappa\xi_1\right] f\left(\xi_1, \xi_2\right) \tag{3.6}$$

where

$$\kappa = \frac{\dot{a}}{2\alpha\sqrt{1 - M^2}}$$

which when inserted in equation (3.5) yields

$$\nabla_\xi^2 f - \kappa^2 f = -\frac{1}{\rho c_p \alpha}\exp\left[\kappa\xi_1\right] \left\{\delta(\xi_1\sqrt{1-M^2})\delta(\xi_2) - \frac{\alpha M^2}{\dot{a}\sqrt{1-M^2}}\frac{\partial\delta(\xi_1\sqrt{1-M^2})}{\partial\xi_1}\delta(\xi_2)\right\}. \tag{3.7}$$

The left-hand side of Eq (3.7) is the modified Helmholtz equation. The Green's function solution of this equation is given by Arfken (1985),

$$G(\mathbf{r}^\xi, \mathbf{r}^\zeta) = -\frac{1}{2\pi}K_0(\kappa|\mathbf{r}^\xi - \mathbf{r}^\zeta|) \tag{3.8}$$

where $K_0(w)$ is the zeroth order modified Bessel's function of the second kind and

$$|\mathbf{r}^\xi - \mathbf{r}^\zeta| = \sqrt{(\xi_1-\zeta_1)^2 + (\xi_2-\zeta_2)^2}.$$

The first vector, $\mathbf{r}^\xi$ refers to the point of interest while the second vector, $\mathbf{r}^\zeta$, refers to the location of the point source. Using the Green's function for the modified Helmholtz equation, the solution to equation (3.7) may be found,

$$f(\xi_1,\xi_2) = \frac{1}{2\pi\rho c_p\alpha}\int_{A^\zeta} K_0(\kappa|\mathbf{r}^\xi - \mathbf{r}^\zeta|)\exp\left[\kappa\zeta_1\right]\delta(\zeta_1\sqrt{1-M^2})\delta(\zeta_2)d\zeta_1 d\zeta_2 - \frac{1}{2\pi\rho c_p\alpha}\frac{\alpha M^2}{\dot{a}\sqrt{1-M^2}}\int_{A^\zeta} K_0(\kappa|\mathbf{r}^\xi - \mathbf{r}^\zeta|)\exp\left[\kappa\zeta_1\right]\frac{\partial\delta(\zeta_1\sqrt{1-M^2})}{\partial\zeta_1}\delta(\zeta_2)d\zeta_1 d\zeta_2. \tag{3.9}$$

Equation (3.9) may be divided into two integrals

$$f(\xi_1,\xi_2) = \frac{1}{2\pi\rho c_p\alpha}\left(J_1(\xi_1,\xi_2) + J_2(\xi_1,\xi_2)\right). \tag{3.10}$$

The first of these integrals is found using the fundamental property of the Dirac delta function,

$$J_1(\xi_1,\xi_2) = \frac{K_0(\kappa|\mathbf{r}^\xi|)}{\sqrt{1-M^2}}, \tag{3.11}$$

and the second may be found using the relation

$$\int G(\xi_1,\xi_2,\zeta_1,\zeta_2)\frac{\partial\delta(\zeta_1)}{\partial\zeta_1}\delta(\zeta_2)d\zeta_1 d\zeta_2 = -\left\{\frac{\partial G(\xi_1,\xi_2,\zeta_1,\zeta_2)}{\partial\zeta_1}\right\}_{\zeta_1=0,\zeta_2=0},$$

i.e.,

$$J_2(\xi_1,\xi_2) = \frac{M^2}{2(1-M^2)^{3/2}}\left\{K_0(\kappa|\mathbf{r}^\xi|) + \frac{\xi_1}{|\mathbf{r}^\xi|}K_1(\kappa|\mathbf{r}^\xi|)\right\}. \tag{3.12}$$

Substituting Eqs (3.11) and (3.12) into Eq (3.10) gives the result

$$f(\xi_1,\xi_2) == \frac{1}{4\pi\rho c_p\alpha(1-M^2)^{3/2}}\left\{(2-M^2)K_0(\kappa|\mathbf{r}^\xi|) + M^2\frac{\xi_1}{|\mathbf{r}^\xi|}K_1(\kappa|\mathbf{r}^\xi|)\right\}. \tag{3.13}$$

Remembering our intial guess for temperature in Eq (3.6), we arrive at the solution to Eq (3.5),

$$T_p(\xi_1,\xi_2) = \frac{1}{4\pi\rho c_p\alpha(1-M^2)^{3/2}}\exp\left[-\kappa\xi_1\right]\left\{(2-M^2)K_0(\kappa|\mathbf{r}^\xi|) + M^2\frac{\xi_1}{|\mathbf{r}^\xi|}K_1(\kappa|\mathbf{r}^\xi|)\right\}, \tag{3.14}$$

where

$$|\mathbf{r}^\xi| = \sqrt{\xi_1^2+\xi_2^2}.$$

This is the solution for hyperbolic two-dimensional heat flow around a point source traveling in a straight line at a constant speed, $\dot{a} < v$, in an infinite body with $T = 0$ as $r \to \infty$. As $M^2 \to 0$ this function gives the solution of Carslaw and Jaeger (1959) for a traveling point source in a parabolically conducting material under identical boundary conditions. This solution differs from the solution provided by Tzou (1989a and 1989b) due to the interpretation of the argument of the modified Bessel's function in Eq (3.8). In the work by Tzou, it appears that the argument of the modified Bessel's function had been interpreted as the difference of the magnitudes of two vectors where it is actually the magnitude of the difference of two vectors. The additional multiplier of the second term, $\xi_1/|\mathbf{r}^\xi|$, provides desirable behavior for the point source solution not found in the expressions provided by Tzou. Note that using the transformation of coordinates in Eq

(3.3) yields

$$\nabla_\xi^2 T + \frac{\dot{a}}{\alpha\sqrt{1-M^2}}\frac{\partial T}{\partial \xi_1} = \\ -\frac{1}{\rho c_p \alpha}\left[S(\xi_1\sqrt{1-M^2},\xi_2) - \frac{\alpha M^2}{\dot{a}\sqrt{1-M^2}}\frac{\partial S(\xi_1\sqrt{1-M^2},\xi_2)}{\partial \xi_1}\right], \tag{3.15}$$

and that if the slope of the source zone, $S(\xi_1\sqrt{1-M^2},\xi_2)$, is negative in the ξ_1 direction there is a heating contribution due to the second forcing term; if the slope of the source zone in the ξ_1 direction is positive, there is a cooling contribution. The slope of a Dirac delta function in the ξ_1 direction is negative infinite for positive ξ_1 and positive infinite for ξ_1 less that zero (Papoulis, 1962). Consequently, it is expected that there should be a heating contribution ahead of the point source that transforms to a cooling contribution behind the point source. The $\xi_1/|\mathbf{r}^\xi|$ term changes the sign of the second term in the solution to produce this behavior.

On the crack faces it is expected that the heat flux out of the material is zero, that is,

$$q_2 = 0 \begin{cases} \text{for } \xi_2 = 0^+ \text{ and } \xi_1 \le 0; \\ \text{for } \xi_2 = 0^- \text{ and } \xi_1 \le 0. \end{cases} \tag{3.16}$$

Naturally, this is an idealization of the actual boundary condition which would involve radiation transfer, convective transfer etc. However, it is clear that a fixed temperature over the entire crack faces is not an appropriate boundary condition and is not included in this analysis. In parabolic heat conduction, symmetry of the temperature solution about the x_1 axis is sufficient to satisfy the boundary condition at the crack faces given by Eq (3.16),

$$-k\frac{\partial T}{\partial \xi_2}\bigg|_{\xi_2=0} = q_2(\xi_1,0) = 0.$$

However, for hyperbolic heat conduction the symmetry results in a first-order differential equation, namely,

$$\frac{-\dot{a}\alpha}{v^2\sqrt{1-M^2}}\frac{\partial q_2}{\partial \xi_1}\bigg|_{\xi_2=0} + q_2(\xi_1,0) = 0.$$

It is obvious from Eq (3.16) that $q_2 = 0$ is the solution to this equation since the material is in thermal equilibrium at a constant temperature when $\xi_1 = \pm\infty$. However, it is clear that in hyperbolic heat conduction symmetry about the ξ_1 axes does not, by itself, imply that q_2 is identically zero on the ξ_1 axis.

3.2.2 For the Case $M^2 > 1$

By employing the transformation,

$$\xi_1 = \frac{z_1 - \dot{a}t}{\sqrt{M^2 - 1}},$$
$$\xi_2 = z_2$$

Eq (3.4) may be reformulated as

$$-\frac{\partial^2 T}{\partial \xi_1^2} + \frac{\partial^2 T}{\partial \xi_2^2} + \frac{\dot{a}}{\alpha\sqrt{M^2-1}}\frac{\partial T}{\partial \xi_1} = -\frac{1}{\rho c_p \alpha}\left[\delta(\xi_1\sqrt{M^2-1})\delta(\xi_2) - \frac{\alpha M^2}{\dot{a}\sqrt{M^2-1}}\frac{\partial \delta(\xi_1\sqrt{M^2-1})}{\partial \xi_1}\delta(\xi_2)\right]. \tag{3.17}$$

We guess a solution to Eq (3.17) of the form

$$T_p(\xi_1, \xi_2) = \exp[\kappa\xi_1]\, f(\xi_1, \xi_2) \tag{3.18}$$

where

$$\kappa = \frac{\dot{a}}{2\alpha\sqrt{M^2-1}}$$

and substitute above resulting in

$$\frac{\partial^2 f}{\partial \xi_1^2} - \frac{\partial^2 f}{\partial \xi_2^2} - \kappa^2 f = \frac{1}{\rho c_p \alpha}\exp[-\kappa\xi_1]\left\{\delta(\xi_1\sqrt{M^2-1})\delta(\xi_2) - \frac{\alpha M^2}{\dot{a}\sqrt{M^2-1}}\frac{\partial \delta(\xi_1\sqrt{M^2-1})}{\partial \xi_1}\delta(\xi_2)\right\}. \tag{3.19}$$

The left-hand side of this equation is the telegraph equation. The Green's function for this equation may be found in Duff and Naylor (1966),

$$G(\mathbf{r}^\xi, \mathbf{r}^\zeta) = \frac{1}{2} I_0(\kappa|\mathbf{r}^\xi - \mathbf{r}^\zeta|) H(|\mathbf{r}^\xi - \mathbf{r}^\zeta|^2) H(\zeta_1 - \xi_1) \tag{3.20}$$

where I_0 is the zeroth order modified Bessel function of the first kind, $H(x)$ is the Heaviside function and

$$|\mathbf{r}^{\xi} - \mathbf{r}^{\zeta}| = \sqrt{(\xi_1 - \zeta_1)^2 - (\xi_2 - \zeta_2)^2}.$$

Because of the Heaviside terms, the solution in Eq (3.20) is zero outside a triangular regime behind the point source. There exists another Green's function that is non-zero ahead of the point source, but this function is not used due to obvious physical arguments. Because the point source is travelling faster than the wave speed of heat propagation in the material, it is physically impossible to have a finite temperature ahead of the point source. Also, due to the Heaviside terms, the temperature exhibits a jump or shock along lines inclined at an angle ω to the negative ξ_1 axis. The shock angle, ω, is given by the familiar formula,

$$\omega = \pm \sin^{-}1(1/M). \tag{3.21}$$

Not surprisingly, these thermal shocks are quite similar to the shocks found in supersonic fluid flow. This is to be expected since Eq (3.2) is, in fact, the damped wave equation.

Convolution of the Green's function for the telegraph equation with the forcing term in Eq (3.17) results in two integrals. As before, the first of these integrals is found using the fundamental property of the Dirac delta function,

$$J_1(\xi_1, \xi_2) = \frac{I_0(\kappa|\mathbf{r}^{\xi}|)}{\sqrt{M^2 - 1}}, H(|\mathbf{r}^{\xi}|^2) H(-\xi_1).$$

The second integral is found using the additional relation $\delta(x - c)\delta(x) = 0$,

$$J_2(\xi_1, \xi_2) = -\frac{M^2}{2(M^2 - 1)^{3/2}} \left\{ I_0(\kappa|\mathbf{r}^{\xi}|) + \frac{\xi_1}{|\mathbf{r}^{\xi}|} I_1(\kappa|\mathbf{r}^{\xi}|) \right\} H(|\mathbf{r}^{\xi}|^2) H(-\xi_1).$$

Combining these two gives the result

$$f(\xi_1, \xi_2) =$$
$$\frac{1}{4\rho c_p \alpha (M^2 - 1)^{3/2}} \left\{ (M^2 - 2) I_0(\kappa|\mathbf{r}^{\xi}|) - M^2 \frac{\xi_1}{|\mathbf{r}^{\xi}|} I_1(\kappa|\mathbf{r}^{\xi}|) \right\} H(|\mathbf{r}^{\xi}|^2) H(-\xi_1).$$

Remembering our intial guess for temperature in Eq (3.18), we arrive at the final result,

$$T_p(\xi_1,\xi_2) = \frac{1}{4\rho c_p \alpha (M^2-1)^{3/2}} \exp\left[\kappa\xi_1\right] \cdot \left\{ (M^2-2) I_0(\kappa|\mathbf{r}^\xi|) - M^2 \frac{\xi_1}{|\mathbf{r}^\xi|} I_1(\kappa|\mathbf{r}^\xi|) \right\} H(|\mathbf{r}^\xi|^2) H(-\xi_1). \tag{3.22}$$

This is the solution of Eq (3.5) for a point source travelling at constant velocity with $M^2 > 1$. It differs significantly from the solution reported by Tzou (1989a and 1989b) due to the use of the correct Green's function solution for the telegraph equation. It must be re-emphasized that the definition of the argument of the modified Bessel's functions, $|\mathbf{r}^\xi|$, is significantly different in this case than in the previous case, and, furthermore, that the sign of the argument of the leading exponential term has changed. Although the two solutions appear similar, they are, in fact, not very similar at all; for example, this solution does not converge to the solution of Carslaw and Jaeger (1959) under any circumstances. Note the effect of the cooling term in the forcing function on the right-hand side of equation (3.17), when $M^2 < 2$ the temperature at the location of the point source is negative due to the fact that $I_1(w) \to 0$ as $w \to 0$ while $I_0(w) \to 1$ as $w \to 0$. If the cooling term in the forcing function of Eq (3.17) were neglected this effect would not be observed. When $M^2 > 2$, the solution is always positive.

3.2.3 Integration over the Source Zone

For the sake of simplicity the heat source zone, $S(\xi_1,\xi_2)$, has been assumed to be defined only on the rectangle $\xi_1 \in [0, \delta/\sqrt{1-M^2}]$ and $\xi_2 \in [-f\delta, f\delta]$ where f is the aspect ratio of the zone; elsewhere it is identically zero. From the experimental work of Zehnder and Rosakis (1991) and Mason and Rosakis (1991) it is seen that a close approximation to the experimental heat source zone is given by

$$\frac{S(\xi_1,\xi_2)}{Q} = \frac{1}{2f}\left[1 - \cos\left(\frac{2\pi\sqrt{1-M^2}\xi_1}{\delta}\right)\right]\left[1 + \cos\left(\frac{\pi\xi_2}{f\delta}\right)\right],$$

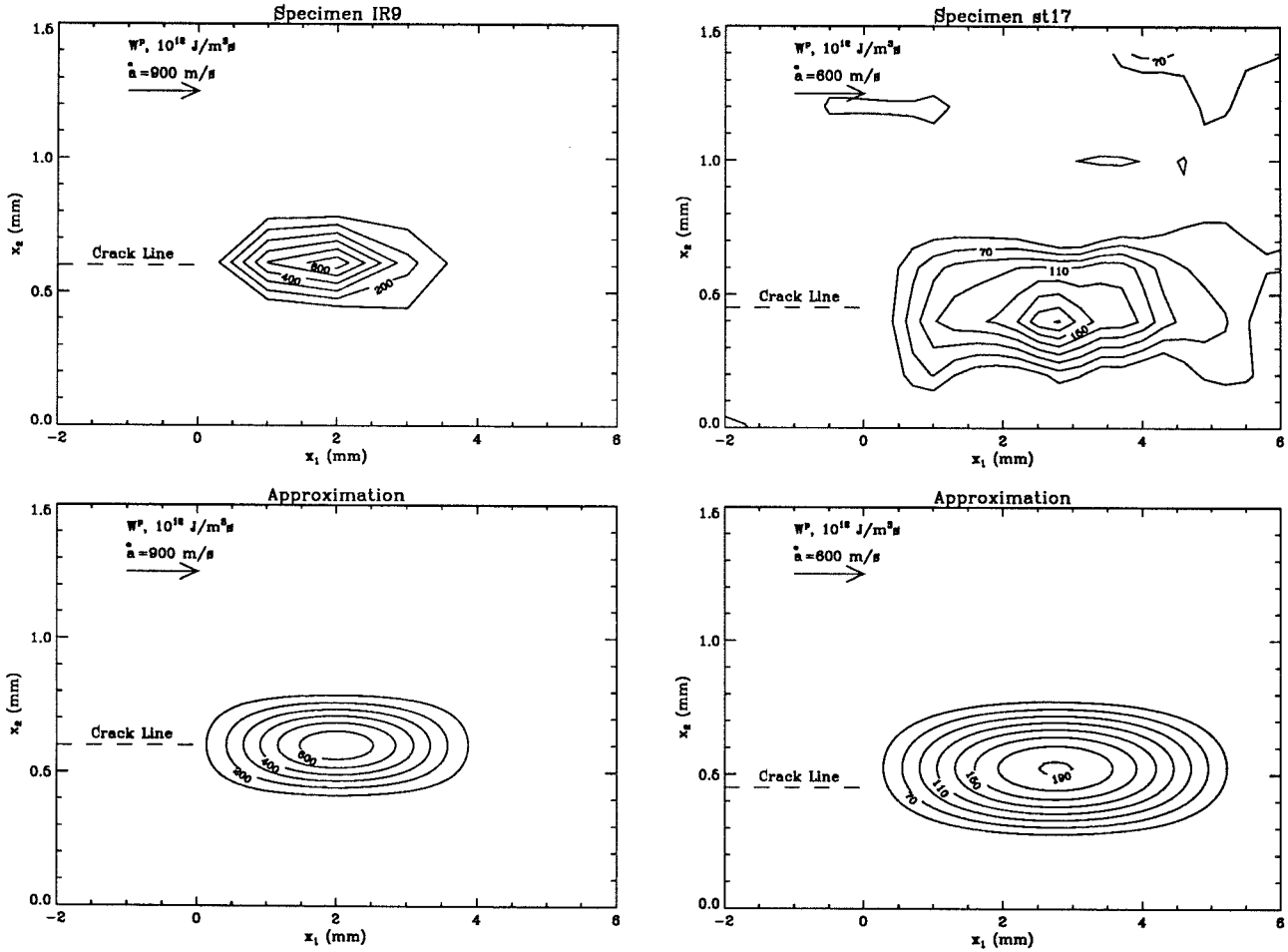

FIGURE 3.2 Experimental measurements and theoretical approximations to the plastic work zone on the surface of oil-quenched 4340 steel during dynamic fracture. At 900 m/s the work zone is smaller (Zehnder and Rosakis, 1991) than the work zone at 600 m/s.(Mason and Rosakis, 1991) For each experiment the aspect ratio is the same, $f = .05$, but the size, δ differs. At 900 m/s $\delta = 5.0$; at 600 m/s $\delta = 7.5$.(See section 2.3.)

where $f = 0.05$. A comparison of the approximate plastic zone, $S(\xi_1, \xi_2)$, with the experimentally estimated plastic zone is shown in Figure 3.2 for both testing conditions. Following the work of Bever et al. (1973) it is assumed that 90% of the plastic work is converted to heat. The inclusion of $1/2f$ in the denominator gives this function characteristics of a Dirac delta function in the ξ_2 (or x_2, given below) direction as $f \to 0$. Consequently, this function is also normalized so that its integral in two dimensions is unity giving usable results if f is allowed to be zero. The multiplier, Q, is found experimentally from the maximum value of the work rate density and the relation between Q and the maximum of the function,

$$Q = \frac{fQ_{max}}{2}.$$

Once this relation for the heat source zone has been assumed, letting

$$\begin{aligned} x_1 = \zeta_1 &= \sqrt{1 - M^2}\frac{\xi_1}{\delta}, \\ x_2 = \zeta_2 &= \frac{\xi_2}{\delta}, \end{aligned} \tag{3.23}$$

the temperature field due to the heat source zone ahead of a crack tip may be found by a convolution;

$$T(x_1, x_2) = Q\delta^2 \int_0^1 \int_{-f}^{f} \frac{S(\zeta_1, \zeta_2)}{Q} T_p(x_1 - \zeta_1, x_2 - \zeta_2) d\zeta_2 d\zeta_1,$$

or, more specifically, for $M^2 < 1$

$$\begin{aligned} T(x_1, x_2) = &\frac{Q\delta^2}{4\pi\rho c_p \alpha (1 - M^2)^{3/2}} \cdot \\ &\int_0^1 \int_{-f}^{f} \frac{S(\zeta_1, \zeta_2)}{Q} \exp\left[\frac{-\psi(x_1 - \zeta_1)}{1 - M^2}\right] \cdot \\ &\left\{(2 - M^2) K_0\left(\frac{\psi|\mathbf{r}^{\mathbf{x}} - \mathbf{r}^{\boldsymbol{\zeta}}|}{1 - M^2}\right) + M^2 \frac{(x_1 - \zeta_1)}{|\mathbf{r}^{\mathbf{x}} - \mathbf{r}^{\boldsymbol{\zeta}}|} K_1\left(\frac{\psi|\mathbf{r}^{\mathbf{x}} - \mathbf{r}^{\boldsymbol{\zeta}}|}{1 - M^2}\right)\right\} d\zeta_2 d\zeta_1, \end{aligned} \tag{3.24a}$$

where

$$\begin{aligned} \psi &= \frac{\dot{a}\delta}{2\alpha} \\ |\mathbf{r}^{\mathbf{x}} - \mathbf{r}^{\boldsymbol{\zeta}}| &= \sqrt{(x_1 - \zeta_1)^2 + (1 - M^2)(x_2 - \zeta_2)^2} \end{aligned} \tag{3.24b}$$

Normalizing temperature with respect to $Q\delta/\rho c_p \dot{a}$ for numerical integration yields

$$\theta(x_1,x_2)=\frac{\rho c_p\dot{a}}{Q\delta}T(x_1,x_2)=\frac{\psi}{2\pi(1-M^2)^{3/2}}\cdot$$
$$\int_0^1\int_{-f}^{f}\frac{S(\zeta_1,\zeta_2)}{Q}\exp\left[\frac{-\psi(x_1-\zeta_1)}{1-M^2}\right]\cdot$$
$$\left\{(2-M^2)K_0(\frac{\psi|\mathbf{r^x}-\mathbf{r^\zeta}|}{1-M^2})+M^2\frac{(x_1-\zeta_1)}{|\mathbf{r^x}-\mathbf{r^\zeta}|}K_1(\frac{\psi|\mathbf{r^x}-\mathbf{r^\zeta}|}{1-M^2})\right\}d\zeta_2 d\zeta_1. \tag{3.25a}$$

Similarly for $M^2>1$

$$\theta(x_1,x_2)=\frac{\psi}{2(M^2-1)^{3/2}}$$
$$\int_0^1\int_{-f}^{f}\frac{S(\zeta_1,\zeta_2)}{Q}\exp\left[\frac{-\psi(x_1-\zeta_1)}{M^2-1}\right]\cdot \tag{3.25b}$$
$$\left\{(M^2-2)I_0\left(\frac{\psi|\mathbf{r^x}-\mathbf{r^\zeta}|}{M^2-1}\right)-M^2\frac{(x_1-\zeta_1)}{|\mathbf{r^x}-\mathbf{r^\zeta}|}I_1\left(\frac{\psi|\mathbf{r^x}-\mathbf{r^\zeta}|}{M^2-1}\right)\right\}$$
$$H(|\mathbf{r^x}-\mathbf{r^\zeta}|^2)H(-x_1+\zeta_1).d\zeta_2 d\zeta_1.$$

Numerical integration of the solution for $M^2<1$ proceeds without avail. The singularity in the modified Bessel's function of the zeroth order at the origin is logarithmic, therefore the integral is finite. The singularity in the modified Bessel's function of the first order at the same point is of order $1/|\mathbf{r^x}-\mathbf{r^\zeta}|$ which is integrable in two dimensions. (This is easily shown by a conversion to polar coordinates.) Multiplication of $K_1(\psi|\mathbf{r^x}-\mathbf{r^\zeta}|)$ by the factor $(x_1-\zeta_1)/|\mathbf{r^x}-\mathbf{r^\zeta}|$ does not change the order of the singularity of this term since at $(x_1-\zeta_1)=(x_2-\zeta_2)=0$ this term is finite. For $M^2>1$, the integration is quite simple. Since both modified Bessel functions of the first kind are finite at the origin, the only singularity occurs in the second term and this remains integrable. (This is easily shown using polar coordinates.)

The convolution, Eq (3.24a), is evaluated numerically for $\psi\in[.01,1,100]$ and $M^2\in[0,.5,.9,100,10^4]$. The modified Bessel's functions are evaluated either by using IMSL subroutines for small arguments or by using the asymptotic expressions given below for larger arguments. To find the value of the integral a two-dimensional

Gauss-Legendre scheme is employed. The number of integration points increased with the value of ψ.

3.2.4 Asymptotic Analysis of the Integration

By employing the transform

$$x_1 = \frac{z_1 - \dot{a}t}{\delta}$$
$$x_2 = \frac{z_2}{\delta}$$

in Eqs (3.1) and (3.2) the following expressions are found;

$$\frac{1}{2\psi}\nabla_{\mathbf{x}}^2 T + \frac{\partial T}{\partial x_1} = -\frac{\delta}{\dot{a}\rho c_p} S \tag{3.26a}$$

and

$$\frac{1}{2\psi}\nabla_{\mathbf{x}}^2 T - \frac{M^2}{2\psi}\frac{\partial^2 T}{\partial x_1^2} + \frac{\partial T}{\partial x_1} = -\left(\frac{\delta}{\dot{a}\rho c_p} S - \frac{M^2}{2\psi}\dot{S}\right), \tag{3.26b}$$

respectively. Note that as the parameter ψ gets large the left-hand sides of both equations become more adiabatic and that the solution to the adiabatic equation is given simply as;

$$\theta_a(x_1, x_2) =$$
$$\begin{cases} \frac{1}{2f}\left(1 + cos(\pi\frac{x_2}{f})\right) & \text{for } x_1 \leq 0 \text{ and } x_2 \in [-f, f], \\ \frac{1}{2f}\left(1 + \cos(\pi\frac{x_2}{f})\right)\left(1 - x_1 + \frac{1}{2\pi}\sin(2\pi x_1)\right) & \text{for } x_1 \in [0, 1],\ x_2 \in [-f, f], \\ 0 & \text{otherwise,} \end{cases} \tag{3.27}$$

where the temperature has been normalized by $Q\delta/\rho c_p \dot{a}$. From the definition of ψ, it is seen that one of three things may be occurring when $\psi \to \infty$: $\alpha \to 0$, $\dot{a} \to \infty$ or $\delta \to \infty$. In Eqs (3.26a) and (3.26b) as $\psi \to \infty$ the left-hand side becomes the adiabatic equation, but, depending upon how ψ is increasing, through α, $\dot{a}$ or δ, the right-hand side may be affected as well. Normalizing the temperature with respect to $Q\delta/\rho c_p \dot{a}$ in Eq. (3.25a) removes this ambiguity in the limit, and, thus, the point source term in the integrand of Eq (3.25a) rather than Eq (3.24a) is examined asymptotically for $M^2 < 1$.

For large arguments the modified Bessel's functions can be approximated by

$$\begin{aligned} K_0(w) &\sim \sqrt{\frac{\pi}{2w}}\exp\left[-w\right]\left\{1-\frac{1}{8w}+\frac{9}{128w^2}+\ldots\right\} \\ K_1(w) &\sim \sqrt{\frac{\pi}{2w}}\exp\left[-w\right]\left\{1+\frac{3}{8w}-\frac{15}{128w^2}+\ldots\right\} \end{aligned} \quad . \tag{3.28}$$

Using only the first terms, the point source in the integrand for $M^2 < 1$, Eq (3.25a), can be rewritten as

$$\theta_p(x_1,x_2) \sim \frac{\psi}{2\pi(1-M^2)}\sqrt{\frac{\pi}{2\psi|\mathbf{r}^{\mathbf{x}}|}}\exp\left[\frac{-\psi(x_1+|\mathbf{r}^{\mathbf{x}}|)}{1-M^2}\right]\left\{2-M^2+M^2\frac{x_1}{|\mathbf{r}^{\mathbf{x}}|}\right\} \tag{3.29}$$

where

$$|\mathbf{r}^{\mathbf{x}}| = \sqrt{x_1^2+(1-M^2)x_2^2}.$$

Given that for small x_2/x_1

$$\exp\left[-\frac{\psi}{1-M^2}|\mathbf{r}^{\mathbf{x}}|\right] \approx \exp\left[-\frac{\psi}{1-M^2}|x_1|\right]\exp\left[-\frac{\psi|x_1|}{2}\left(\frac{x_2}{x_1}\right)^2\right], \tag{3.30}$$

Eq (3.29) may be expanded to take the following form,

$$\begin{aligned} &\theta_p(x_1,x_2) \sim \frac{\psi}{2\pi(1-M^2)}\sqrt{\frac{\pi}{2\psi|x_1|}} \\ &\exp\left[-\frac{\psi}{1-M^2}(x_1+|x_1|)\right]\exp\left[-\frac{\psi|x_1|}{2}\left(\frac{x_2}{x_1}\right)^2\right] \\ &\left\{2-M^2+\mathrm{sgn}(x_1)M^2\right. \\ &\left.-\left[\frac{2\mathrm{sgn}(x_1)M^2(1-M^2)+(2-M^2+\mathrm{sgn}(x_1)M^2)(1-M^2)}{4}\right]\left(\frac{x_2}{x_1}\right)^2\ldots\right. \end{aligned}$$

When $x_1 > 0$ the exponential term $\exp\left[-\psi(x_1+|x_1|)/(1-M^2)\right]$ dominates the solution and $T_p(x_1,x_2) \sim 0$; on the other hand, when $x_1 \leq 0$, $(x_1+|x_1|)=0$, the same exponential term disappears and $\mathrm{sgn}(x_1)$ is always negative. Thus,

$$\theta_p(x_1,x_2) \sim \begin{cases} \sqrt{\frac{\psi}{2\pi|x_1|}}\exp\left[-\frac{\psi}{2|x_1|}x_2^2\right]\left\{1-\frac{(1-2M^2)}{4}\left(\frac{x_2}{x_1}\right)^2+\ldots\right\} & \text{for } x_1<0; \\ 0 & \text{for } x_1>0. \end{cases} \tag{3.31}$$

It is clear that, as $\psi/2|x_1|$ becomes large, the second term in the expansion becomes negligible and the solution becomes independent of M^2 Consequently, the solution for the hyperbolic heat conduction equation and the solution for the parabolic heat conduction equation converge to the same result. It is also clear that as $\psi/2|x_1| \rightarrow \infty$, $\theta_p(x_1, x_2)$ becomes, as expected from the adiabatic solution, a Dirac delta function (Arfken, 1985) in x_2. However, contrary to the solution for the adiabatic equation and in keeping with the boundary condition $T \rightarrow \infty$ as $\mathbf{r}^{\mathbf{x}} \rightarrow \infty$, the function in Eq (3.31) loses its Dirac delta function character as $|x_1|$ grows.

Not surprisingly, similar results are found for the case $M^2 > 1$. Asymptotic analysis using the approximations

$$I_0(w) \sim \sqrt{\frac{1}{2\pi w}} exp[w]$$
$$I_1(w) \sim \sqrt{\frac{1}{2\pi w}} exp[w]$$

and following the same steps outlined above leads to the same leading term characterization of the solution as for the case $M^2 < 1$. Since the governing equation becomes adiabatic as the approximation becomes more accurate it is to be expected that both solutions converge to the same result as they do.

3.3 Results and Discussion

The solution for the simplest case, the adiabatic case in Eq (3.27), is shown in Figure 3.3. Behind the heat source zone the adiabatic solution is characterized by contours of constant temperature extending from the heat source zone to $x_1 = -\infty$ parallel to the crack faces. In front of the crack tip, in the heat source zone, the gradient of temperature along lines extending radially from the crack tip appears to be constant. Although it isn't true mathematically that the radial gradient in the heat source zone is constant, it is noted that the expression for the zone used here is an approximation to

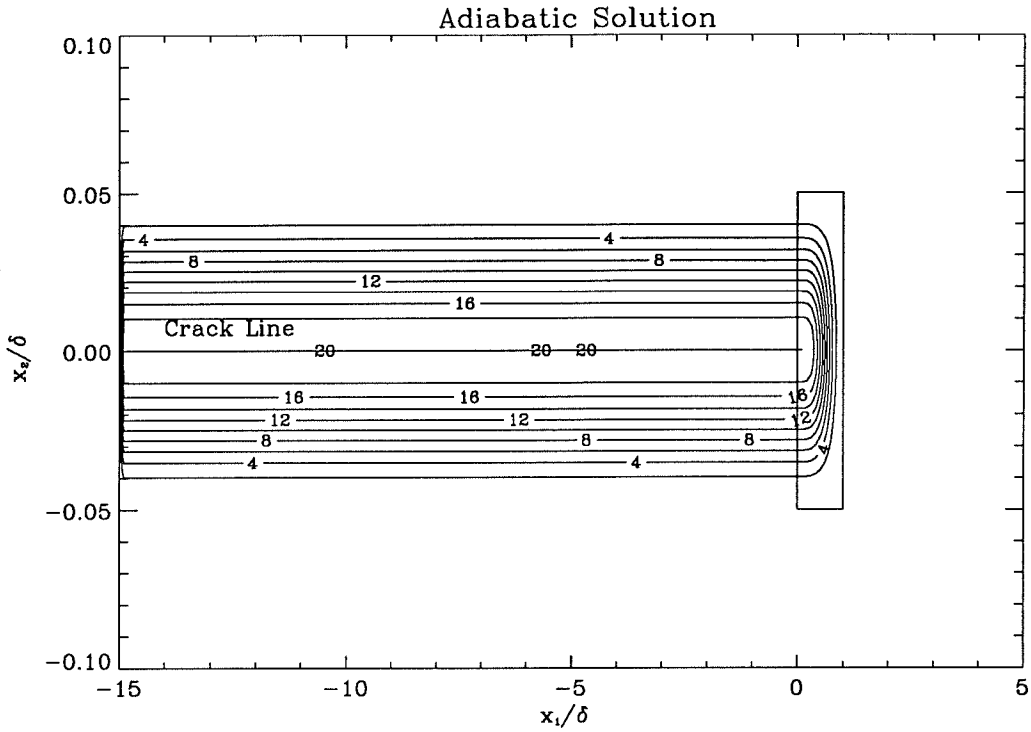

FIGURE 3.3 The temperature field due to the approximate plastic work zone shown in Figure 3.2 for adiabatic conditions. The box indicates the region of non-zero plastic work. (See section 2.3.) Good qualitative and quantitative agreement with the experimental results for $\dot{a} = 600m/s$ are seen. The predicted temperature rise for $\dot{a} = 900m/s$ is also good, however, the shape of the field does not agree with that measured when $\dot{a} = 900m/s$.(See Figure 3.1.)

the experimental data and that "averaging"in the experiments due to the finite infrared detector size reduces the accuracy of the measurements near the crack tip (Zehnder and Kallivayalil, 1991). Generally, it is expected that if adiabatic conditions prevail at the crack tip, a nearly constant radial gradient may be recorded experimentally. Good quantitative agreement is found between the predicted temperature rise and the measured temperature rise. A maximum temperature rise of 298°C is seen in the experiment when $\dot{a}$ =600 m/s, and the predicted result, 304°C occurring along the crack line, is very close to that measurement. The minimum temperature is 0°C occurring everywhere outside—except directly behind—the heat source zone.

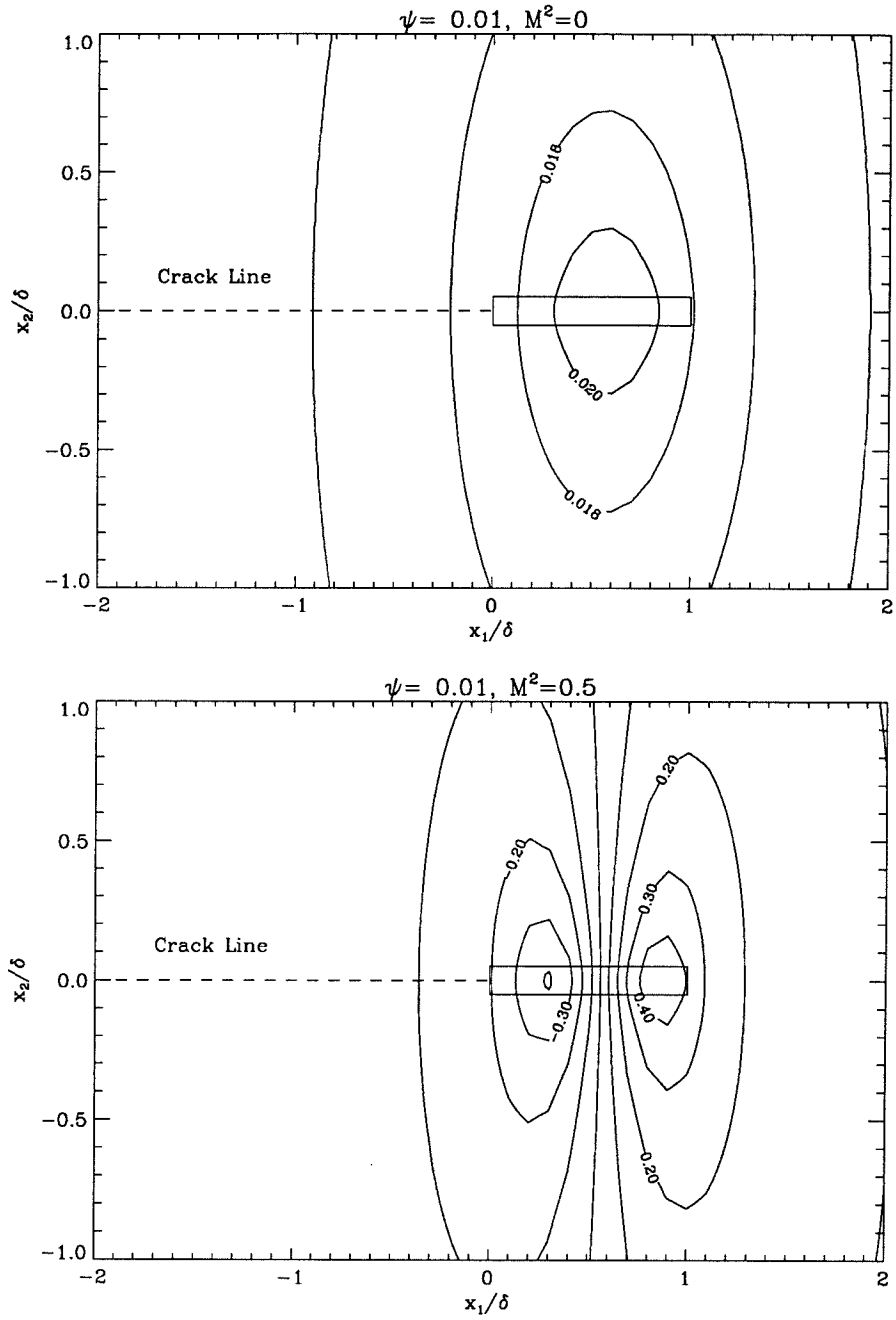

FIGURE 3.4 The normalized temperature field for a propagating source zone with $\psi = .01$ and $M^2 \in [0, .5, .9]$. (See Eqs (3.24a) and (3.24b).) Note that the existence of a temperature drop is exhibited for $M^2 \in [.5, .9]$ and that the temperature field becomes more localized around the source zone with increasing M^2. (a) $M^2 = 0.0$ (b) $M^2 = 0.5$

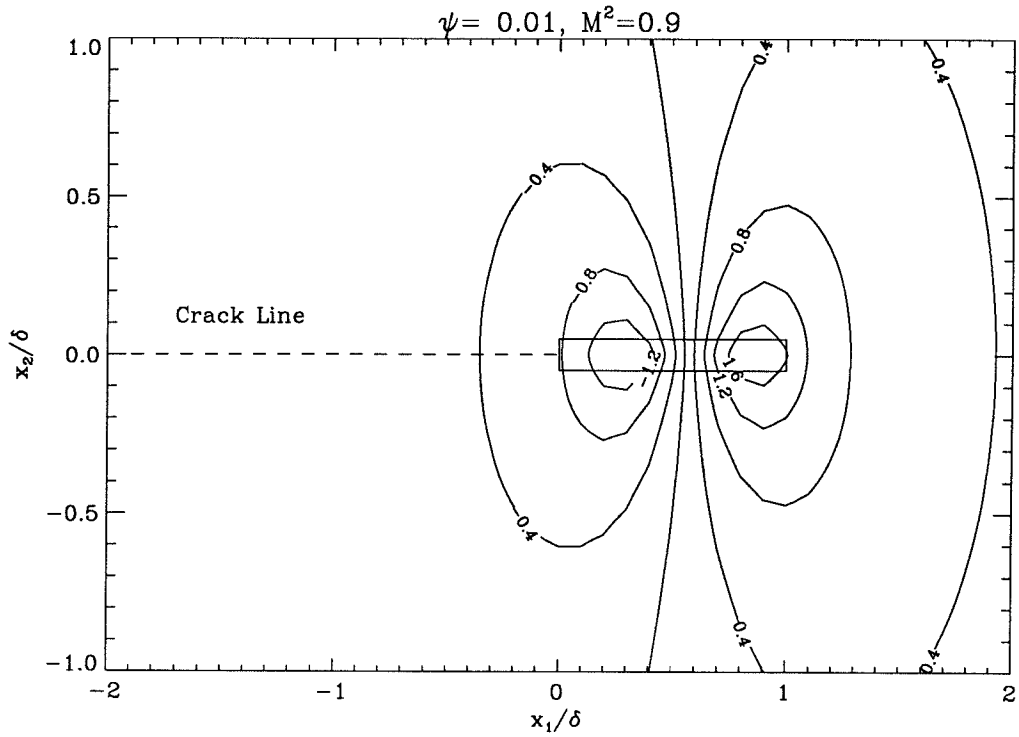

FIGURE 3.4 (c) $M^2 = 0.9$

The results of the numerical integration for the $M^2 < 1$ cases are plotted in Figures 3.4 through 3.6. For small ψ it can be seen in Figure 3.4 that there is a marked dependence of the temperature field upon M^2. Most notably, for $M^2 \in [.5, .9]$ a region of temperature drop is seen behind the source zone. This is an interesting mathematical effect, but the result is unrealistic since the combination of parameters in these plots, $\psi = .01$ and $M^2 \in [.5, .9]$, is unlikely to be seen experimentally. As $M^2 \to 1$ the temperature field becomes more localized near the origin and the temperature at any given point behind the heat source zone decreases with increasing M^2. For $M^2 = 0$ the maximum normalized temperature, θ_{max}, occurs roughly at the maximum of the heat source zone and is equal to .1% of the adiabatic maximum. The minimum, naturally, is zero as $r \to \infty$. For $M^2 = .5$ the maximum is moved forward to roughly the location of the minimum slope of the source zone where θ_{max} is equal to 1% of the adiabatic maximum. The minimum occurs roughly at the location of the maximum

slope of the source zone where the normalized temperature is equal to -1% of the maximum adiabatic temperature. For the case $M^2 = .9$ the location of the maximum and minimum are not changed with respect to the case $M^2 = .5$ but the magnitude does, θ_{max} is equal to 10% of the adiabatic maximum while θ_{min} is equal to -10% of the adiabatic maximum. The behavior seen for the two cases when $M^2 \neq 0$ is exactly as expected from Eqs (3.15) and (3.14). When $M^2 \neq 0$ there is a contribution due to the slope of the heat source zone as seen in Eq (3.15). This contribution has a cooling effect when the slope is a maximum and a heat effect when the slope is a minimum; as $M^2 \rightarrow 1$ the significance of the heating and cooling due to the modified Bessel's function of the first order becomes greater and more dominant. Thus, as $M^2 \rightarrow 1$, the maximum temperature moves to the location of minimum slope and the minimum temperature moves to the location of the maximum slope. Both maximum and minimum increase in magnitude as $M^2 \rightarrow 1$.

For larger ψ, Figure 3.5, the dependence of the temperature field upon M^2 begins to disappear. No negative temperature changes are seen, however, when $M^2 = .9$ the temperature does exhibit a positive minimum near the tail end of the heat source zone. Thus, some cooling effects due to the second source term in Eq (3.15) remain. Although, far from the heat source zone, $x_1/\delta > 1$, all three fields are equal. As $M^2 \rightarrow 1$ a localization of the temperature near the source zone is still seen. The maximum temperature is located near the maximum of the source function in each sub-case although it moves forward slightly as the thermal mach number increases. The maximum normalized temperature increases with thermal mach number; $\theta_{max} = .75, 1, 1.5$ for $M^2 = 0, .5, .9$ respectively. These values are 3.25%, 5% and 7.5% of the maximum temperature under adiabatic conditions.

For even larger ψ, Figure 3.6, the dependence upon M^2 disappears completely as expected from the asymptotic analysis, Eq (3.31), and the hyperbolic heat conduction

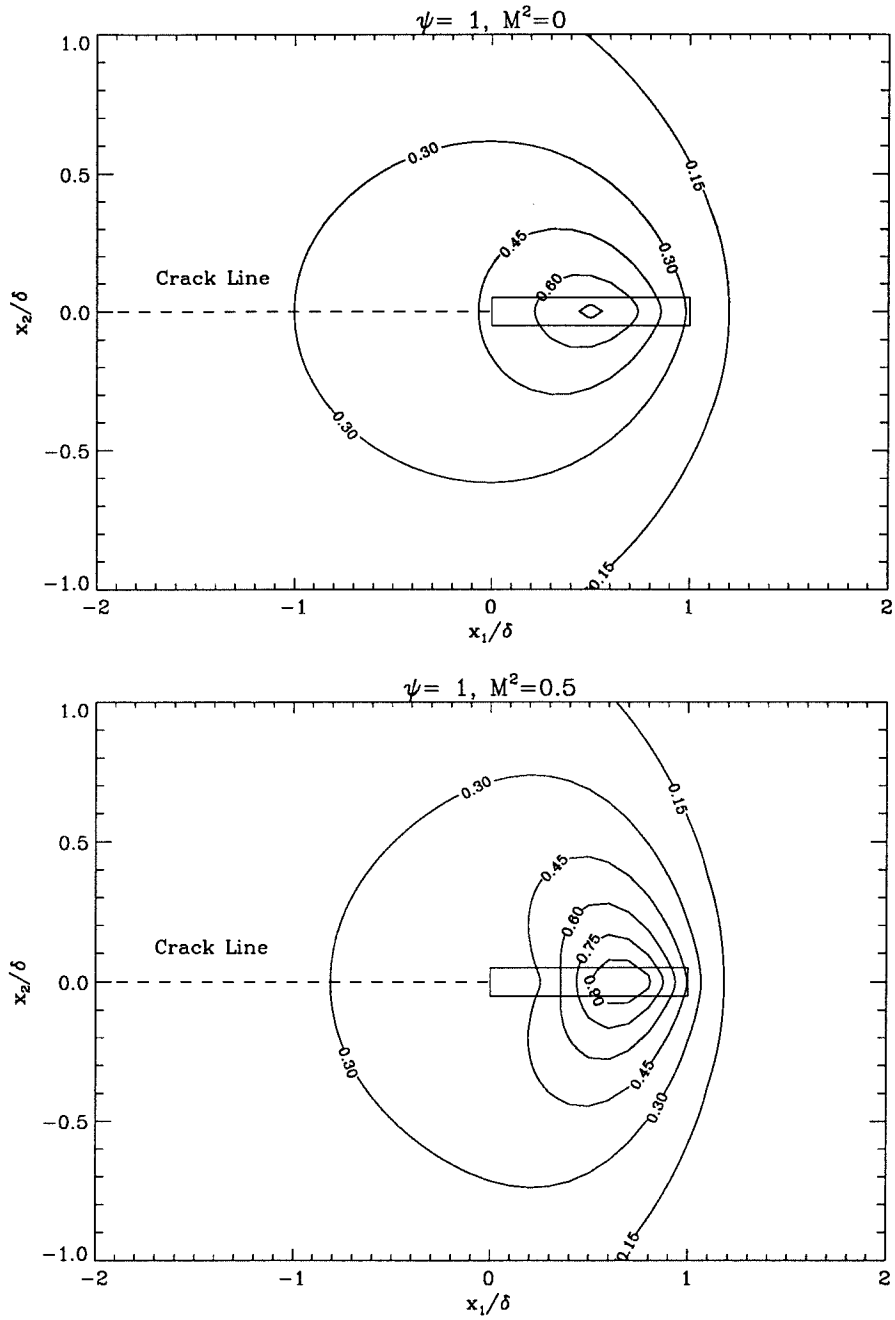

FIGURE 3.5 The normalized temperature field for a propagating source zone with $\psi = 1$ and $M^2 \in [0, .5, .9]$. There exist no temperature drops as for $\psi = .01$ in Figure 3.4., however, the temperature field becomes increasingly localized around the heat source as the thermal Mach number, M, increases leading to higher temperature rises at the maximum. (a) $M^2 = 0.0$ (b) $M^2 = 0.5$

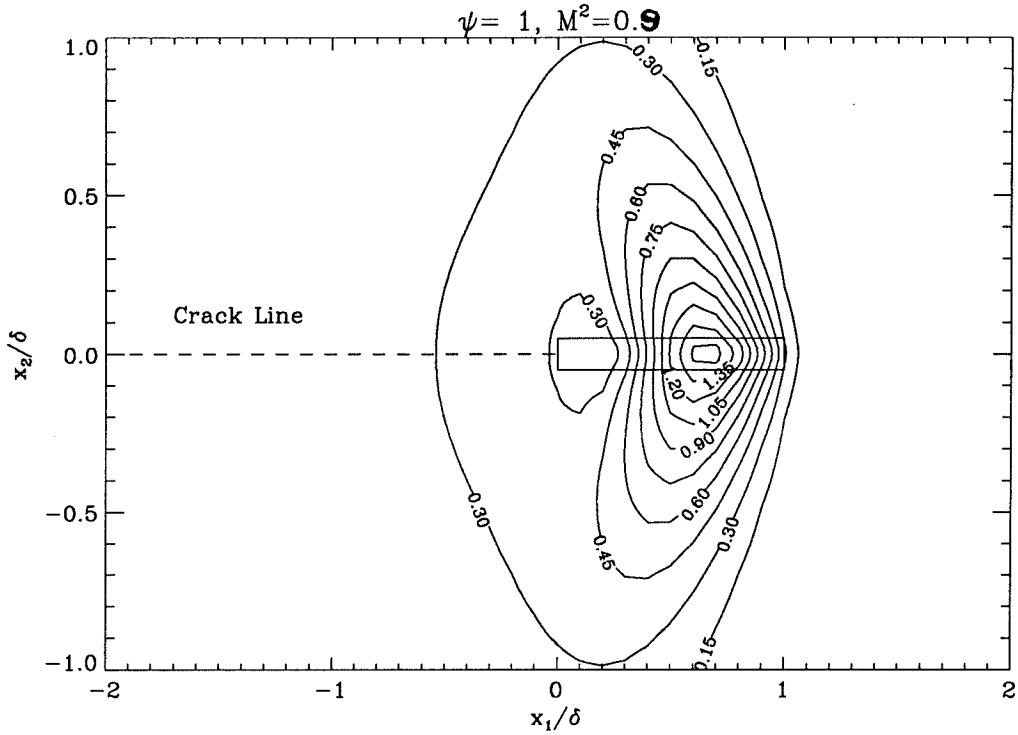

FIGURE 3.5 (c) $M^2 = 0.9$

solution is indistinguishable from the solution for parabolic heat conduction at all values of $M^2 < 1$. No localization of the temperature near the heat source zone is discernable. The maximum temperature occurs slightly behind the maximum of the heat source zone with value of 7.5—32.5% of the maximum temperature under adiabatic conditions.

Small ψ accounts for; a small source zone, δ, low velocity, $\dot{a}$, or a large thermal diffusivity, α. (See Eq (3.24b).) For metals these conditions do not reflect the usual experimental conditions. For 4340 steel, $\alpha = 10^{-5}$, and $\dot{a}\delta \approx 2$ for both experiments shown in Figure 3.1 giving $\psi \sim 10^5$ in both cases. For comparison the results of the integration for $\psi = 10^5$ have been plotted in Figure 3.7. It is seen that the theoretical temperature field matches the experimental results, Figure 3.1, well for $\dot{a} = 600$ m/s and that both the theoretical temperature field and the experimental temperature field resemble the adiabatic solution, Figure 3.3. Contours extend from the heat source zone nearly parallel to the crack faces toward $x_1 = -\infty$ before curving in to meet the

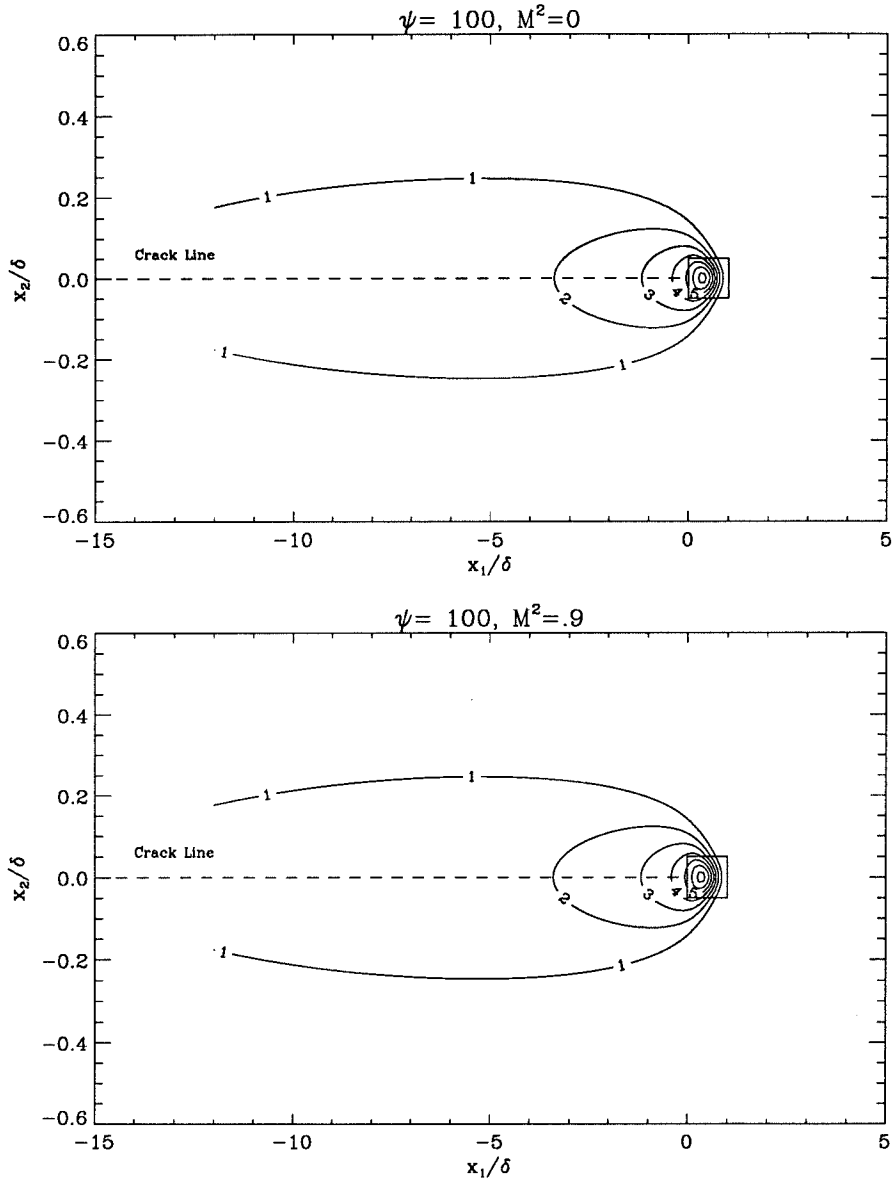

FIGURE 3.6 The normalized temperature field for a propagating source zone with $\psi = 100$ and $M^2 \in [0, .9]$. The two fields are virtually indistinguishable. No dependence upon M^2 is seen.

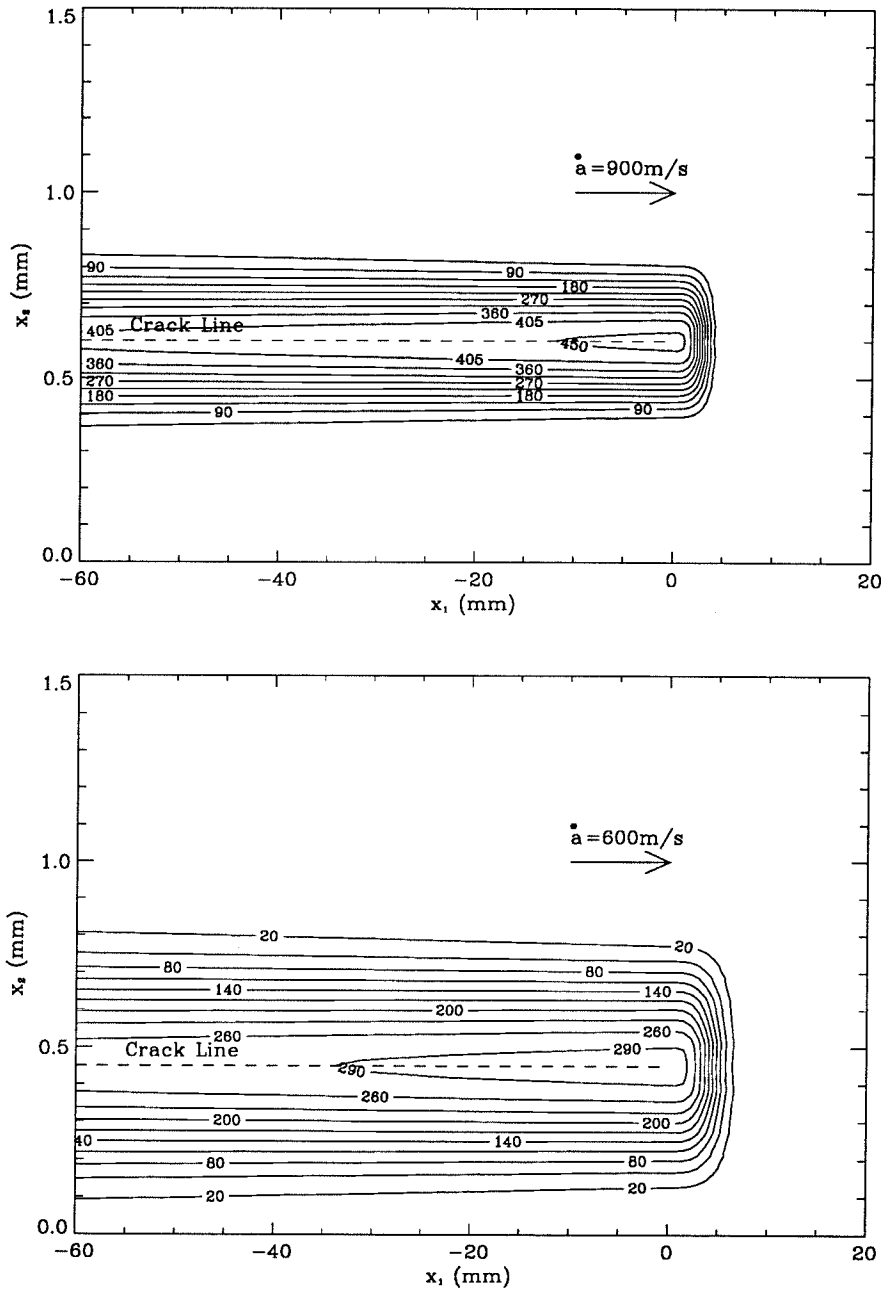

FIGURE 3.7 The theoretical temperature fields for approximate experimental conditions when $\dot{a}$= 900 m/s and 600 m/s. Good agreement is seen in the predicted maximum temperature at the crack tip, however some discrepancies occur between the general shape of the field in this figure and the temperature fields shown in Figure 3.1. ($\psi = 10^5$, $\delta = 7.5$ mm for $\dot{a} = 600$ m/s and $\delta = 5$ mm for $\dot{a} = 900$ m/s.)

negative x_1 axis. The results for $\psi = 10^5$ differ from the adiabatic solution in that the temperature decreases as $|x_1|$ increases behind the heat source zone. It is reiterated that this decrease is expected due to the zero temperature boundary condition at $|x_1| = \infty$. This boundary condition more closely approximates the experimental condition than an adiabatic boundary condition because there is, after all, a small but significant amount of heat conduction leading to a cooling of the specimen as $|x_1| \to \infty$. It is noted that the temperature decreases more rapidly behind the crack tip in the experiments than in the theory. This is attributed to heat loss by radiation and convection at the surface. Kuang and Atluri (1985) have included these effects in there numerical parabolic heat conduction analysis, and they report a more rapid decrease in the temperature behind the crack than when radiation and convection are *not* neglected. For $\dot{a} = 900$ m/s in Figure 3.1 a discrepancy with the theoretical results for $M^2 < 1$ in Figure 3.7 is seen. The contours seen experimentally emanate from the source zone outwardly before curving in to meet the negative x_1 axis. (The predicted maximum temperature at the crack tip is in good agreement with the experimental measurement, however, owing to the adiabatic conditions at the crack tip.)

For $M^2 > 1$ an exemplary plot is shown in Figure 3.8. The resemblance of this figure to the results recorded in Fig 3.1 for $\dot{a} = 900$ m/s is striking, however, the experimental temperature field for $\dot{a} = 900$ m/s shows what might be interpreted to be thermal shocks at a shock angle corresponding to a large mach number, $M \approx 100$. If this value for M is accurate then when $\dot{a} = 600$ m/s the temperature field should also show similar thermal shocks; it doesn't. Also, because $\psi = 10^5$ experimentally not 10^3 as in Fig 3.8, the theoretical temperature field for thermally super-sonic crack propagation at $\dot{a} = 900$ m/s actually resembles the temperature field in Fig 3.7. This is expected from the asymptotic analysis and has been checked numerically by the authors. Therefore, it is clear that no evidence of thermally super-sonic crack propagation is

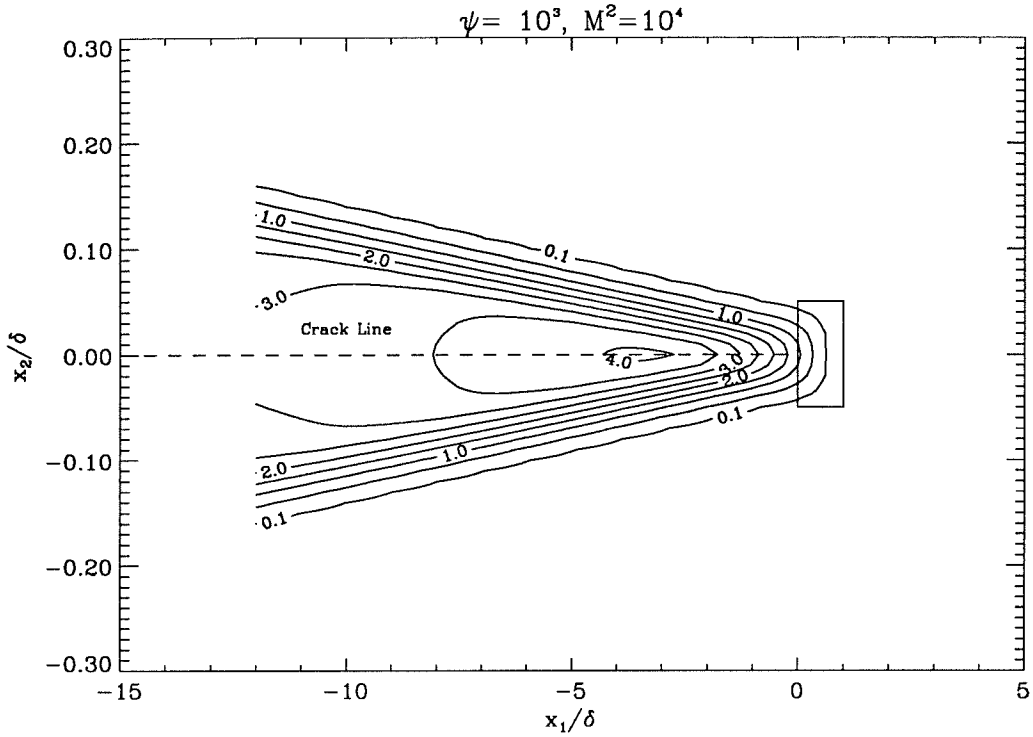

FIGURE 3.8 The theoretical temperature field when $M^2 = 10^4$ and $\psi = 100$ resembles that in Fig 1 when $\dot{a} = 900$ m/s. This resemblance is coincidental, however, because the large value of M^2 indicates thermally supersonic behavior should also be expected when $\dot{a} = 600$ m/s and no such behavior is observed.

observed in these experiments.

The difference between the experimentally observed temperature field at $\dot{a}$ =900 m/s and the predicted field at the same crack speed is due to crack face opening (Mason and Rosakis, 1991). The opening velocity required to produce the observed effect is 7.5 m/s, a reasonable crack opening velocity. It is expected that the crack face opening speed depends upon the initial static stress intensity factor and the crack velocity. From simple theory one might expect that the crack face opening velocity increases by as much as 5 times when the crack speed increases from 600 m/s to 900 m/s (Freund, 1977). This suffices to explain the difference in the temperature fields in Figures 3.1 and 3.7.

3.4 Conclusions

From the asymptotic analysis of the traveling point source solution of the hyperbolic heat conduction equation, it is clear that, for crack propagation in metals when the crack speed is either lower or higher than the material heat propagation speed, the difference between hyperbolic heat conduction and parabolic heat conduction is negligible (see Figures 3.6 and Figure 3.7). As the factor $\psi = \dot{a}\delta/2\alpha$ gets large, ($\psi \sim 10^5$ for a crack propagating in 4340) solutions for a traveling point source in a hyperbolic or parabolic material converge to the same result. This end result is insensitive to changes in the thermal mach number, M, and is very similar to the solution for a traveling source zone in an adiabatic material.

The temperature field in Figure 3.1 exhibits quasi-adiabatic heat conduction behavior when $\dot{a} = 600$ m/s. Contours of constant temperature extend from the crack tip to $|x_1| = -\infty$ nearly parallel to the crack faces before curving in to meet the negative x_1 axis. A region of nearly constant radial temperature gradient is observed ahead of the crack tip. The temperature field greatly resembles the solution for adiabatic conditions due to the high crack velocity, $\dot{a}$, small heat production zone, δ, and low thermal diffusivity, α, of 4340 steel.

When $\dot{a} = 900$ m/s the temperature field does not show behavior that is predicted by parabolic or hyperbolic heat conduction. It is understood that this difference is due to opening of the crack faces behind the crack tip (Mason and Rosakis, 1991). Thus, no evidence of hyperbolic heat conduction is observed, and it is concluded that the traveling point source shows little promise as an experimental method for the investigation of the hyperbolic heat conduction effect. A feasible source zone size combined with the normal range of material parameters for engineering materials consistently leads to near adiabatic conditions around the source zone unless a very low thermal wave speed is expected (~ 1 m/s). Furthermore, it is noted that hyperbolic heat conduction is expected

only at very low temperatures and only for very special materials (S. Nemat-Nasser, 1992) making this phenomenon even less likely to occur under these experimental conditions.

References

1. G. Arfken (1985), *Mathematics for Physicists,* 3rd Edition, Academic Press, Inc., New York, 912

2. K.J. Baumeister and T.D. Hamill (1969), Hyperbolic heat conduction equation—a solution for the semi-infinite body problem, *J. Heat Transfer,* **91,** 543

3. M.B. Bever, D.L. Holt and A.L. Titchener (1973), The stored energy of cold work, *Prog. Mat. Sci.*,**17,** 1

4. H.S. Carslaw and J.C. Jaeger (1959), *Conduction of Heat in Solids,* Oxford University Press, London, 267

5. G.F.D. Duff and D. Naylor (1966), *Differential Equations of Applied Mathematics,* John Wiley & Sons, Inc., New York

6. L.B. Freund (1977), A simple model of the double cantilever beam crack propagation specimen, *J. Mech.Phys. Sol.,* **25,** 69

7. W. Kaminski (1990), Hyperbolic heat conduction equation for materials with a nonhomogeneous inner structure, *J. Heat Transfer,* **112,** 555

8. Z.-B. Kuang and S.N. Atluri (1985), Temperature field due to a moving heat source: a moving mesh finite element analysis, *J. Appl. Mech.,* **52,** 274

9. J.J. Mason and A.J. Rosakis (1992), On the dependence of dynamic crack tip temperature fields in metals upon crack tip velocity and material parameters, SM Report 92-2, Graduate Aeronautics Laboratories, California Inst. of Tech., Pasadena, CA 91125

10. P.M. Morse and H. Feshbach (1953), *Methods of Theoretical Physics,* Vol. 1, McGraw-Hill Book Co., Inc., 837, 865

11. S. Nemat-Nasser (1992), *Private Communication*

12. A. Papoulis (1962), *The Fourier Integral and Its Applications,* McGraw Hill Book Co., Inc., New York

13. D.Y. Tzou (1989), On the thermal shock wave induced by a moving heat source, *J. Heat Transfer,* **111,** 232

14. D.Y. Tzou (1989), Shock wave formation around a moving heat source in a solid with finite speed of heat propagation, *Int. J. Heat Mass Transfer,* **32,** No. 10, 1979

15. D.Y. Tzou (1990), Thermal shock waves induced by a moving crack, *J. Heat Transfer,* **112,** 21

16. D.Y. Tzou (1990), Thermal shock waves induced by a moving crack—a heat flux formulation, *Int. Heat Mass Transfer,* **33,** No. 5, 877

17. R. Weichert and K. Schonert(1978), Temperature distribution produced by a moving heat source, *Q. J. Mech Appl. Math.,***31,** Pt. 3, 363

18. A.T. Zehnder and J.A. Kallivayalil (1991), Temperature rise due to dynamic crack growth in beta-c titanium, in *Speckle Techniques, Birefringence Methods and Applications to Solid Mechanics,* SPIE Vol. 1554A, 48

19. A.T. Zehnder and A.J. Rosakis (1991), On the temperature distribution at the vicinity of dynamically propagating cracks in 4340 steel, *J. Mech. Phys. Sol.,* **39,** No. 3., 385

CHAPTER 4

On the Strain and Strain-Rate Dependence of the Fraction of Plastic Work Converted to Heat: An Experimental Study Using High-Speed Infrared Detectors and the Kolsky Bar

Overview

The conversion of plastic work to heat at high strain-rates gives rise to a significant temperature increase which contributes to thermal softening in the constitutive response of many materials. This investigation systematically examines the rate of conversion of plastic work to heat in metals using a Kolsky (split Hopkinson) pressure bar and a high-speed infrared detector array. Several experiments are performed, and the work rate to heat rate conversion fraction, the relative rate at which plastic work is converted to heat, is reported for 4340 steel, 2024 aluminum and Ti-6Al-4V titanium alloys undergoing high strain and high strain-rate deformation. The functional dependence of this quantity upon strain and strain-rate is also reported for these metals. This quantity represents the strength of the coupling term between temperature and mechanical fields in thermomechanical problems involving plastic flow. The experimental measurement of this constitutive function is important since it is an integral part of the formulation of coupled thermomechanical field equations, and it plays an important role in failure mode selection—such as the formation of adiabatic shear bands—in metals deforming at high strain-rates.

4.1 Introduction

In coupled thermomechanical problems an additional field equation is added to the usual field equations. This additional equation, the heat conduction equation, provides a link between mechanical deformation fields and an additional unknown, the temperature field, $T(\mathbf{x}, t)$, and is given by

$$\alpha \nabla^2 T - \dot{T} = -\frac{\beta \boldsymbol{\sigma} \cdot \dot{\boldsymbol{\epsilon}}^p}{\rho c_p} + \frac{\kappa}{\rho c_p} \frac{E}{(1-2\nu)} T_0 tr(\dot{\boldsymbol{\epsilon}}^e) \tag{4.1}$$

where the dot refers to differentiation with respect to time, α is the thermal diffusivity, ρ is density, c_p is the heat capacity, β is defined below, $\boldsymbol{\sigma}$ is the stress, $\dot{\boldsymbol{\epsilon}}^p$ is the plastic strain-rate, κ is the coefficient of thermal expansion, E is Young's modulus, ν is Poisson's ratio, $\dot{\boldsymbol{\epsilon}}^e$ is the elastic strain-rate and T_0 is the initial or ambient temperature. The first term on the right represents heating due to irreversible plastic deformation (Taylor and Quinney, 1934; Bever et al., 1973) and second term represents heating due to the reversible thermoelastic effect (Sneddon and Berry, 1958). If elasticity is neglected and adiabatic conditions prevail, then the heat conduction equation takes a more simple form, i.e.;

$$\rho c_p \dot{T} = \beta \boldsymbol{\sigma} \cdot \dot{\boldsymbol{\epsilon}}^p = \beta \dot{W}^p \tag{4.2}$$

where

$$\beta = \frac{\rho c_p \dot{T}}{\dot{W}^p}. \tag{4.3}$$

Obviously, even for these simple conditions it is necessary to know the material parameters such as β, the work rate to heat rate conversion fraction, and c_p, the heat capacity which may depend upon temperature, before useful solutions to thermomechanics problems can be obtained.

Although c_p may be found in tables (sometimes as a function of temperature), β is not commonly available. Often β is simply assumed to be a constant in the range 0.85-1.00; a practice that dates back to the work of Taylor and Quinney (1934). They

determined β using calorimetric methods to measure the heat produced during quasi-static deformation. The remaining work is usually attributed to the stored strain energy, e.g., dislocations, defects and their interactions. However, it is known that β may depend upon strain. Many investigations (Bever et al., 1973) in the past that have been concerned with a quantity related to β, the fraction of stored energy defined as

$$f = 1 - \frac{\rho c_p T}{W^p}. \tag{4.4}$$

They have reported that this material property depends upon strain. Since β may be expressed in terms of f, it is clear that β will depend upon strain as well. At least two models have been proposed for predicting the dependence of β or f upon strain representing two mechanisms for the storage of energy in a material. In the first model, dislocation density is assumed to increase with strain at a rate that is proportional to the slope of the stress-strain curve. The energy per unit of dislocation density is estimated, and the relative rate at which work is converted to heat may then be related to the work hardening exponent (Bever et al. 1973; Zehnder, 1991). In the second model, the stored macroscopic strain energy is calculated for a polycrystalline solid made up of elastic perfectly plastic crystals, and the stored energy is related to the reciprocal of plastic work, $\int \epsilon^p d\sigma$ (Aravas et al., 1990). The two models produce different predictions for the dependence of β upon strain. For a power law hardening material,

$$\sigma = \begin{cases} \sigma_o \left(\frac{\epsilon}{\epsilon_o}\right) & \text{for } \sigma \leq \sigma_o \\ \sigma_o \left(\frac{\epsilon}{\epsilon_o}\right)^n & \text{for } \sigma \geq \sigma_o \end{cases}, \tag{4.5}$$

the two separate models predict

$$\beta(|\epsilon|) = \begin{cases} \dfrac{\left(\frac{\epsilon}{\epsilon_o}\right)^{1-n} - 2An}{\left(\frac{\epsilon}{\epsilon_o}\right)^{1-n} - n} & \text{for dislocation theory} \\ \dfrac{(1-n)\left(\frac{\epsilon}{\epsilon_o}\right)^n}{\left(\frac{\epsilon}{\epsilon_o}\right)^n - n\left(\frac{\epsilon}{\epsilon_o}\right)^{2n-1}} & \text{for strain energy theory.} \end{cases} \tag{4.6}$$

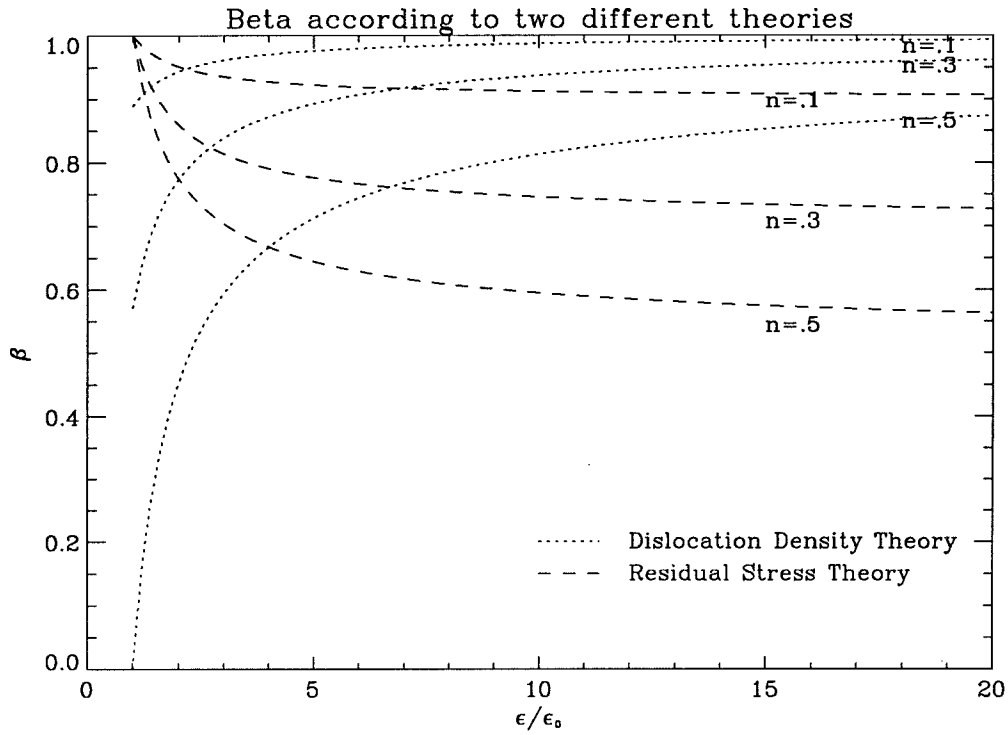

FIGURE 4.1 Theoretical prediction of the dependence of β, the work rate to heat rate conversion fraction, upon strain and hardening exponent, n, in metals. For the model of Zehnder $A = 1$.

where σ_0 and ϵ_0 are the yield stress and strain for the material, respectively, and n is the hardening exponent. The results may be seen in Fig 4.1 for different values of the hardening exponent, n. In the dislocation based model, β increases with strain while in the strain energy based model the opposite is true. (The models have been adapted to produce a prediction for β rather than f when necessary.) As evident from Eq (4.6), the dislocation theory contains an unknown parameter, A, that essentially assumes the role of a fitting parameter. The residual stress theory is exact for a material made up of elastic-perfectly-plastic crystals, but it only serves as a lower bound on β for work hardening crystals. Comparison of these models with experiments on copper at low strain-rates (Williams, 1965) showed the model of Zehnder (1991) to be more accurate for that material.

Little is known about the dependence of β upon strain-rate. Some early work

has shown that the stored energy in drawn wires has a maximum when plotted with respect to drawing rate (Bever et al., 1973). This maximum is attributed to the thermal annihilation of dislocations at higher drawing rates resulting in a decrease in stored energy. Also, if one uses the above theories for strain dependence of β should be used for all strain-rates, then the materials exhibiting strain-rate dependence in their mechanical behavior should also exhibit strain-rate dependence in β. For example, copper is weakly strain-rate dependent for strain-rates in the range 10^{-4}–10^{3}, and, consequently, it has shown a very small strain-rate dependence in the work rate to heat rate conversion fraction, β (Williams, 1965). Even though the work rate to heat rate conversion fraction, β, shows some indication of being a material dependent function of both strain and strain-rate, i.e., $\beta = \beta(|\epsilon|, |\dot{\epsilon}|)$, virtually no work has systematically tried to investigate the dependence of β upon strain-rate for many structural materials. The experimental procedure introduced here for the first time provides a simple means by which to carry out such investigations.

It is important to investigate the behavior of β under a variety of deformation histories because of its role in thermomechanics. In dynamic plasticity experiments the conversion of plastic work to heat can lead to thermal softening and instabilities in the deformation (for example see Clifton et al., 1984 and Batra and Wright, 1988). Any numerical modelling of dynamic plastic deformation that includes the effects of heat generation would require complete knowledge of the behavior of the material constitutive functions, including β, during all phases of deformation before accurate modeling of any unstable behavior such as adiabatic shear band formation (Duffy, 1984; Giovanola, 1988) may be achieved. Motivated by the above concerns our goal here is to report on the initial steps of a study whose aim is to investigate the functional dependence of β on $|\epsilon|$ and $|\dot{\epsilon}|$ for a variety of loading regimes.

4.2 Experimental Apparatus

The Kolsky pressure bar is used to deform the materials at high strain-rates ($\approx$1000–3000 s^{-1}) in this investigation. The incident, $\epsilon_I(t)$, reflected, $\epsilon_r(t)$, and transmitted, $\epsilon_T(t)$, strain signals are recorded by strain gauges attached to the input and output bars. The stress, strain-rate, strain and average velocity of the deforming specimen can be determined from the recorded incident, reflected and transmitted pulses assuming that the specimen deforms *homogeneously*; (Kolsky, 1949)

$$\begin{aligned} \sigma(t) &= E_{bar}\frac{A_o}{A}\epsilon_T(t) \\ \dot{\epsilon}(t) &= -\frac{2c_o}{L}\epsilon_R(t) \\ \epsilon(t) &= \int_o^t \dot{\epsilon}(\tau)d\tau \\ \bar{v}(t) &= \frac{2c_o}{L}\epsilon_I(t) \end{aligned} \tag{4.7}$$

where E_{bar} is Young's modulus of the bar, A_0 and A are the cross-sectional area of the bar and the specimen, respectively, c_0 is the one-dimensional wave speed in the bar, L is the specimen length and $\bar{v}$ is the average specimen velocity. Note that the average velocity is non-zero, meaning that the specimen translates past a stationary observer. For further details of the pressure bar technique the reader is referred to Lindholm (1965) and Follansbee (1985).

In order to record the temperature rise in the Kolsky pressure bar experiments a stationary, focused, high-speed, infrared detector array is used. For details regarding the detector array time response and characteristics see Zehnder and Rosakis (1991 and 1993). The array is shown in Figure 4.2. The detectors are calibrated by heating a sample—with controlled surface finish—of the specimen material to a known temperature while simultaneously recording the detector output voltage. The calibration procedure precludes the need for any knowledge of the specimen emissivity and, thus, greatly simplifies the temperature measurement procedure. A sample calibration curve

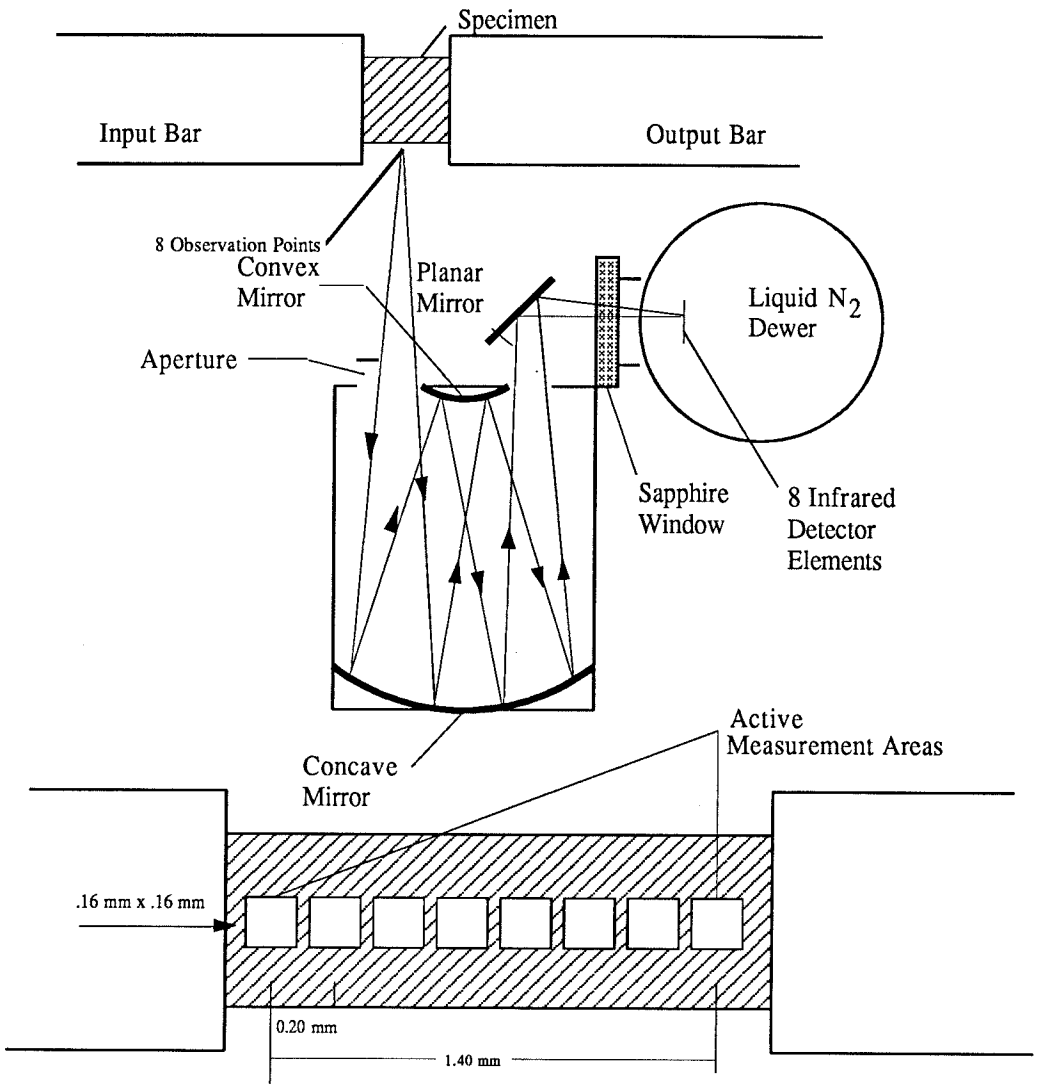

(Specimen, bars and detector array not drawn to scale.)

FIGURE 4.2 A schematic representation of the high-speed I-R detector array focussed on a specimen in a Kolsky pressure bar. The detector array size and orientation as focussed on the specimen is also shown.

corresponding to a 4340 specimen may be seen in Figure 4.3. Although they are not shown, calibration curves are evaluated for every material investigated here. In each case the resulting curve is qualitatively very similar to Figure 4.3. The dependence of the calibration curve upon surface finish is investigated since the specimen surface finish may change during deformation in the Kolsky bar. Two roughnesses were chosen; one representing the specimen before deformation, 600 grit finish, and one representing the specimen after deformation, 120 grit finish. Minimal dependence upon surface finish is seen. For the two very different surface finishes the calibration is very nearly the same and within the scatter of either calibration curve. This is largely due to the longer wavelength of infrared radiation and the detector characteristics. (The detectors integrate energy over a band of infrared wavelengths.) Some materials exhibit a stronger dependence upon surface finish than others; colored metals such as brass and copper are somewhat more sensitive to finish. Regardless, it suffices to say that for the metals studied here, the effects of change in surface finish during deformation are negligible. Further details of the high-speed infrared measurement technique can be found in Duffy (1984) and in Zehnder and Rosakis (1991 and 1993).

Assuming that homogeneous deformation of the specimen occurs, one may easily calculate the plastic work rate density from the Kolsky bar using relations (4.7) and

$$\dot{W}^p = \boldsymbol{\sigma} \cdot \dot{\boldsymbol{\epsilon}}^p. \tag{4.8}$$

By measuring the temperature and differentiating it with respect to time, $\dot{T}(t)$ is estimated, and by assuming that adiabatic conditions apply during the experiment, β is calculated from Eq (4.3). The density and heat capacity (with its dependence upon temperature) may be found in the literature (e.g., Aerospace Structural Materials Handbook, 1985) for the materials investigated; 4340 steel, Ti-6Al-4V and 2024 Al. Fortunately, it is seen that the heat capacity for each of these materials does not change significantly over the range of material temperatures anticipated during the experiments (20-130°C).

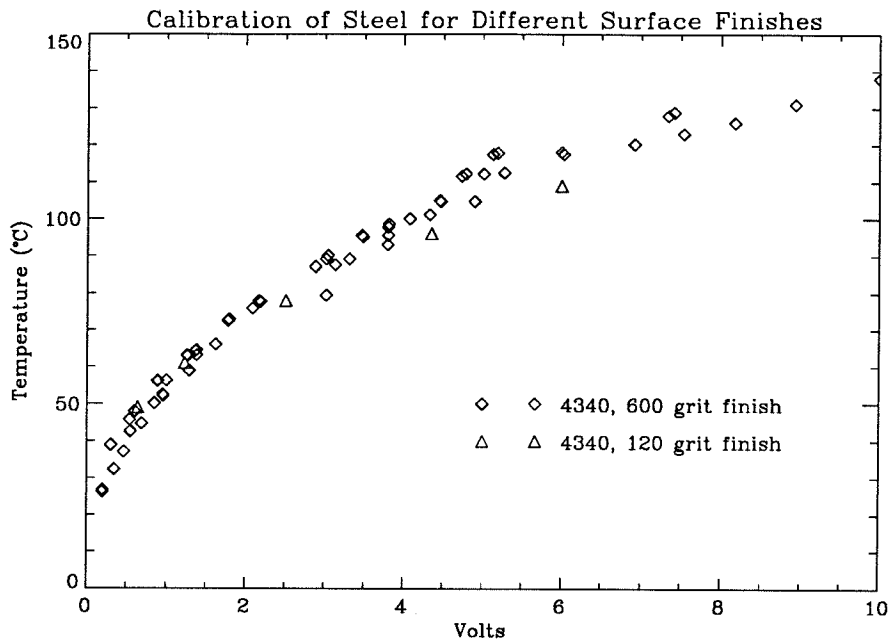

FIGURE 4.3 Calibration of the I-R detectors. The dependence of the calibration curve upon surface finish is shown to be minimal.

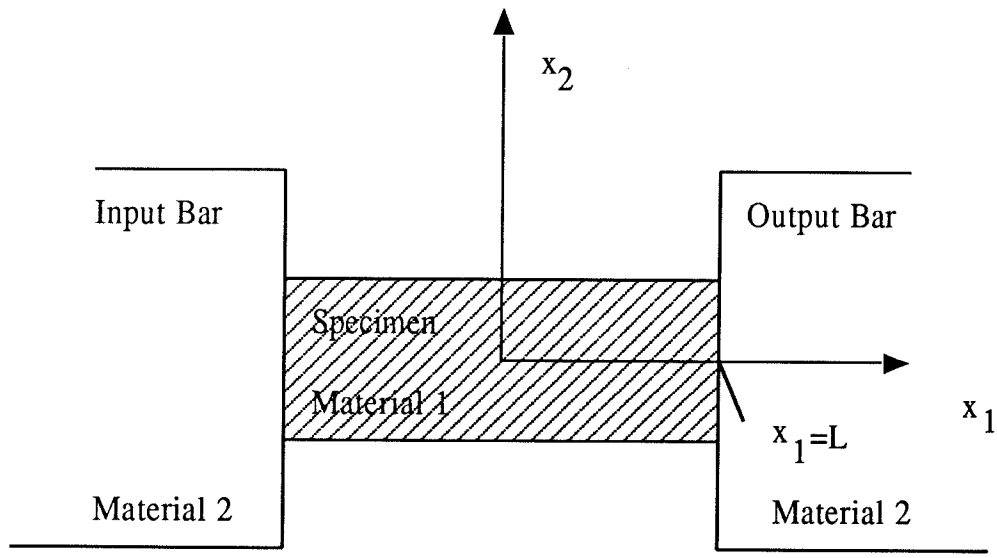

FIGURE 4.4 A schematic representation of the Kolsky Bar for purposes of model the conduction of heat during a typical high strain-rate test.

4.3 Theoretical Model of Heat Conduction in the Kolsky Bar

In order to be sure that adiabatic conditions prevail throughout the dynamic testing of materials, a model of heat conduction in the Kolsky bar is proposed. The geometry for the heat conduction problem in a Split Hopkinson Pressure Bar is shown in Fig 4.4. The configuration is symmetric about $x = 0$, the axial centerline of the specimen. Material 1 represents the specimen (of total length $2L$); material 2 represents the semi-infinite input or output bar. It is assumed that at $x = L$ the specimen and the bars mate perfectly allowing conduction across the interface without heat loss. The boundary conditions of the problem as stated are as follows:

$$\frac{\partial T_1}{\partial x} = 0, \qquad for\ x = 0$$

$$k_1 A_1 \frac{\partial T_1}{\partial x} = k_2 A_2 \frac{\partial T_2}{\partial x}, \qquad for\ x = L$$

$$T_1 = T_2, \qquad for\ x = L$$

$$T_2 = 0, \qquad for\ x \to \infty.$$

The most dubious of these conditions is the second one. This simply states that the energy flow into the interface equals the energy flow out of the interface, however the energy flow is related to the cross-sectional area of the materials. Implicit in this assumption is the assumption that energy flows into or out of the larger cross section uniformly throughout that cross section. Clearly this is impossible since the contact occurs only over an area equal to the smaller cross section. It is not sufficient to let the two areas be equal because heat flow into or out of the larger cross section will not be one-dimensional, and, in general, three-dimensional effects will lead to more heat flow than predicted by the one-dimensional approximation. Therefore, in order to produce a conservative estimate of the requirements for adiabatic conditions, the above assumption is made. Note also, that the length, L, will change in the Kolsky bar during a test and that no provision for that effect is made here; L is assumed to be fixed. Lastly, note that the area of the specimen, A_1, will change during the deformation and

that no provision is made for that effect either. Later, the qualitative effects of all these oversimplifying assumptions will be assessed.

Since there exists a characteristic length scale, L, for this problem it is possible to non-dimensionalize the governing equation, Eq (4.1), by assuming a characteristic temperature, T_0,

$$\frac{\partial^2\theta}{\partial X^2} - \frac{\partial\theta}{\partial\tau} = -G \tag{4.9}$$

where

$$\begin{aligned}
\theta &= \frac{T}{T_0} \\
\tau &= \frac{\alpha t}{L^2} = \frac{t}{\tau_0} \\
\tau_0 &= \frac{L^2}{\alpha} \\
X &= \frac{x}{L} \\
G &= \frac{gL^2}{kT_0}
\end{aligned} \quad .$$

For the problem at hand Ozisik (1980) has provided a usable solution. Assuming a homogeneous governing equation, $G = 0$, and the initial conditions

$$\theta^*(X,0) = H(X) - H(X-1) \tag{4.10}$$

where $H(X)$ is the Heaviside function, Ozisik (1980) finds a solution given by

$$\begin{aligned}
\theta_1^* =& 1 - \\
& \frac{1-\gamma}{2}\sum_{n=0}^{\infty}\gamma^n\left\{\operatorname{erfc}\left[\frac{2n+1-X}{2\sqrt{\tau}}\right] + \operatorname{erfc}\left[\frac{2n+1+X}{2\sqrt{\tau}}\right]\right\}, \quad for\ 0 < X < 1 \\
\theta_2^* =& \frac{1+\gamma}{2} \\
& \sum_{n=0}^{\infty}\gamma^n\left\{\operatorname{erfc}\left[\frac{2n+\mu(X-1)}{2\sqrt{\tau}}\right] - \operatorname{erfc}\left[\frac{2n+2+\mu(X-1)}{2\sqrt{\tau}}\right]\right\}, \quad for\ X > 1
\end{aligned} \tag{4.11a}$$

where

$$\begin{aligned}
\gamma &= \frac{k_1A_1 - k_2A_2\mu}{k_1A_1 + k_2A_2\mu} \\
\mu &= \sqrt{\frac{\alpha_1}{\alpha_2}}
\end{aligned} \quad . \tag{4.11b}$$

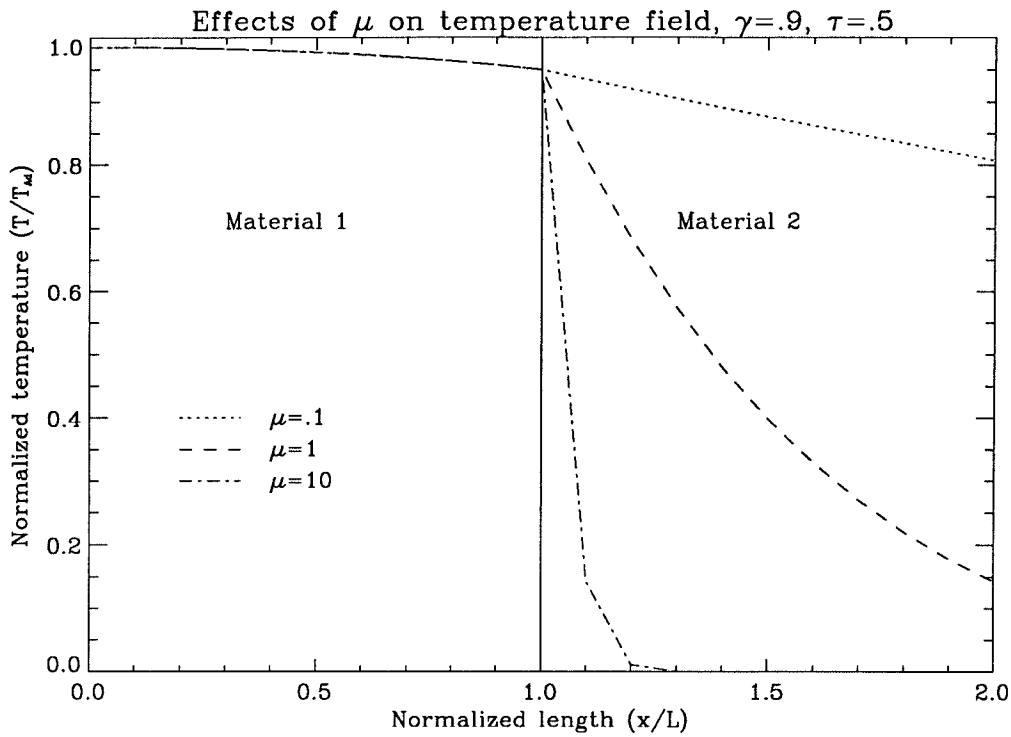

FIGURE 4.5 The effect of the parameter μ is demonstrated for $\gamma = .9$ and $\tau = .5$. It is seen that increasing μ decreases the temperature in material 2 while not effecting the temperature in material 1. Physically, an increase in μ means that the penetration depth in material 2 is much smaller than that in material 1.

Note in this solution that μ only effects the temperature in material 2 i.e., θ_1^* does not depend upon μ. Since we are most interested in the temperature in material 1, the effects of μ are not investigated in depth here. Figure 4.5 shows that the temperature in material 2 decreases with increasing μ. This is to be expected since a large μ indicates a smaller penetration depth in material 2 than in material 1. Also note that there are a few values of γ which have physical significance:

- when $\gamma = 0$ This occurs when materials 1 & 2 and their cross sections, A_1 and A_2, are equal, i.e., $\gamma = 0$ and $\mu = 0$. Then the problem reduces to a uniform semi-infinite bar. If the materials are not the same, the temperature in material 1 is that for a uniform bar; only the temperature in material 2 changes.

when $\gamma = 1$ Conduction in material 1 is dominant, and material 2 acts as an insulator. At the interface $\frac{\partial \theta_1}{\partial X} = 0$ at $X = 1$.

when $\gamma = -1$ Conduction in material 2 dominates, and material 2 acts as a heat sink. A fixed temperature condition exists at the interface, $\theta_1 = 0$ at $X = 1$.

This solution may be used as a "quasi-Green's function." Following the example of Duff and Naylor (1966). Ozisik's (1980) solution may be multiplied by the Heaviside function. Then the problem is re-cast for a non-homogeneous governing equation, and no initial conditions are needed. Letting

$$\begin{aligned} \theta_1^g(X,\tau) &= \theta_1^*(X,\tau)H(\tau) \\ \theta_2^g(X,\tau) &= \theta_2^*(X,\tau)H(\tau) \end{aligned} \tag{4.12}$$

and inserting this solution into Eq (4.9) yields

$$\frac{\partial^2 \theta_{1,2}^g}{\partial X^2} - \frac{\partial \theta_{1,2}^g}{\partial \tau} = -\delta(\tau)\left[H(X) - H(X-1)\right],$$

where the solution, θ^g, is now defined for $\tau \in (-\infty, \infty)$ rather than for $\tau \in [0, \infty)$ as is θ^*. If it is assumed that the plastic work in the specimen is uniform, i.e., it always has the dependence upon X given in Eq (4.10) and that elastic effects are negligible, then we can integrate the solution in Eq (4.12) to get the temperature distribution for a time varying heat source density. Mathematically, it is assumed that

$$G(X,\tau) = \hat{g}(\tau)\theta_{1,2}^*(X,0) \tag{4.13}$$

then

$$\begin{aligned} \theta_1(X,\tau) &= \int_{-\infty}^{\infty} \hat{g}(s)\theta_1^g(X,\tau-s)ds \\ \theta_2(X,\tau) &= \int_{-\infty}^{\infty} \hat{g}(s)\theta_2^g(X,\tau-s)ds \end{aligned}$$

which can be verified by direct substitution into Eq (4.9). Substituting Eq (4.12) in the above equation yields

$$\begin{aligned} \theta_1 &= \int_{-\infty}^{\tau} \hat{g}(s)\theta_1^*(X,\tau-s)ds \\ \theta_2 &= \int_{-\infty}^{\tau} \hat{g}(s)\theta_2^*(X,\tau-s)ds. \end{aligned} \tag{4.14}$$

For uniaxial compression it may be assumed that

$$\hat{g}(\tau) = \beta\sigma\dot{\epsilon}\frac{L^2}{kT_0}H(\tau) \tag{4.15}$$

and that $\beta\sigma\dot{\epsilon}$ is constant. The latter assumption is exact for a perfectly plastic material with constant converted work fraction, β, deforming under uniform constant strain-rate. Although the actual deformation is much more complicated than that, it is observed experimentally that the assumption of constant $\beta\sigma\dot{\epsilon}$ is, in fact, quite reasonable. Unloading is not considered, i.e.,

$$\hat{g}(\tau) = \beta\sigma\dot{\epsilon}\frac{L^2}{kT_0}\left[H(\tau) - H(\tau - \tau_1)\right]$$

since in this investigation it is only important to establish the existence of adiabatic conditions *during* the test. After unloading occurs, it is of no consequence whether adiabatic conditions remain.

The ratio of the predicted temperature in Eq (4.14) to the magnitude of the adiabatic temperature may be found using Eq (4.15), i.e.,

$$\begin{aligned}\frac{\theta_1}{|\theta_{ad}|} &= \frac{1}{\tau}\int_0^\tau \theta_1^*(X, \tau - s)ds, \\ \frac{\theta_2}{|\theta_{ad}|} &= \frac{1}{\tau}\int_0^\tau \theta_2^*(X, \tau - s)ds.\end{aligned} \tag{4.16}$$

Note that solution in Eq (4.16) is independent of the strain-rate, $\dot{\epsilon}$. This is because $\beta\sigma\dot{\epsilon}$ has been assumed to be constant, and normalizing by the adiabatic temperature removes it from the solution expression. As a result, only the time length of the test, τ, and the conditions at the interface, γ, determine whether adiabatic conditions prevail.

The results of the numerical integration of the solution given in equation (4.16) are shown in figures 4.6(a)-(e). It can be seen in the figures that the time below which adiabatic conditions prevail, τ_0, is independent of the boundary conditions, γ. This fact indicates that adiabatic conditions hold for a specified time regardless of the input and output bars. Only the specimen material paramenters are important. The characteristic times below which adiabatic conditions prevail are listed in Table 4.1.

Table 4.1

Material Parameters and Characteristic Times for Several Materials

Material	α (10^{-6} m^2/s)	k ($W/m°C$)	τ_0 (s)	t_{ad} (μs)	γ	μ
Steel	9.86	34.6	.575	5750	-.88	1
Ti-6-4	4.78	10.9	1.19	11,900	-.95	.7
Pure Cu	112.6	386	.050	500	-.18	3.4
Brass	34.12	111	.166	1660	-.80	1.9
Al-2024	66.76	164	.085	850	-.79	2.7
Glass	0.343	0.78	16.5	165,000	-.98	.27

where γ has been calculated assuming a 3/16" diameter specimen and a 3/4" bar.

Note that $\gamma \approx -1$ for most materials except for copper, thus a fixed temperature boundary condition will suffice in future analyses. For most high strain-rate tests, $\dot{\epsilon} \approx 10^3$, the time length of the test is on the order of 10 μs. Thus, adiabatic conditions prevail in those tests. For lower strain-rate tests the time length of the test must be determined before it is possible to asses the validity of adiabatic assumptions.

Since the dimensions are normalized with respect to the specimen size, L, it is expected that changes in this parameter will have only a minor effect on the solution, possibly causing the temperatures in the specimen to be lower than expected when $X = 1$ and for τ large. As the cross-sectional area of the specimen increases, so does γ. However, in determining the conditions under which the adiabatic assumption is valid it has been shown the γ has little effect. Thus, the effect of a changing specimen cross section is minimal. Remember, the boundary conditions assumed are very conservative, so the prediction of this model concerning the validity of adiabatic assumptions is a conservative prediction. The effects of a non-constant L and a non-constant A_1 are considered less than significant because of the conservative approach.

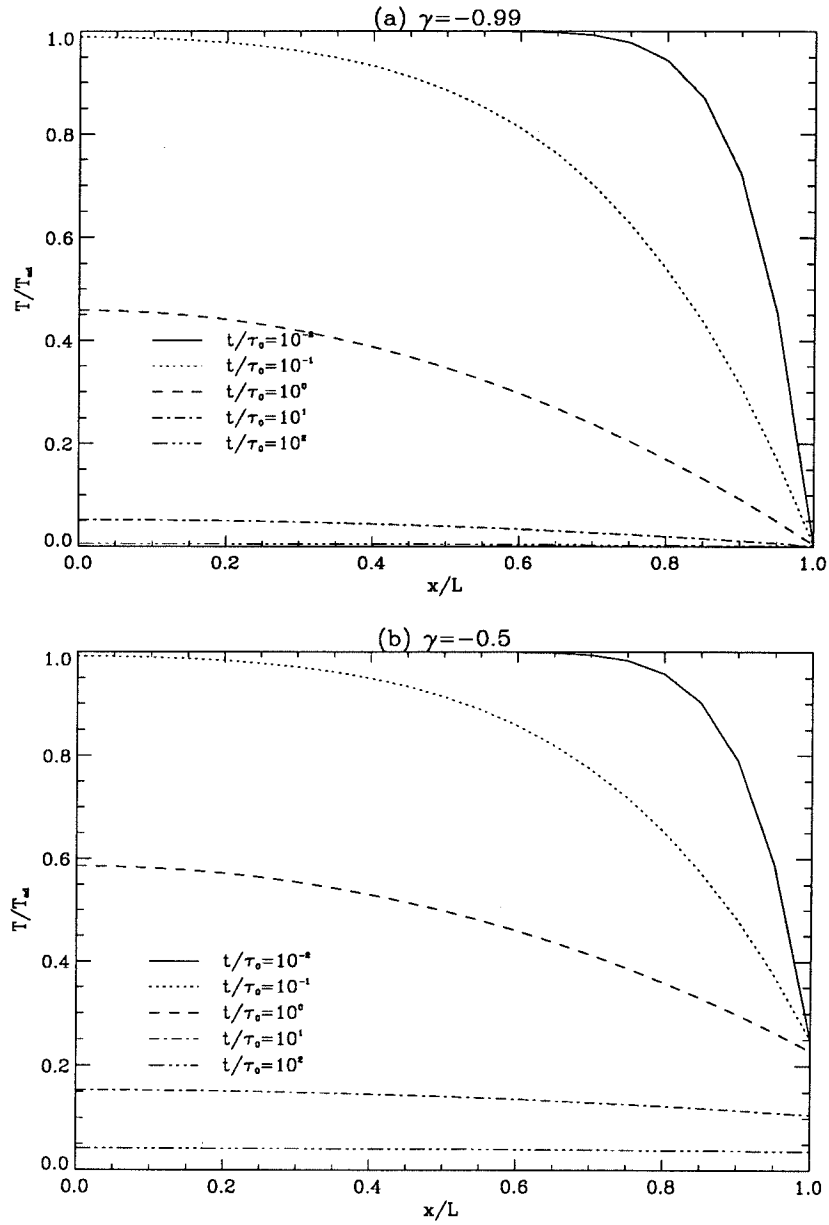

FIGURE 4.6 (a)The temperature field in material 1 is plotted for various times when $\gamma \to -1$. In this case it is expected that a constant temperature, $\theta = 0$, is held at the interface. It can be seen that this boundary condition holds. For $\tau < 10^{-2}$ adiabatic conditions prevail over most of the specimen, $X < .7$. (b)The temperature field in material 1 for $\gamma = -.5$. For short times the boundary condition at $X = L$ is given by $(\gamma + 1)/2$ and using asymptotic analysis. For long times the temperature in the specimen is independent of postion and the temperature decays as $1/\sqrt{\tau}$ (as expected from asymptotic analysis). For $\tau < 10^{-2}$ adiabatic conditions prevail over most of material 1.

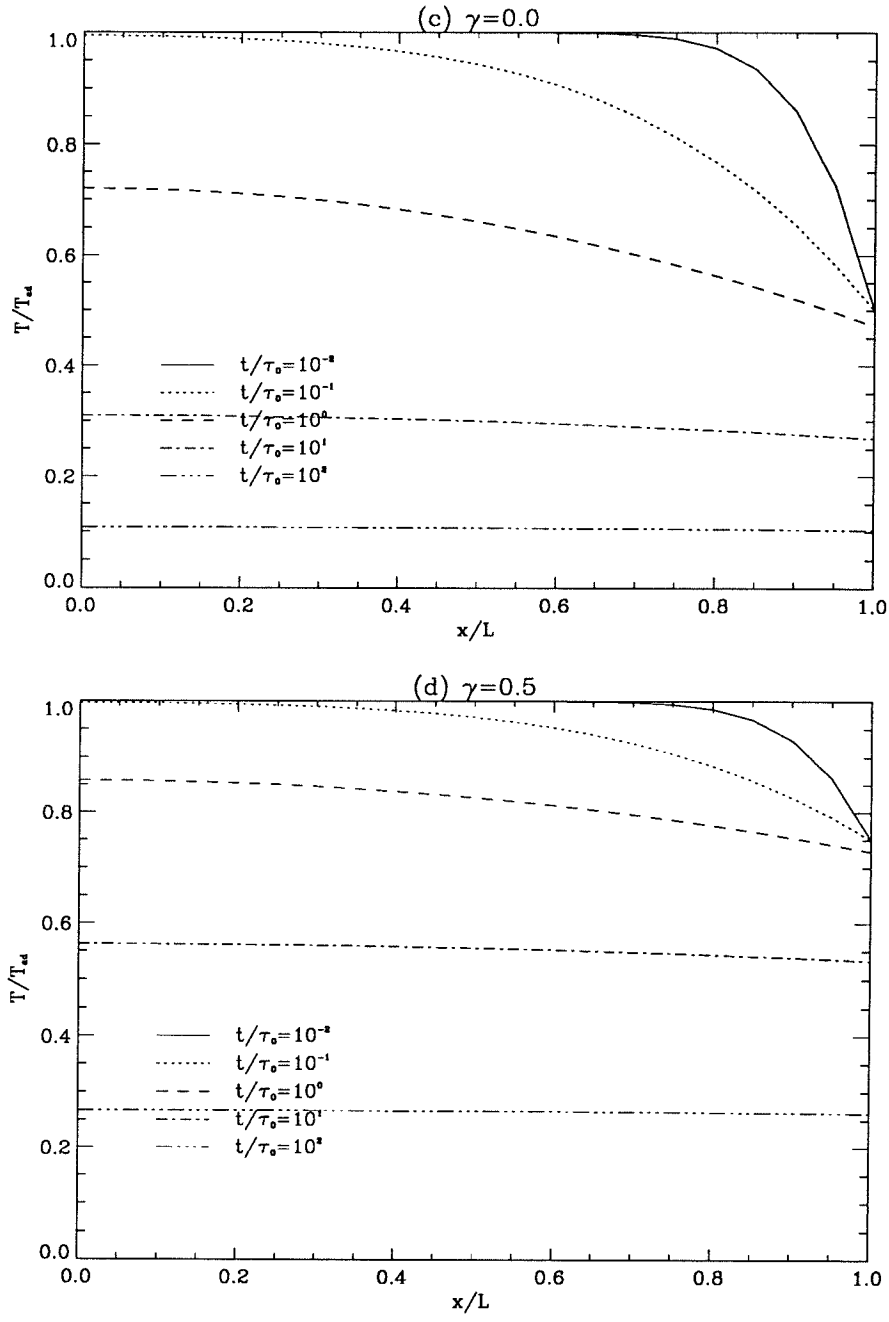

FIGURE 4.6 (c)The temperature field in material 1 for $\gamma = 0$. (d)The temperature field in material 1 for $\gamma = .5$. For $\tau < 10^{-2}$ adiabatic conditions prevail over most of material 1 for both boundary conditions.

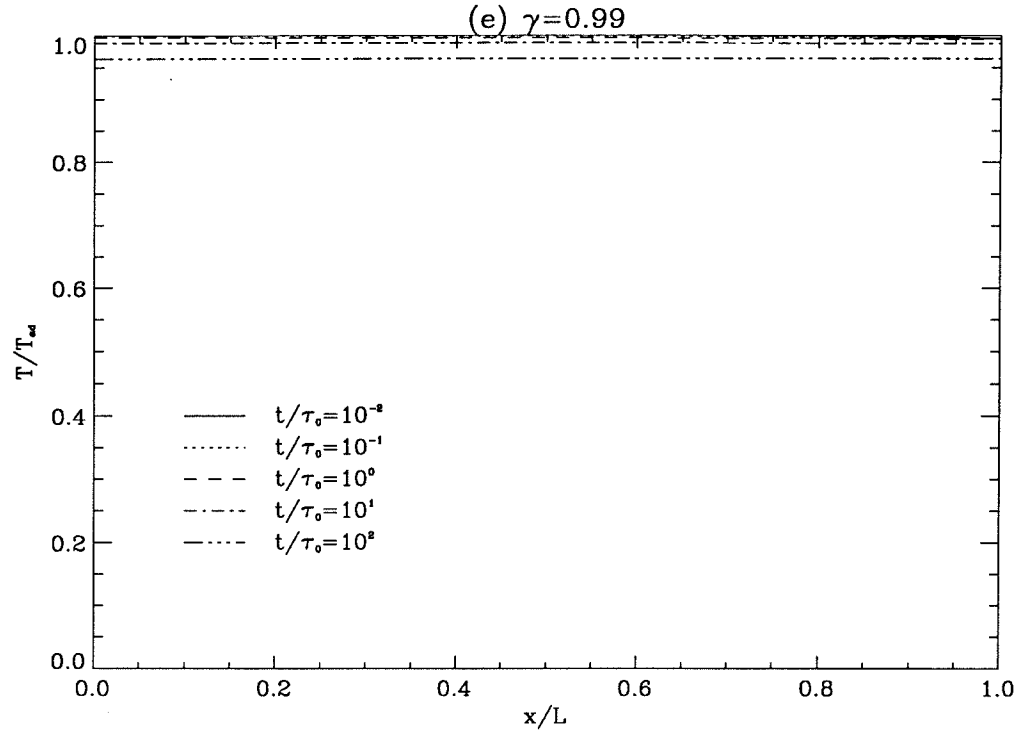

FIGURE 4.6 (e)The temperature field in material 1 for $\gamma = .99$. As expected when $\gamma \rightarrow 1$, adiabatic conditions prevail for long times. For $\tau < 10^0$ adiabatic conditions prevail rather than for $\tau < 10^{-2}$ as in all the previous cases.

4.4 Results and Discussion

Typical results of the experiments are shown for 2024 aluminum in Figure 4.7. The figure shows the time history of strain of the input and output bars as well as the time history of the voltage output of two detectors focussed on the specimen surface at two points 1.4 mm apart. It should be noted that the temperature reaches its maximum value within 150 μs of the beginning of loading at approximately 200 μs and remains constant once unloading occurs, thus the process is *adiabatic*. Adiabatic conditions were observed for all materials studied here. Also, the two detector output voltages nearly coincide during loading of the specimen. Since the process is adiabatic, Eq (4.2) holds, and, since the temperature is nearly independent of position, Eq (4.2) indicates that the plastic work rate is also nearly independent of position. Thus, the deformation is homogeneous. It is also worth observing that there is a second temperature rise in the

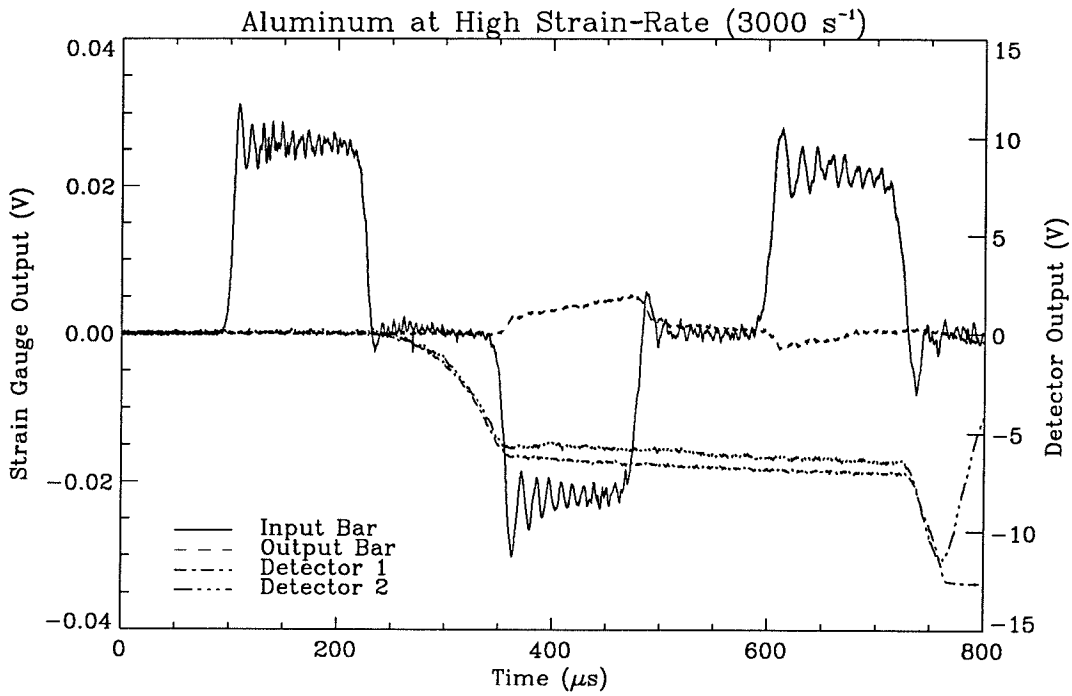

FIGURE 4.7 The results of a typical Kolsky bar experiment on 2024 aluminum. The transmitted and reflected signals are delayed with respect to the temperature signal because the strain gauge measurements are made at a finite distance from the specimen.

specimen due to the reflection of waves from the free end of the input bar which result in a second loading of the specimen. In softer materials such as 2024 aluminum this secondary temperature rise is significant. Lastly, it is observed that the output of one of the detectors drops shortly after the second loading of the specimen by the reflected wave begins. This is because the specimen and input bar are moving. The input bar has moved in front of one detector causing a lower temperature to be measured there.

The stress-strain curve for 2024 Aluminum calculated from the Kolsky bar equations is shown in Figure 4.8. Note that three-dimensional effects and lack of equilibrium in the specimen at short times in the Kolsky bar result in inaccuracies at low strains (Follansbee and Frantz, 1983) and that the elastic behavior of the specimen is not captured. These effects add to the uncertainty in the calculation of β at low strains

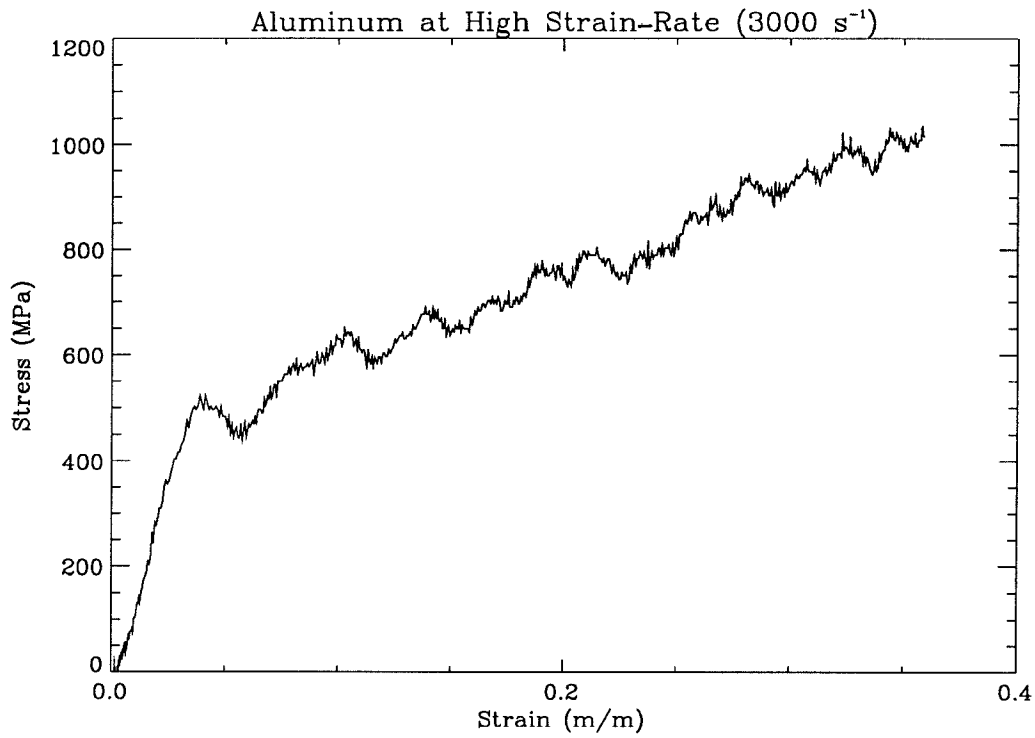

FIGURE 4.8 The stress-strain relationship for 2024 aluminum at high strain-rate (3000 s^{-1}). The hardening exponent from a fit of the power law constitutive equation, Eq. (4.5), is calculated to be .31.

($\epsilon \leq 3\%$). The hardening exponent for 2024 Al is 0.31 when the constitutive model in Eq (4.5) is fitted to the experimental results. The plastic work rate may be calculated using equations (4.7) and (4.8) and is shown in Figure 4.9. An approximation of the plastic work by a linear fit of the experimental data with respect to time is also shown in the figure. This approximation is considered a valid estimate of the true plastic work rate since the oscillations in the experimentally observed plastic work rate are due to three-dimensional wave propagation in the input and output bars of the apparatus. In the calculations of β presented here the fitted approximation is used.

The temperature measurement also suffers from inaccuracies at low temperatures because of inherent noise in the signal and the slope of the calibration curve. At low voltages the calibration curve slope becomes very large, therefore a small amount in noise can result in large fluctuation in temperature. This makes the calculation of β

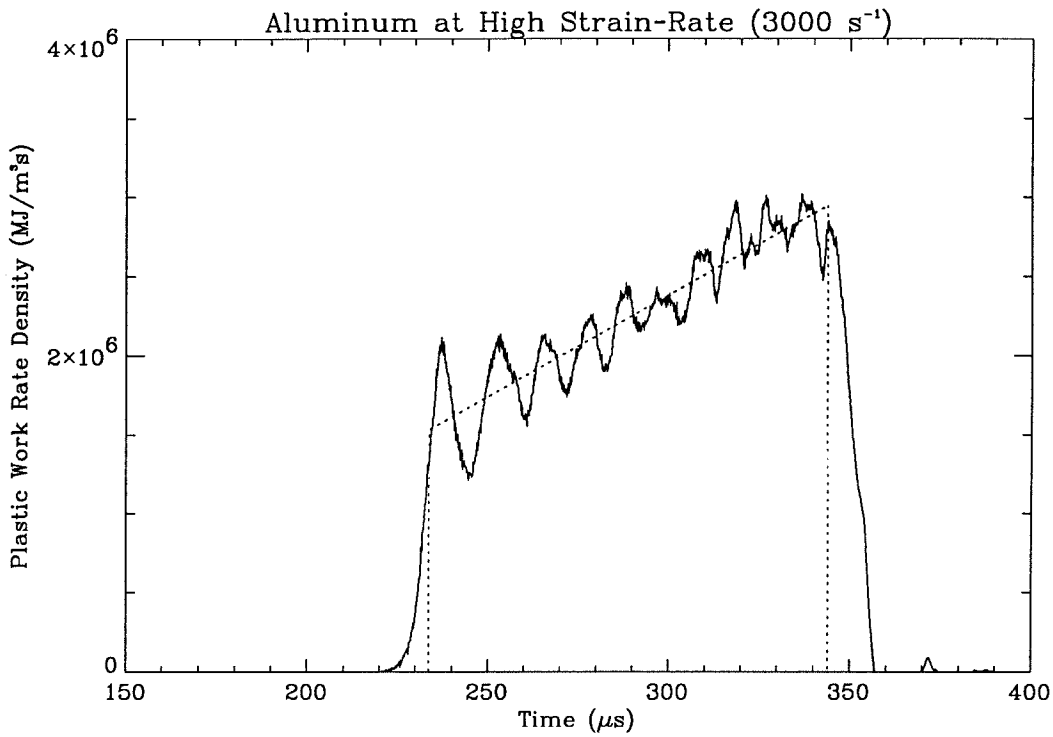

FIGURE 4.9 The plastic work rate density as calculated using Eqs. (4.7) and (4.8). The oscillations are due to three-dimensional wave propagation in the bar. A linear fit to the data shown as a dotted line is used in calculations of β.

uncertain for low strains ($\epsilon \leq 3\%$) where temperature rise is still small (below 10°C).

The most significant difficulty in calculating β however is due to the problems associated with differentiation of the measured temperature. Differentiation of a noisy signal has inherent instabilities, and usual numerical differentiation schemes such as the central difference method (Beyer, 1987) do not work because they are formulated for numerically exact functions. The noise in the function to be differentiated by such methods must be much smaller than the sampling time. That is not the case here, and an alternate method is necessary to accurately differentiate the temperature rise. It is not sufficient to simply fit a known function to the temperature measurement in this case because the exact form of the expected result is not known and two equally good fits can result in dramatically different derivatives. Consequently, the method of Vasin (1973) and Groetsch (1992) is used to differentiate the temperature measurement. In

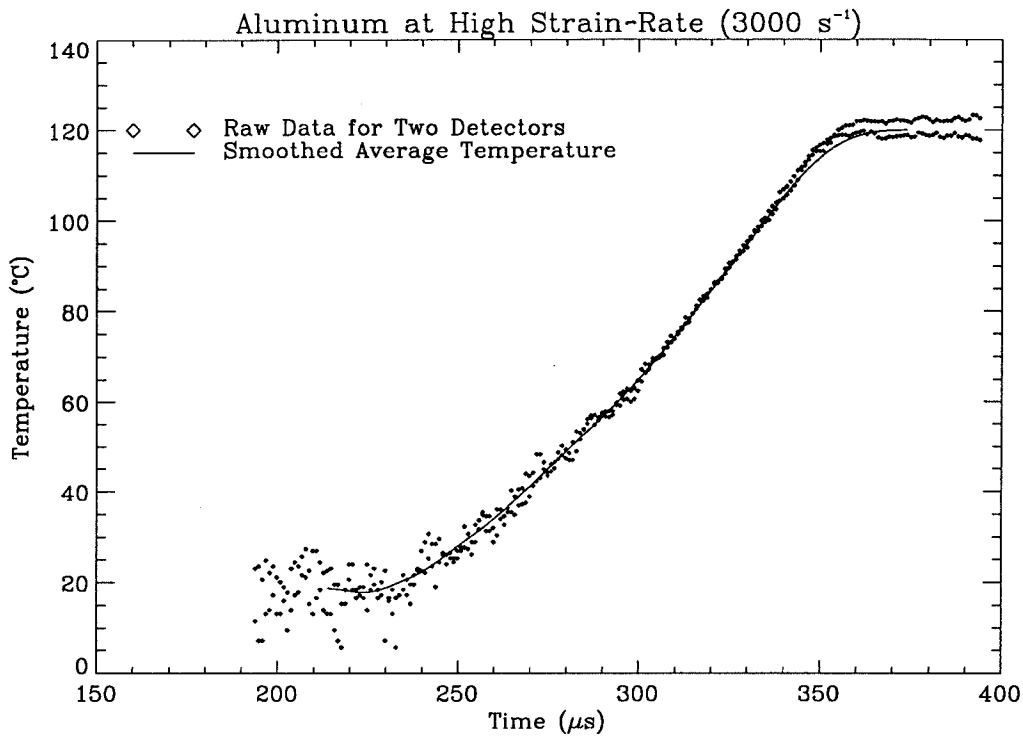

FIGURE 4.10 The temperature data for 2024 aluminum. The solid line represents the smoothed function which is differentiated using the method of Vasin, (1973), and Groetsch, (1992).

this method a weighted average smoothing function is used to differentiate a noisy signal, $g(t)$, i.e.,

$$\omega_{t_0}(t) = \begin{cases} \frac{.825}{t_0} exp\left[t^2/(t^2 - t_0^2)\right], & \text{for } |t| < t_0 \\ 0, & \text{for } |t| \geq t_0 \end{cases} \tag{4.17}$$

where

$$\begin{aligned} g_s(t) &= \int_{t-t_0}^{t+t_0} \omega_{t_0}(t-s)g(s)ds \\ &= \omega_{t_0} * g, \end{aligned} \tag{4.18}$$

where t_0 is the half width of the time over which a weighted average of the noisy signal is taken and $g_s(t)$ is the smoothed function. An example of the smoothed temperature signal with $t_0 = 20\mu s$ may be seen in Figure 4.10 plotted with both noisy signals. Further precautions were taken by averaging the two temperature signals before smoothing to reduce some of the noise at low temperature. Differentiation of the noisy

signal, $g(t)$, is carried out by using the relationship

$$g'_s(t) = \omega'_{t_0} * g \quad (= \omega_{t_0} * g'). \tag{4.19}$$

Consequently, the derivative is actually found by differentiating the smoothing function, $\omega_{t_0}(t)$, and integrating the convolution in Eq (4.19) for all points of the temperature signal. Multiplying the derivative of temperature by ρc_p and using equation (4.3) results in the evaluation of β.

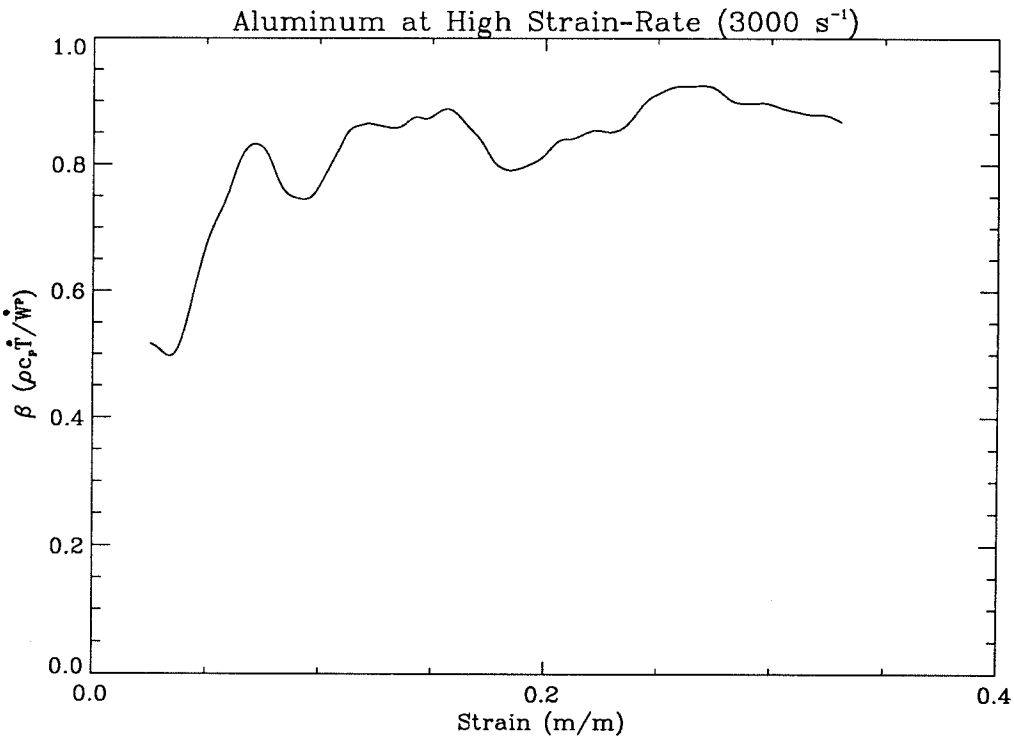

FIGURE 4.11 The work rate to heat rate conversion fraction for 2024 aluminum. Good qualitative agreement is seen between the experimental results shown here an the theoretical prediction of Zehnder in Figure 4.1.

The dependence of the work rate to heat rate conversion fraction, β, upon strain for a nominal strain-rate of 3000 s^{-1} and corresponding to the raw data shown in Figures 4.7-4.10 is plotted in Figure 4.11. It can be seen that β for 2024 aluminum is strongly strain dependent; initially the relative rate at which work is converted to heat is approximately 0.5 rising with strain to the traditionally accepted 0.85-1.00 range for

metals (Taylor and Quinney, 1934; Bever et al., 1973). The trend qualitatively follows the model of Zehnder (1991) and not that of Aravas et al. (1990). Since the model of Zehnder is known to be more accurate than the model of Aravas et al. for strain-rate insensitive copper at low strain-rates and nominally high strain-rates ($10^3 s^{-1}$) and since quasi-static testing of the 2024 aluminum by the authors shows that the stress-strain curve has only a weak strain-rate dependence over the same strain-rate range, it is concluded that β for 2024 aluminum at high strain-rates behaves much the same as it would be expected to behave at low strain-rates. This is also supported by the finding that the large strain value calculated for β at high strain-rates, 0.85, corresponds well with general observations of β made for all metals at low strain-rates. Thus, strain-rate dependence in β is not found in 2024 aluminum for strain-rates up to $\dot{\epsilon} \approx 3000 s^{-1}$.

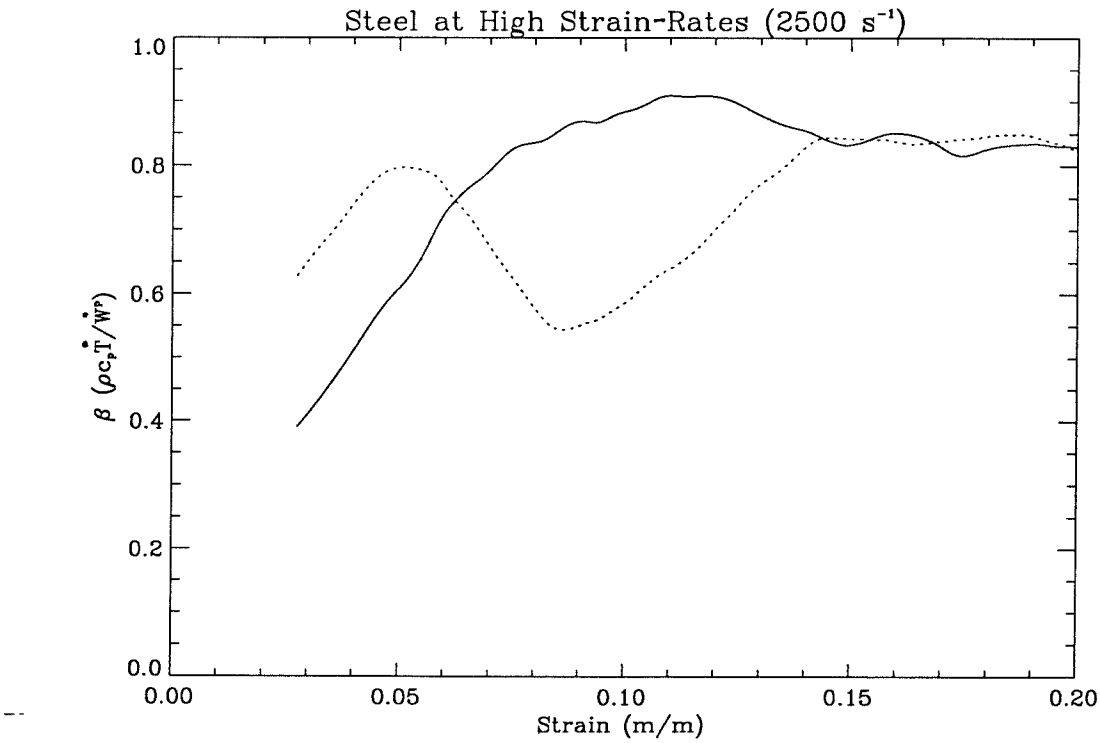

FIGURE 4.12 The work rate to heat rate conversion fraction for steel. The calculation of β has been carried out for each detector individually. The anomalous result in one detector at lower strains is due to inhomogeneous deformation of the steel.

In Figure 4.12 the same calculation has been carried out for 4340 steel. Here the signals from each detector was treated individually to show some unexpected behavior. It can be seen that for one detector in early parts of the experiment the value of β varies noticeably. However, on the other detector the value of β is a smoothly increasing function of strain and in qualitative agreement with the results for 2024 aluminum. The final value of β for both detectors , 0.85, is in agreement with earlier preliminary experiments on 4340 steel (Rosakis et al., 1992). The disagreement between two detectors in the calculation of β is due to inhomogeneous deformations. In Figure 4.13 it can be seen that temperature spikes can occur on one detector during the initial deformation of 4340 steel. These spikes are never observed in 2024 aluminum or Ti-6Al-4V titanium, but they occur regularly, although not consistently, in experiments with 4340 steel. Because adiabatic conditions prevail, a spike in the temperature measurement indicates that an inhomogeneity, perhaps similar to the formation of Luder's bands, has formed in the early stages of the deformation of 4340 steel. The spike disappears because the specimen is moving and the inhomogeneity translates away from the focussed detector. Notice that the other detector also shows some transient temperature rise due to the inhomogeneity. The formation of such inhomogeneities violates the assumptions of the Kolsky bar equations, Eq (4.7). Consequently, the plastic work reported for that portion of the experiment is only an *average* value and does not reflect the local value of the plastic work rate density near the inhomogeneity. At later times it is likely that the specimen is deforming more homogeneously, and, consequently, the results are more repeatable. Following the arguments used for 2024 aluminum it is concluded that strong strain dependence but no strain-rate dependence of β is observed in 4340 steel up to strain-rates of $3000 s^{-1}$.

The experiments on Ti-6Al-4V titanium indicate that it also suffered from inhomogeneous deformations. This material, however, deformed in a different fashion than

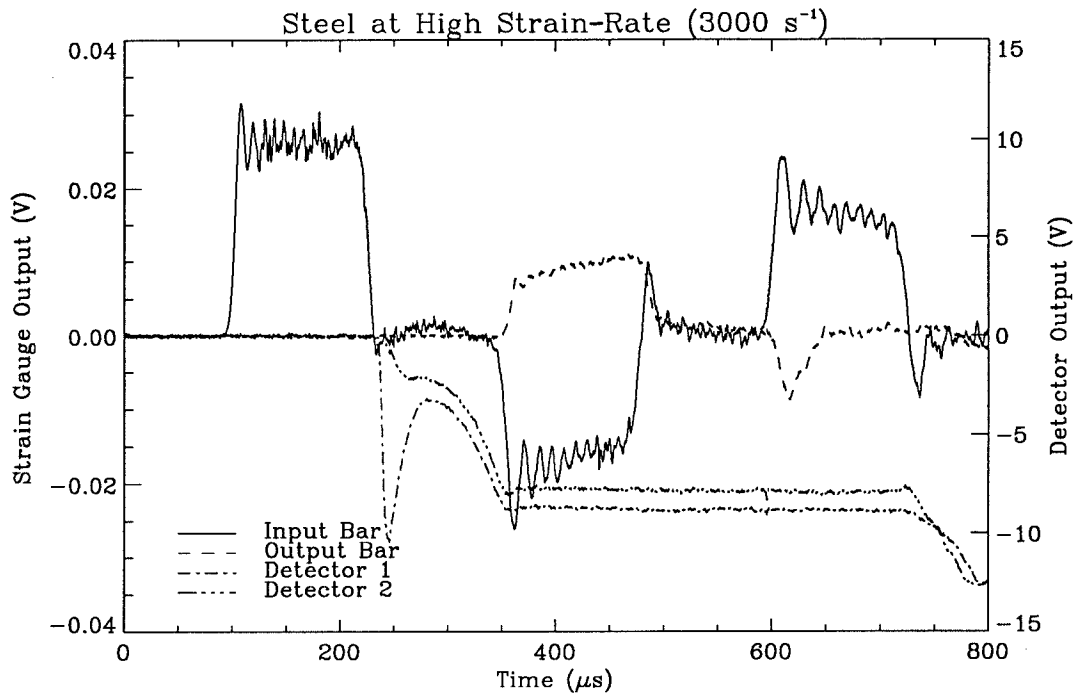

FIGURE 4.13 The raw data for an experiment using 4340 steel. These results show a spike in one of the two temperature detectors due to a localized deformation. Such spikes are not always repeatedly observed in steel although they are never observed in Ti-6Al-4V titanium or 2024 aluminum.

the steel. The Ti-6Al-4V titanium did not show large initial spikes in the temperature measurement. Rather, it deformed inhomogeneously over a larger scale, resulting in two slightly different temperature measurements for each detector over the duration of the loading. In Figure 4.14 it can be seen that the detector measurements differ not more than 10% over the full length of the experiment. However, the shape and curvature of these curves remains equivalent. It was observed that the final temperature measured varies slightly with the initial placement of the detectors along the axial coordinate of the specimen, but the shape and curvature do not vary with measurement location. Therefore, the deformation varies over more than the separation of the two detectors, 1.4 mm. Since the Kolsky bar reports an *average* measure of the plastic work rate for inhomogeneously deforming materials, an *average* of the two tempera-

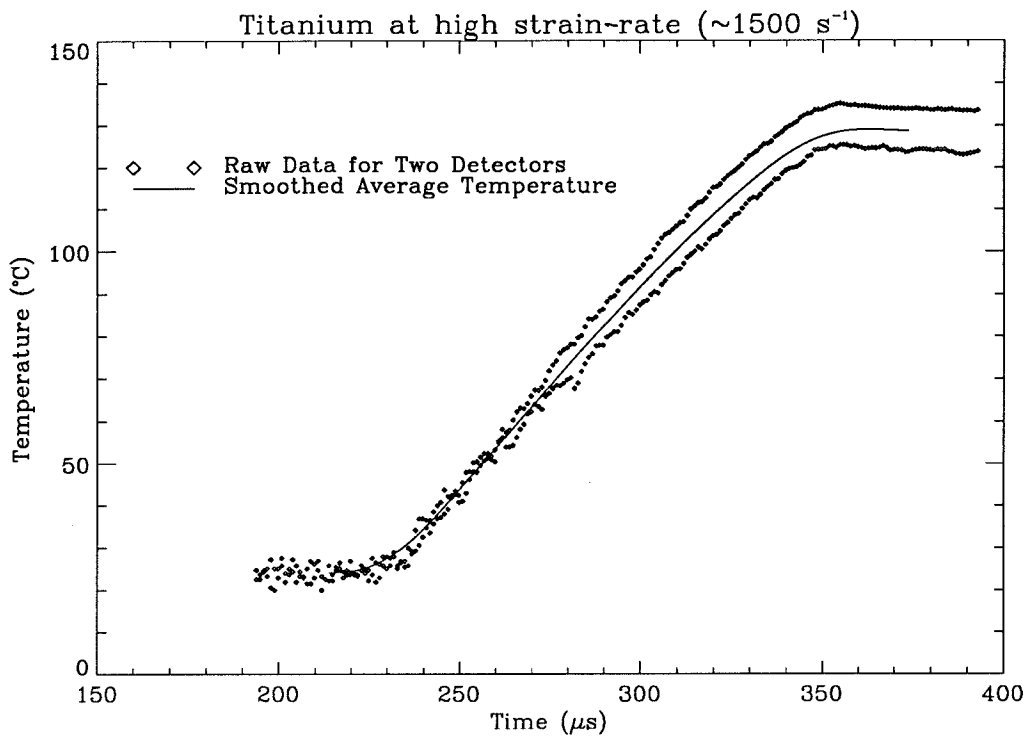

FIGURE 4.14 The temperatures measured by each of two detectors during an experiment of Ti-6Al-4V titanium are slightly different. This is due to inhomogeneous deformation over a scale that is larger than the separation of the detectors. The shape of the curve, i.e., a decreasing slope, however, is invariant with respect to measurement location.

ture measurements is used to calculate the work rate to heat rate conversion fraction, β. The result is seen in Figure 4.15. Note that the form of β for Ti-6Al-4V titanium is different than that of 2024 aluminum and that it is in better agreement with the model Zehnder (1990) at low strains (up to 5%). At higher strains the same curve is in better qualitative agreement with the model of Aravas et al. (1990). Since quasi-static measurement of the stress-strain behavior of Ti-6Al-4V titanium by the authors shows this alloy to be strain-rate sensitive, this difference between the behavior of Ti-6Al-4V and the behavior of 4340 steel or 2024 aluminum—in the same strain-rate range—may be connected to the strain-rate sensitivity of the Ti-6Al-4V titanium. Further work at lower strain-rates and using the full detector array should shed more light on this issue.

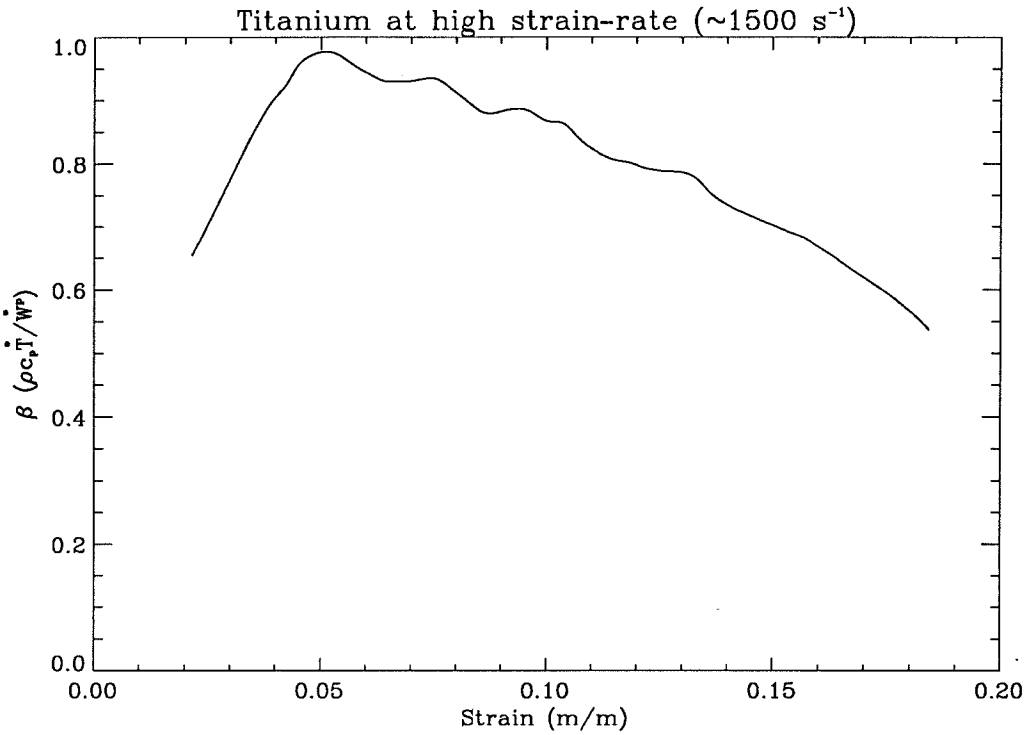

FIGURE 4.15 The work rate to heat rate conversion fraction is calculated for Ti-6Al-4V titanium using the average of the temperature of the two detectors. It is seen that the form of the result qualitatively follows the prediction of Zehnder (1991) at low strains and the prediction of Aravas et al. (1990) at high strains. (See Figure 4.1.)

4.5 Conclusions

This work describes the first attempt to quantify the functional dependence of the plastic work rate to heat rate conversion fraction, β, on strain and strain-rate in a range of metals. The main conclusions can be summarized as follows:

1. Adiabatic conditions exist in the Kolsky bar for experiments on 4340 steel, 2024 aluminum and Ti-6Al-4V titanium when experimental times were shorter than 800 μs. This fact greatly simplifies the thermomechanical analysis of specimen deformation in the Kolsky bar.

2. It is possible to measure the dependence of β upon strain and strain-rate using the Kolsky bar and high-speed temperature detectors provided the specimen

deforms uniformly or nearly uniformly.

3. For nominally strain-rate independent solids, the dependence of β upon strain at high strain-rate (1000–3000 s^{-1}) roughly follows the dependence expected at low strain-rates. The model of Zehnder (1991) produces an acceptable qualitative prediction of this dependence. Consequently, significant strain-rate dependence of β for 2024 Al and 4340 steel is not detected over a large range of strain-rates (10^{-3} to 10^{3} s^{-1}). However, this is to be expected since neither materials showed strain-rate dependence in their mechanical properties.

4. Strain-rate sensitive Ti-6Al-4V titanium exhibited interesting behavior at high strain-rates. The measured dependence of β upon strain for this material did not follow the qualitative trends observed in strain-rate insensitive 2024 aluminum and 4340 steel. The model of Zehnder (1991) qualitatively described β at low strains while the model of Aravas et al. (1990) gave a better qualitative description at high strains. This difference may be connected to the strain-rate sensitivity of the material. Further investigation is required.

5. The reflection of input stress waves from the free end of the input bar of the Kolsky bar lead to significant temperature rises in the specimen subsequent to the conclusion of the initial, recorded loading. This fact must be considered if post-mortem examination of the specimens is to be performed since material microstructure may be influenced by the high temperatures generated during repeated loading. Repeated loading can be eliminated using the a stress reversal Kolsky bar set up (Nemat-Nasser et al., 1991).

These results have significant implications in the study of the conditions preceeding and governing adiabatic shear band formation and shear band growth as well as on the

establishment of a criterion governing dynamic failure mode selection in rate sensitive materials. This is because the work rate to heat rate conversion fraction, β, serves as a measure of the strength of the coupling term, in Eq (4.1), between the temperature and mechanical fields. The temperature rise governed by Eq (4.1) can be significant leading to thermal softening and to subsequent shear localization in many materials. When modelling thermomechanical behavior of materials β is usually assumed to be a constant. For example, in thermomechanical models of shear band formation (Clifton et al., 1984; T. Belytschko et al., 1991; Wright and Ockendon, 1992), in thermomechanical finite element simulations of dynamic failure mode transitions (Lee, 1990) and in general thermomechanical computational codes (Simo and Miehe, 1992), β is assumed to be a constant in the traditionally accepted range of 0.85-1.00. However, as shown here, this assumption may not be correct for all metals, and serious consideration of the variation of β with strain and strain-rate may be necessary to properly account for the strength of the thermomechanical coupling and to accurately model material behavior. For example, β in Ti-6Al-4V deformed at high strain-rates is significantly dependent upon strain, and, for strains higher than 5%, β decreases from 1 to 0.5 (at 20%, see Figure 4.15). This decreasing trend may continue for strains beyond 20%. Also, this strong variation of β with strain may suggest that β is dependent upon strain-rate as well. Such strain and strain-rate sensitivity in the mechanism of converting plastic work to heat for this material may play an important role in the determination of the width of shear localization zones, in the determination of the maximum temperature in such zones and, ultimately, in the determination of a critical shear localization or failure mode selection criterion.

References

1. N. Aravas, K-S. Kim and F.A. Leckie (1990), On the calculations of the stored energy of cold work, *J. Eng. Mat. Tech.*, **112**, 465

2. *Aerospace Structural Materials Handbook* (1989), Metals and Ceramics Information Center, Battelle Columbus Laboratories, Columbus, Ohio

3. R.C. Batra and T.W. Wright (1988), A comparison of solutions for adiabatic shear banding by forward-difference and crank-nicolson methods, *Commun. Appl. Num. Meth.*, **4,** 741

4. M.B. Bever, D.L. Holt and A.L. Titchener (1973), The stored energy of cold work, *Prog. Mat. Sci.*, **17,** 1

5. W.H. Beyer (1987), *CRC Standard Mathematical Tables, 28th Edition,* CRC Press, Inc., Boca Raton, Florida, 449

6. T. Belytschko, B. Moran and M. Kulkarni (1991), On the crucial role of imperfections in quasi-static viscoplastic solutions, *J. Appl. Mech.*, **58,** 658

7. R.J. Clifton, J. Duffy, K.A. Hartley and T.J. Shawki (1984), On critical conditions for shear band formation at high strain-rates, *Scr. Met.*, **18,** 443

8. G.F.D. Duff and D. Naylor (1966), *Differential Equations of Applied Mathematics,* J.Wiley & Sons, New York

9. J. Duffy (1984), Temperature measurements during the deformation of shear bands in a structural steel, G.J. Dvorak and R.T. Shield, eds., *Mechanics of Material Behavior,* Elsevier Science Pub. B.V., Amsterdam, 75

10. P.S. Follansbee (1985), The split Hopkinson bar, *Metals Handbook; 9th Edition,* American Society for Metals, Metals Park OH, **8,** 198

11. P.S. Follansbee and C. Frantz, Wave propagation in the split Hopkinson pressure bar, *J. Engr. Matls. Tech.*, **105,** 61

12. J.H. Giovanola (1988), Adiabatic shear banding under pure shear loading, Part I: Direct observation of strain localization and energy dissipation measurements, *Mech. Matls.*, **7,** 59

13. C.W. Groetsch (1992), Optimal order of accuracy in Vasin's method for differentiation of noisy functions, *Journal of Optimization Theory and Applications,* **74,** 373

14. H.Kolsky (1949), An investigation of the mechanical properties of materials at very high rates of loading, *Proc. Royal Soc. B,* **62,** 676

15. Y.J. Lee (1990), Problems associated with dynamic fracture under high strain-rate loading, *Ph.D. Thesis, Division of Engineering, Brown University*

16. U.S. Lindholm (1964), Some experiments with the split Hopkinson pressure bar, *J. Mech. Phys. Sol.*, **12,** 317

17. S. Nemat-Nasser, J.B. Isaacs and J.E. Starret (1991), Hopkinson techniques for dynamic recovery experiments, *Proc. R. Soc. London., A,* **435,** 371

18. M.N. Ozisik (1980), *Heat Conduction,* J.Wiley & Sons, New York

19. A.J. Rosakis, J.J. Mason and G. Ravichandran (1992), The conversion of plastic work to heat around a dynamically propagating crack in metals, to appear *Journal of Mechanical Behavior of Materials*

20. J.C. Simo and C. Miehe (1992), Associative coupled thermoplasticity at finite strains-formulation, numerical analysis and implementation, *Comput. Meth.,* **98,** 41

21. I.N. Sneddon and D.S. Berry (1958), The classical theory of elasticity, in S. Flugge, ed., *Handbuch der Physik,* Vol. VI, Springer Verlag, Berlin, 123

22. G.I. Taylor and M.A. Quinney (1934), The latent energy remaining in a metal after cold working, *Proc. Roy. Soc. London A,* **143,** 307

23. V.V. Vasin (1973), The stable evaluation of a derivative in the space $C(-\infty,\infty)$, *USSR Comp. Math. Math. Phys.,* **13,** 16

24. R.O. Williams (1965), The stored energy of copper deformed at 24°C, *Acta Metall.,* **13,** 163

25. T.W. Wright and H. Ockendon (1992), A model for fully formed shear bands, *J. Mech. Phys. Sol.,* **40,** 1217

26. A.T. Zehnder (1991), A model for the heating due to plastic work, *Mechanics Research Communications,* **18,** 23

27. A.T. Zehnder and A.J. Rosakis (1991), On the temperature distribution at the vicinity of dynamically propagating cracks in 4340 steel, *J. Mech. Phys. Sol.,* **39,** 385

28. A.T. Zehnder and A.J. Rosakis (1993), Temperature rise at the tip of dynamically propagating cracks: measurements using high-speed infrared detectors, to appear in *Experimental Techniques in Fracture,* **III**

Part II:

An Effect of Heating at a Dynamic Crack Tip; The Formation of a Shear Instability

CHAPTER 5

On the Use of a Coherent Gradient Sensor in Dynamic Mixed-Mode Fracture Mechanics Experiments

Overview

The use of a coherent gradient sensing (CGS) apparatus is explored in dynamic fracture mechanics investigations. The ability of the method to accurately quantify mixed-mode crack tip deformation fields is tested under dynamic loading conditions. The specimen geometry and loading follow that of Lee and Freund (1990a) and (1990b) who give the theoretical and numerical mixed mode K values as a function of time for the testing conditions. The CGS system's measurements of K_I and K_{II} are compared with the predicted results, and good agreement is found. The method is used to measure K beyond the time domain of the known solution; it is seen that a shift from primarily Mode II deformation to primarily Mode I deformation occurs.

List of Symbols

K_I, K_{II}	mode I, II stress intensity factors
K'	normalization for stress intensity factor
ν, E	Poisson's ratio and Young's modulus
x_1, x_2	Cartesian coordinates;
	x_1 along crack line,
	x_2 perpendicular to crack line
$\sigma_{ij}, \epsilon_{ij}, u_i$	Cartesian stress, strain and displacement components
$v(t)$	impact velocity
v_o	velocity magnitude
λ	wavelength of light
c_R, c_S, c_d	Rayleigh, shear and dilatational wave speeds
δS	optical path difference
ϵ	shearing distance of light beams
Δ	grating separation
p	grating pitch
m, n	integer fringe order
n_o	refractive index of undeformed material
D_1	stress optical constant
h	specimen thickness
l	crack length

5.1 Introduction

In an effort to understand dynamic mixed mode crack initiation as well as rapid crack growth, various optical techniques have been used extensively for direct determination of dynamic crack tip fields. The method of photo-elasticity, for instance, has been used to obtain both the dynamic fracture initiation and propagation toughnesses of transparent, optically anisotropic materials such as Homalite 100.[Dally (1979)] The method of caustics, on the other hand, has been used to study dynamic fracture behavior of transparent solids such as PMMA and Homalite 100 [Theocaris and Gdoutos (1972) and Ravi-Chandar and Knauss (1984)] as well as opaque materials such as steel [Rosakis and Zehnder (1985)]. For a review of the method of caustics or the method of photo-elasticity see Kalthoff (1987b) or Burger (1987), respectively.

The method of caustics has been used in a variety of fracture mechanics experiments [Rosakis and Zehnder (1985), Theocaris and Gdoutos (1972), Ravi-Chandar and Knauss (1984) and Beinert and Kalthoff (1981)]. This technique, however, inherently assumes that the stress field near the crack tip is well described by the dominant $(r^{-\frac{1}{2}})$ singular term of the asymptotic expansion (K-dominance). If the K-dominance approximation is not valid in regions where measurements are performed, the method of caustics can produce erroneous results in its measurement of K_I or K_{II}. Furthermore, if there is limited knowledge of the crack tip deformation field (consider the formation of an adiabatic shear band at a crack tip), the method of caustics can give little information about the deformation. Consequently, a full-field method is experimentally more advantageous because it can offer a more complete description of the deformation and response of the specimen over a larger region and not along a single curve as in caustics. The method of photo-elasticity is a full-field technique, but this method is limited to optically birefringent materials.

The full-field method known as the coherent gradient sensor, CGS [Tippur et al.

(1989a) and (1989b)] is investigated here for the measurement of mixed-mode, dynamic crack tip deformation fields under plane stress conditions in optically transparent, non-birefringent materials. The Coherent Gradient Sensor is a lateral shear interferometer utilizing two identical line gratings. The set-up was first proposed for measuring lens abberations, [Hariharan et al. (1974) and Hariharan and Hegedus (1975)] but, until recently, other possible applications of the CGS interferometer have been overlooked. When used in fracture mechanics the method gives real time measurements of the in-plane stress gradients for transparent materials or the in-plane gradients of the out-of-plane displacements for opaque materials. With data taken at a wide range of points near the crack tip, it is possible for the CGS method both to show whether or not a K-dominant field exists near the crack tip and to find accurate values of K_I and K_{II}.

Tippur et al. (1989a) and (1989b) have demonstrated the accuracy of the CGS statically for mode I loading, however, its accuracy in dynamic investigations, including dynamic mixed-mode loading, has not been reported.

Recently, Kalthoff and Winkler (1987) and Kalthoff (1987a) have observed interesting behavior in the dynamic propagation of mixed-mode (mostly mode II) cracks in steel. Double-notched specimens were impacted by a projectile travelling with speeds up to 70 m/s, see Figure 5.1a. It was found that below a certain impact speed (depending upon the root radius of the notch) dynamic cracks propagated at a deflected angle of approximately 70° form the notch line. This behavior is to be expected if the material fails in a brittle fashion under a maximum hoop stress criterion [Erdogan and Sih (1963)]. Above a critical impact speed, however, failure occurs along a direction at a much smaller angle. Further investigation suggests that at high impact speeds (high strain-rate) failure occurs in an adiabatic shear banding mode.

An analysis of the experiment of Kalthoff and Winkler (1987) and Kalthoff (1987a) by Lee and Freund (1990a) shows that both modes of deformation, mode I and mode

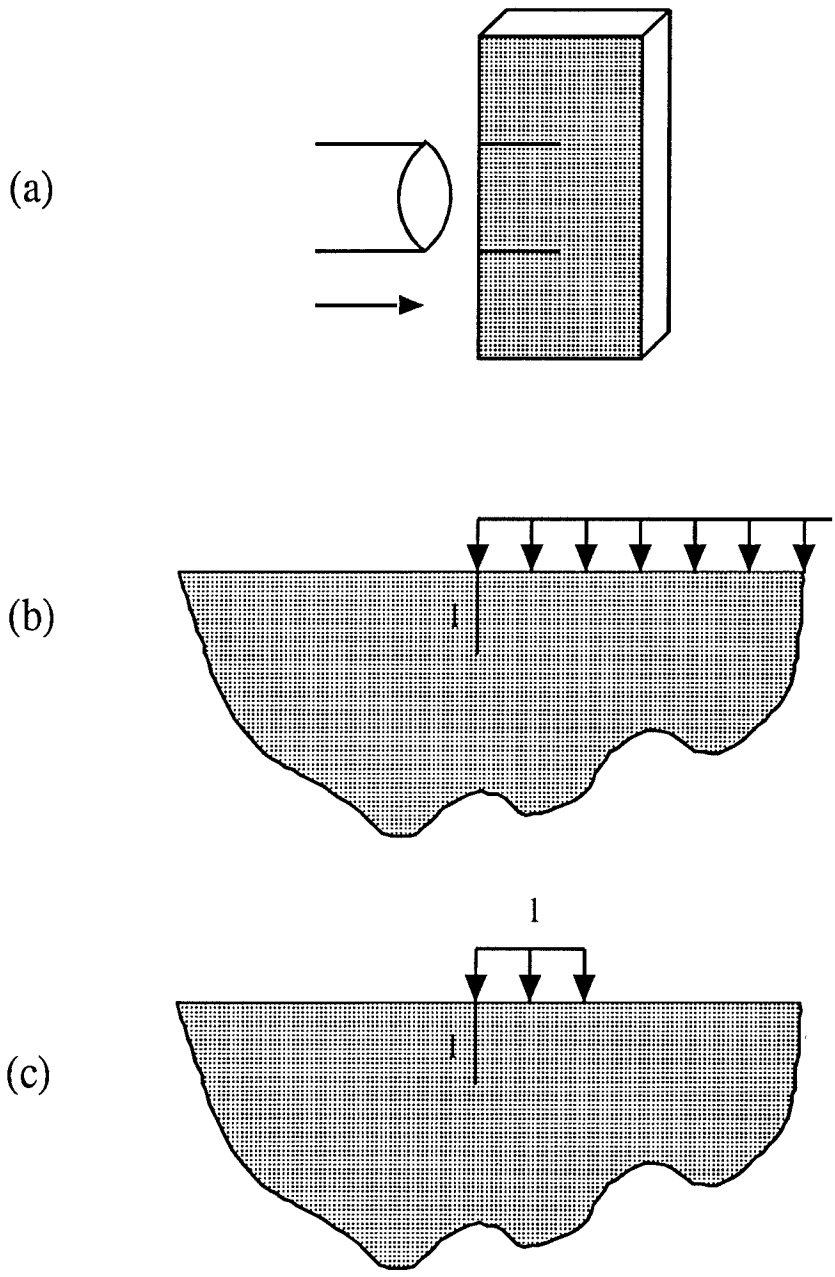

FIGURE 5.1 Loading configuration and geometry for (a) experiments of Kalthoff (1987) and Kalthoff and Winkler (1987), (b) theoretical solutions of Lee and Freund (1990a) and (c) finite element solution of Lee and Freund (1990b).

II, can be expected for such a loading geometry. In fact, apart from the dominant K_{II}, a small negative K_I is also predicted. Lee and Freund indicate limited agreement of the mode II stress intensity factor predicted by their analysis with the caustics measurements of Kalthoff and Kalthoff and Winkler. In these measurements, the caustics patterns were interpreted as corresponding to a pure mode II deformation field. Hence, no values of K_I are reported. The limited agreement of the theoretical results with the experimental measurements may be attributed to a failure of the assumption of K-dominance, which was not thoroughly substantiated in the experiments.

It is important that the Lee-Freund analysis of the experiment be verified so that understanding of the failure mode transition from brittle cracking to adiabatic shear banding can be achieved. Knowledge of the existence and magnitude of a K field at the crack tip could lead to a clearer understanding of the mechanisms behind this failure mode transition.

5.2 Theoretical Development

5.2.1 Analytical Model

The problem investigated by Lee and Freund (1990a) is shown in Figure 5.1b. One side of an elastic, half-space containing an edge crack is loaded dynamically by some prescribed velocity, $v(t)$. All other faces are traction free so the boundary conditions to be satisfied are

$$\left.\begin{aligned}\sigma_{11}(-l,x_2,t)&=0\\ \sigma_{12}(-l,x_2,t)&=0\end{aligned}\right\}\ \text{if } x_2<0,\qquad \left.\begin{aligned}\sigma_{12}(-l,x_2,t)&=0,\\ u_1(-l,x_2,t)&=\int_0^t v(\tau)\,d\tau\end{aligned}\right\}\ \text{if } x_2>0,$$

$$\left.\begin{aligned}\sigma_{22}(x_1,0^{\pm},t)&=0\\ \sigma_{12}(x_1,0^{\pm},t)&=0\end{aligned}\right\}\ \text{if } -l<x_1<0,$$

and at $t = 0$ all quantities are zero. x_1 and x_2 are coordinates along the crack line and perpendicular to it, respectively. An elastic plane strain solution to this problem is reported by Lee and Freund (1990a) for a step input velocity, $v(\tau) = v_o H(\tau)$, but conditions in our experiment are closer to a plane stress situation. As a result, the analysis was adjusted to reflect a plane stress field. This was achieved by substituting for ν with the quantity $\frac{\nu}{\nu+1}$ in the results for K_I and K_{II}. Note that K_I and K_{II} in this problem depend on material constants, namely ν, because a velocity boundary condition is prescribed on part of the boundary.

For PMMA $\nu \approx .35$ and $\frac{\nu}{\nu+1} = .26$, therefore the analysis was evaluated numerically for $\nu = .26$ The normalization factor, K', for the stress intensity factors is given by

$$K' = \begin{cases} \sqrt{\frac{l}{\pi}} \frac{E v_o}{2 c_d^{pl-\sigma}} & \text{for plane stress} \\ \sqrt{\frac{l}{\pi}} \frac{E v_o}{2 c_d^{pl-\epsilon}(1-\nu^2)} & \text{for plane strain} \end{cases} \tag{5.1}$$

where the plane stress normalization factor is found using the above substitution for ν in the plane strain normalization factor given by Lee and Freund (1990a). The time axis is normalized by the characteristic time, $l/c_d^{pl-\sigma}$ where $c_d^{pl-\sigma}$ is the plane stress dilatational wave speed. The results of the new calculations for both mode I and mode II stress intensity factors are shown in Figures 5.2a and 5.2b, respectively. As expected, these results are very close to the results of Lee and Freund (1990a) for $\nu = .25$.

Most of the qualitative features of the curves in these figures can be explained. Upon impact a plane compressive wave is generated. It is followed by cylindrical unloading waves generated at the corners of the impact area. The compressive wave gives rise to K_{II}. The existence of the unloading wave makes the increase in K_{II} progressively more gradual and forces the crack faces to close, thus causing a smaller, but significant, negative K_I. As can be seen in Figures 5.2a and 5.2b there exist three regions in the solution. These correspond to the arrivals at the crack tip of the first dilatational, shear and Rayleigh waves, respectively. The solution is valid up

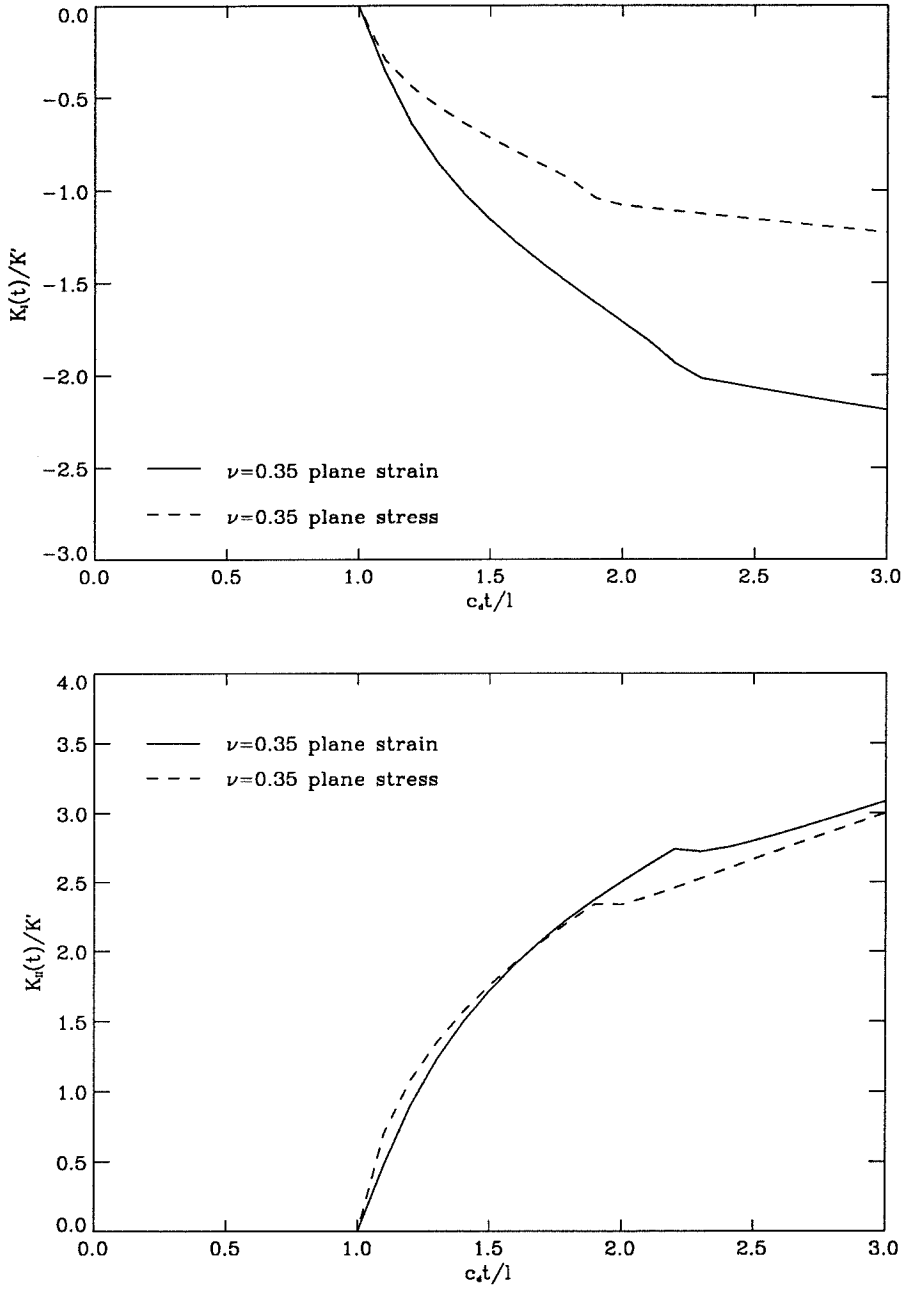

FIGURE 5.2 (a) Theoretical predictions for $K_I(t)$ from the analysis of Lee and Freund (1990a) for PMMA, $\nu = .35$, under plane strain and plane stress conditions. (b) Theoretical predictions for $K_{II}(t)$ from the analysis of Lee and Freund (1990a) for PMMA, $\nu = .35$, under plane strain and plane stress conditions.

to $c_d t/l = 3$, which corresponds to the arrival of a second dilatational wave that is reflected from the impact surface.

5.2.2 *The Method of CGS*

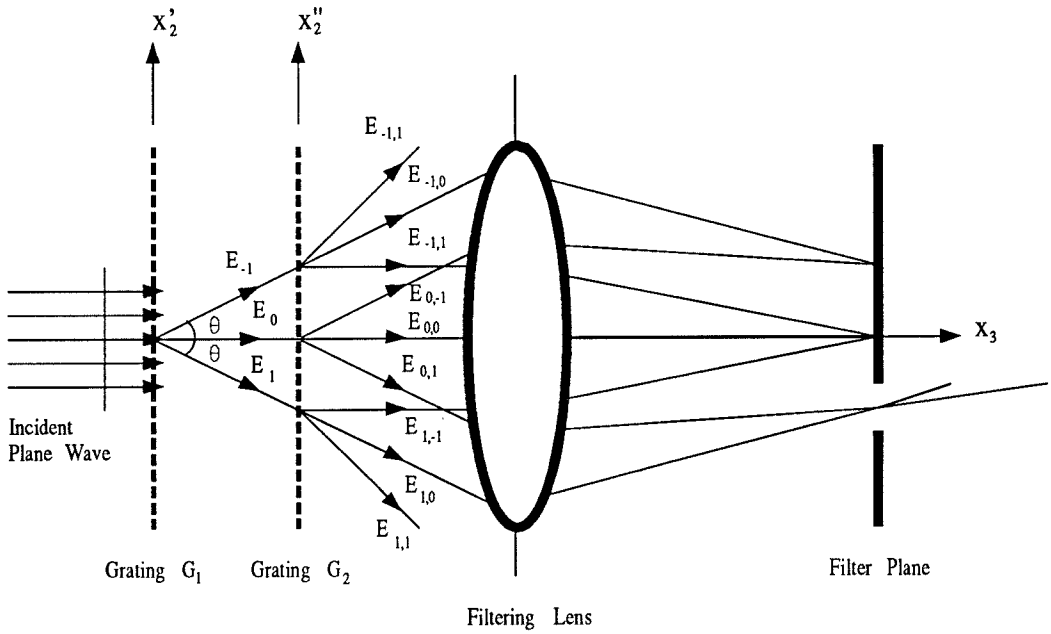

FIGURE 5.3 Schematic describing the working principle of CGS.

In contrast to Tippur et al. (1989a) and (1989b), the theoretical development of CGS shown here follows the more traditional approach of Murty (1978) for lateral shearing interferometers. The two approaches are equivalent; the same assumptions are made and the same governing equations result. It is hoped that the more traditional development will result in an easier understanding of the method. A schematic of the set-up is shown in Figure 5.4. A coherent, collimated laser beam, 50 mm in diameter, passes through a notched transparent specimen. After exiting from the deformed specimen, the beam falls upon the first of two identical diffraction gratings (40 lines/mm).

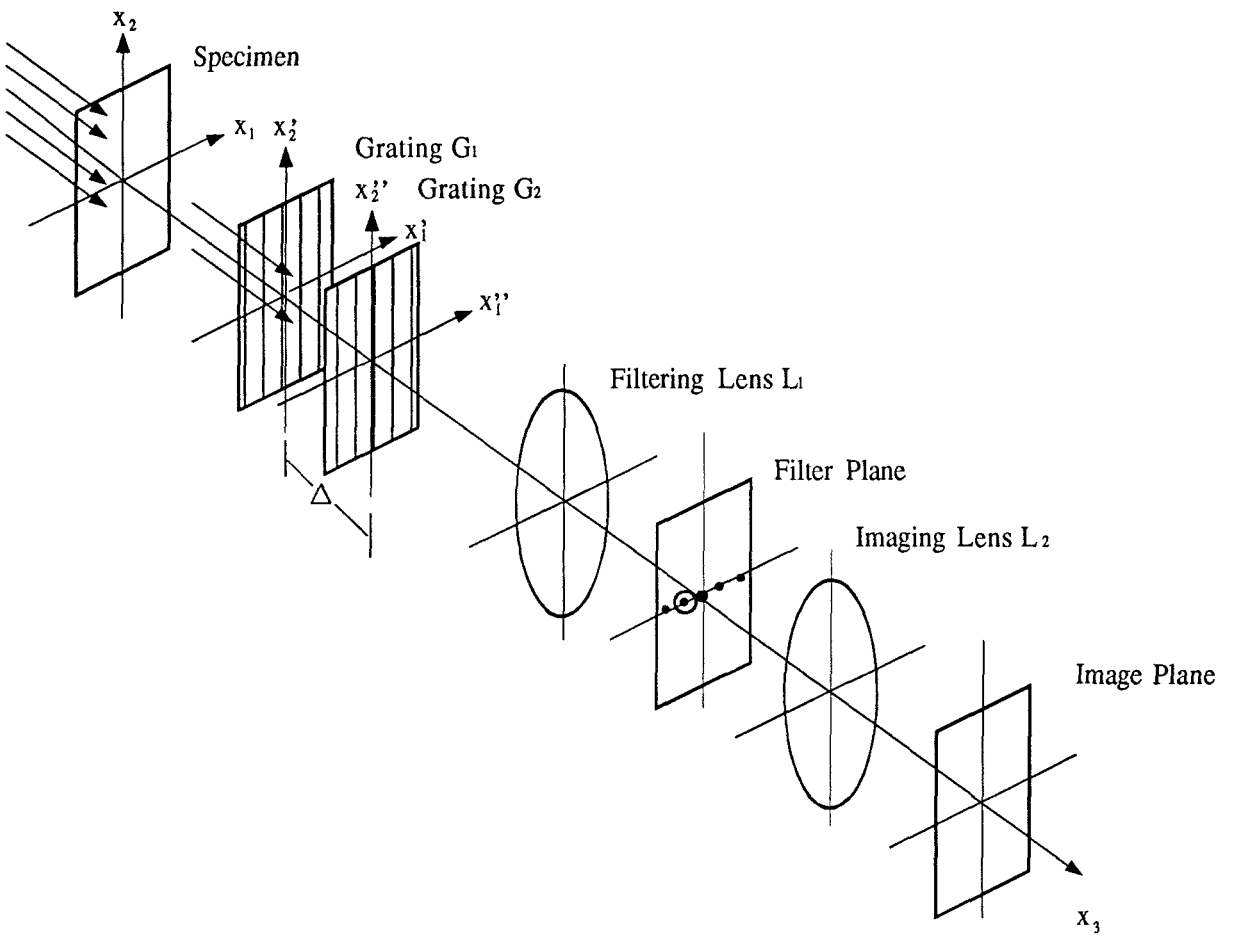

FIGURE 5.4 Schematic of the experimental set up for transmission CGS.

The primary grating splits the beam into a direct beam and numerous diffraction orders. For the sake of brevity, only the first diffraction orders (± 1) and the direct beam are considered. The second diffraction grating diffracts both the direct beam and the first diffraction orders into three beams each, giving a total of nine beams behind the second grating. Of these nine beams the (0,$\pm$1) and the ($\pm$1,0) orders are parallel—as can be seen in Figure 5.3.

An on-line spatial filter is used to isolate one of the two pairs of parallel beams. A lens is placed a distance equal to its focal length behind the secondary grating as in Figure 5.4. The Fourier Transform of the intensity distribution at the second grating is observed in the back-focal plane of the lens where an aperture is placed on either the +1 or -1 diffraction order spot. The aperture filters all but the two desired parallel beams from the wavefront. Another lens is placed at a distance equal to its focal length behind the aperture to invert the Fourier transformation.

It is assumed that the wave front before the first grating is approximately planar with some phase difference, $\delta S(x_1, x_2)$. Deviations of the propagation direction from the optical axis are neglected. Thus, the two gratings shift one beam with respect to the other by a distance

$$\epsilon = \Delta tan\theta \approx \Delta\theta \tag{5.2}$$

where Δ is the separation between the gratings, see Figure 5.4, and θ is the angle of diffraction (assumed small), given here by

$$\theta = sin^{-1}\frac{\lambda}{p} \approx \frac{\lambda}{p}. \tag{5.3}$$

λ is the wavelength of the illumination, and p is the pitch of gratings.

The two parallel, sheared wavefronts constructively interfere at a point if their difference in phase is an integer multiple of the wavelength, i.e., if

$$\delta S(x_1 + \epsilon, x_2) - \delta S(x_1, x_2) = m\lambda, \tag{5.4a}$$

where m is called "the fringe order." Dividing this equation by ϵ gives

$$\frac{\delta S(x_1+\epsilon, x_2) - \delta S(x_1, x_2)}{\epsilon} = \frac{m\lambda}{\epsilon}, \tag{5.4b}$$

which, for sufficiently small ϵ, may be approximated by

$$\frac{\partial(\delta S(x_1, x_2))}{\partial x_\alpha} = \frac{mp}{\Delta}. \tag{5.5}$$

In equation (5.5), the approximations in equations (5.2) and (5.3) have been used, and the result has been generalized to include shearing in either the x_1 or x_2 direction, $\alpha = 1, 2$.

Equations (5.4a) and (5.4b) are the standard equations for lateral shearing interferometry found in Murty (1978). Note that as ϵ goes to zero the approximation in equation (5.5) grows more exact, but at the same time the number of fringes and, therefore, the sensitivity of the system, is decreased. It is important that the grating separation, Δ, and, consequently, the value of ϵ, appropriately balances the competition between maximizing sensitivity and approximating the derivative.

For a transparent material, the phase difference, $\delta S(x_1, x_2)$, in equations (5.4a) and (5.4b), is given by the difference in optical path length. Two important factors are included in calculating this parameter; the change in refractive index of the material due to variations in hydrostatic stress, and changes in specimen thickness due to Poisson's contraction. The optical path difference is, thus, given by

$$\delta S(x_1, x_2) = 2h(n_o - 1)\int_0^{\frac{1}{2}} \epsilon_{33}\, d\left(\frac{x_3}{h}\right) + 2h\int_0^{\frac{1}{2}} \delta n_o\, d\left(\frac{x_3}{h}\right), \tag{5.6}$$

where n_o is the index of refraction of the undeformed material and h is the thickness. The first term in equation (5.6) represents the optical path difference due to changes in the plate thickness caused by the strain component, ϵ_{33}. The second term represents the optical path difference accumulated due to stress induced change in refractive index given by the Maxwell relation,

$$\delta n_o(x_1, x_2) = D_1(\sigma_{11} + \sigma_{22} + \sigma_{33}), \tag{5.7}$$

where D_1 is the stress-optic constant and σ_{ij} are the Cartesian stress components. Assuming the material is isotropic and linearly elastic and using the plane stress assumption substitution of (5.7) into (5.6) yields [Tippur et al. (1989a) and (1989b)]

$$\delta S(x_1, x_2) \approx \bar{c}h(\hat{\sigma}_{11} + \hat{\sigma}_{22}) , \tag{5.8}$$

where $\bar{c} = D_1 - \frac{\nu}{E}(n_o - 1)$ and $\hat{\sigma}_{11}$ and $\hat{\sigma}_{22}$ are plane stress thickness averages of stress components in the material while $\hat{\sigma}_{33} = 0$. Finally, substituting (5.8) into (5.5) gives the result,

$$\bar{c}h\frac{\partial(\hat{\sigma}_{11} + \hat{\sigma}_{22})}{\partial x_\alpha} \approx \frac{mp}{\Delta}. \tag{5.9}$$

All interference images produced by the CGS apparatus are interpreted using equation (5.9). A similar analysis may be carried out for opaque materials in reflection giving results with the same form.[Tippur et al. (1989a) and (1989b)]

For the case of a mixed-mode, K-dominant deformation field at a crack tip,

$$(\hat{\sigma}_{11} + \hat{\sigma}_{22}) = \frac{2}{\sqrt{2\pi r}}(K_I cos\frac{\phi}{2} - K_{II} sin\frac{\phi}{2}), \tag{5.10}$$

where $r = \sqrt{x_1^2 + x_2^2}$ and $\phi = tan^{-1}(x_2/x_1)$. x_1 and x_2 are the coordinates along the crack length and perpendicular to the crack length, respectively, with the origin at the crack tip. Equation (5.9) indicates that constructive fringes are formed if

$$A\frac{sin\frac{3}{2}(\phi - \psi)}{\sqrt{2\pi r^3}} = \frac{mp}{\Delta \bar{c}h} \qquad \text{for } x_1 \text{ gradients,} \tag{5.11a}$$

or

$$A\frac{cos\frac{3}{2}(\phi - \psi)}{\sqrt{2\pi r^3}} = \frac{mp}{\Delta \bar{c}h} \qquad \text{for } x_2 \text{ gradients,} \tag{5.11b}$$

where $K_I/K_{II} = tan(3\psi/2)$, and $A = K_{II}/cos(3\psi/2)$.

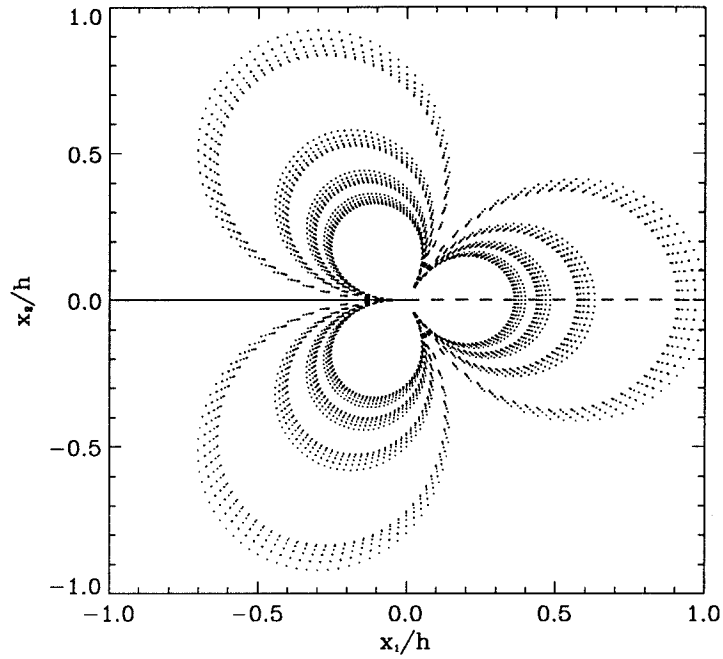

FIGURE 5.5 (a) Numerical predictions of CGS fringes (constant $\frac{\partial(\hat{\sigma}_{11}+\hat{\sigma}_{22})}{\partial x_\alpha}$ values) constructed on the basis of a pure K_I field.

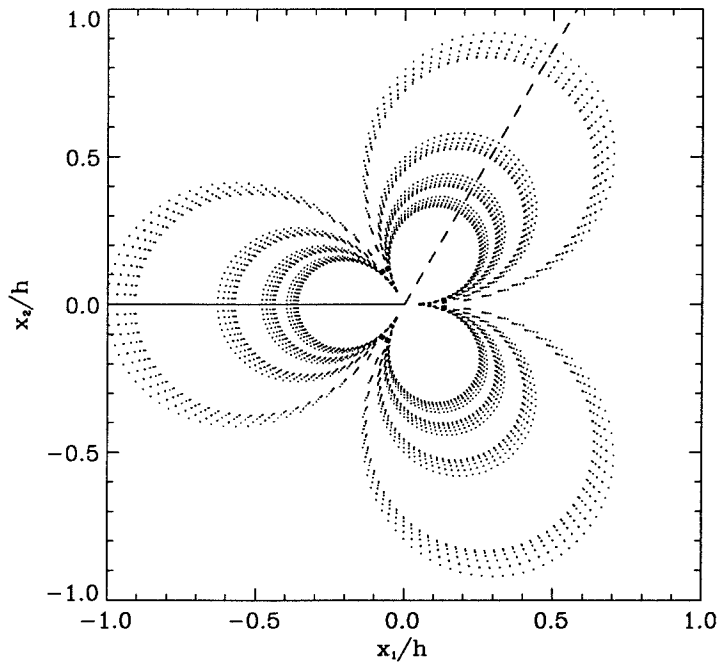

FIGURE 5.5 (b) Numerical predictions of CGS fringes (constant $\frac{\partial(\hat{\sigma}_{11}+\hat{\sigma}_{22})}{\partial x_\alpha}$ values) constructed on the basis of a pure K_{II} field.

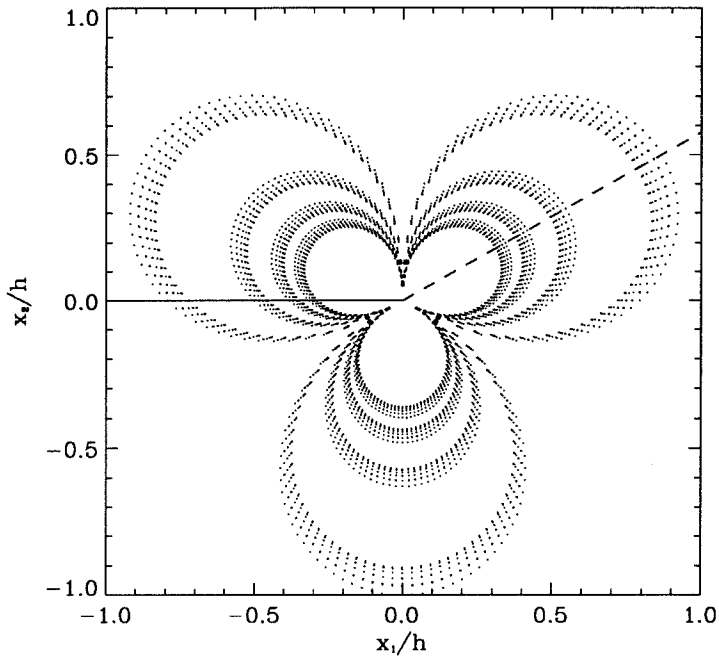

FIGURE 5.5 (c) Numerical predictions of CGS fringes (constant $\frac{\partial(\hat{\sigma}_{11}+\hat{\sigma}_{22})}{\partial x_\alpha}$ values) constructed on the basis of a mixed mode K field, $K_I = K_{II}$.

An example of the fringe pattern expected from equation (5.11a) is shown in Figure 5.5a for $K_{II} = 0$ and Figure 5.5b for $K_I = 0$. A change in the ratio K_I/K_{II} results in a rotation and/or magnification of the fringe pattern, as seen in Figure 5.5c.

5.3 Experimental Procedure

5.3.1 Apparatus

The specimen geometry is shown in Figure 5.6. Specimens are made of PMMA because it approximates the linear elastic assumption of the theoretical solution. Square-tip notches $\approx 1.5mm$ thick are cut on a band saw as per the figure. The inclusion of a notch of finite opening rather than a crack allows the generation of a negative mode-I stress field at the notch tip (as long as the notch faces do not come into contact). Thus, the mode-I response of the system can be investigated.

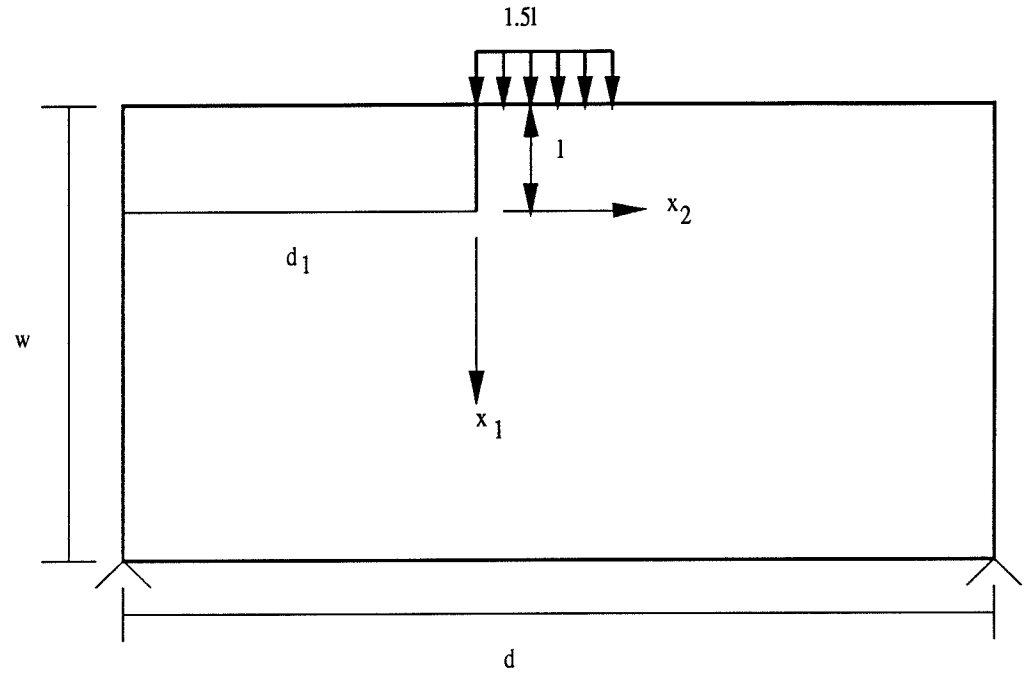

Dimesions of specimen:
l=25 mm
w=127 mm
d=254 mm
d_1=136 mm
thickness=7.5 mm

Mechanical Properites of specimen:
E=1240 MPa
v=0.35
c=1.08 10^{-10} Pa
c_d^{pl-o} =1765 m/s

FIGURE 5.6 Specimen geometry, loading configuration and material constants.

Impact of the specimens is achieved using a Dynatup drop weight tower. The contact area of the drop weight tup is made of steel, and the corners are rounded to reduce stress concentration. The weight is dropped from approximately 1.4 m giving it a velocity of 5.25 m/s at impact. Including the impedance mismatch of the two materials, this results in a contact interface velocity between the specimen and the drop weight of ≈5 m/s.

Set up of the CGS apparatus follows Figure 5.4. A streak camera is used as the imaging system. The CGS interferograms are generated using an Argon-Ion laser pulsed for 50 ns at 7 μs intervals as the light source. The total length of the test is ≈ 300 μs resulting in approximately 40 CGS interferograms per test.

The fringe patterns are digitized by hand. A ray of constant ϕ from the crack tip is followed; points at the center of fringes are digitized along the way. Most of the uncertainty in digitization arises from locating the crack tip and choosing the center of the fringe. Uncertainties in the measurement of ϕ are minimal.

5.3.2 Data Reduction

Rearranging equation (5.11a) gives

$$\frac{m_i p}{\Delta \bar{c} h} \sqrt{2\pi r_i^3} = Y_i \tag{5.12}$$

where $Y_i = A sin\frac{3}{2}(\phi_i - \psi)$ and the subscript i refers to individually digitized points. The left-hand side of this equation is obviously constant for fixed ϕ, K_I and K_{II}. If K-dominance is exhibited, plotting the left side of equation (5.12) with respect to r should result in a horizontal line. K-dominance was studied by producing such plots and investigating their slope.

Deviation of experimental results from the fringe patterns predicted by a K-dominant field are expected for various reasons. These include the notch tip geometry, the zone around the notch tip where plane stress assumptions break down (the

3-D zone)[Rosakis and Ravi-Chandar (1986) and Krishnaswamy et al. (1988)] and the finite specimen size. Once a region of K-dominance is located, however, a fit of the expected fringe pattern to the digitized data points can be attempted. This fit is produced by minimizing the error function

$$\chi(K_I, K_{II}) = \sum_{i=1}^{N} \left(r_i^{\frac{3}{2}} - \hat{r}^{\frac{3}{2}}(\phi_i, m_i, K_I, K_{II}) \right)^2 , \tag{5.13}$$

where

$$\hat{r}^{\frac{3}{2}}(\phi_i, m_i, K_I, K_{II}) = \frac{\Delta \bar{c} h}{m_i p \sqrt{2\pi}} \left[K_{II} sin\left(\frac{3\phi_i}{2}\right) - K_I cos\left(\frac{3\phi_i}{2}\right) \right], \tag{5.13a}$$

and N is the total number of points. The minimization of equation (5.13) results in a linear set of equations for K_I and K_{II}. It is noted that the function, χ, inherently weights the outer lobes of the interferograms more strongly than the inner lobes. Another function was tested, namely,

$$\tilde{\chi}(K_I, K_{II}) = \sum_{i=1}^{N} (m_i - \hat{m}(\phi_i, r_i, K_I, K_{II}))^2 .$$

where

$$\hat{m}(\phi_i, r_i, K_I, K_{II}) = \frac{\Delta \bar{c} h}{p \sqrt{2\pi r_i^3}} \left[K_{II} sin\left(\frac{3\phi_i}{2}\right) - K_I cos\left(\frac{3\phi_i}{2}\right) \right],$$

This function weights the inner lobes more heavily, but results similar to those reported here are found.

5.4 Results and Discussion

A series of shearing interferograms is shown in Figure 5.7. Comparison to Figure 5.5b shows that the fringes represent a primarily mode II type of deformation at a short time after impact ($c_d t/l \leq 3$). In analogy to observed near-tip three-dimensional effects in mode-I deformation [Rosakis and Ravi-Chandar (1986) and Krishnaswamy

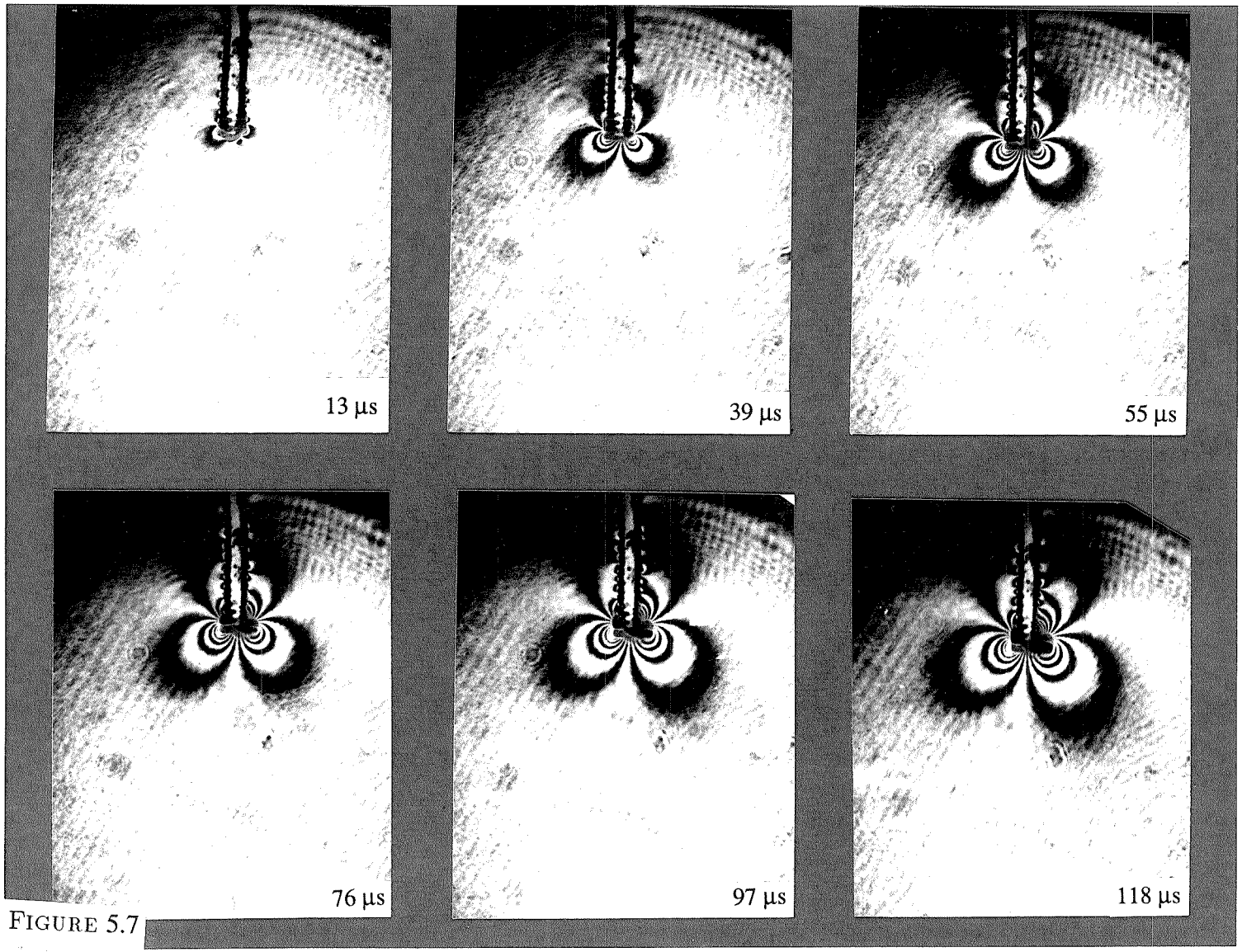

FIGURE 5.7

Sequence of CGS interferograms corresponding to initial stages of the dynamic asymmetric loading of the prenotched specimen.

et al. (1988)] it is expected that within a radius equal to half the specimen thickness, mixed-mode deformation will have a strongly three-dimensional character. As a result, the fringes contained within a radius equal to half the specimen thickness, were always excluded in the analysis. Digitization was always performed outside the 3-D zone for the useable interferograms, and, consequently, the results up to 18μs ($c_d t/l = 1.2$) were rendered uninterpretable.

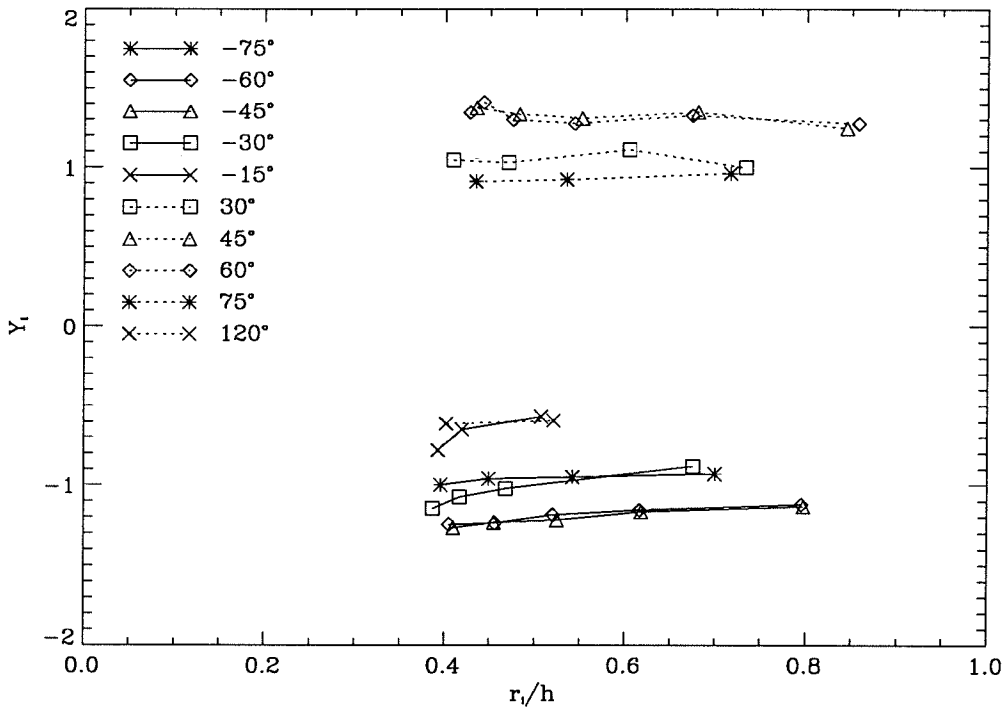

FIGURE 5.8 Radial variation of Y_i for various ϕ at a time, t=49 μs ($c_d t/l = 3.3$), after impact.

Before attempting a fit based on equation (5.13), K-dominance was investigated. The left-hand side of equation (5.12) was plotted for various values of r_i and constant ϕ. Examples of such plots are shown in Figure 5.8. It can be seen in this figure that in a substantial region surrounding the 3-D zone horizontal lines result. Thus, K-dominance is a reasonable assumption for data points taken beyond half the thickness from the notch-tip.

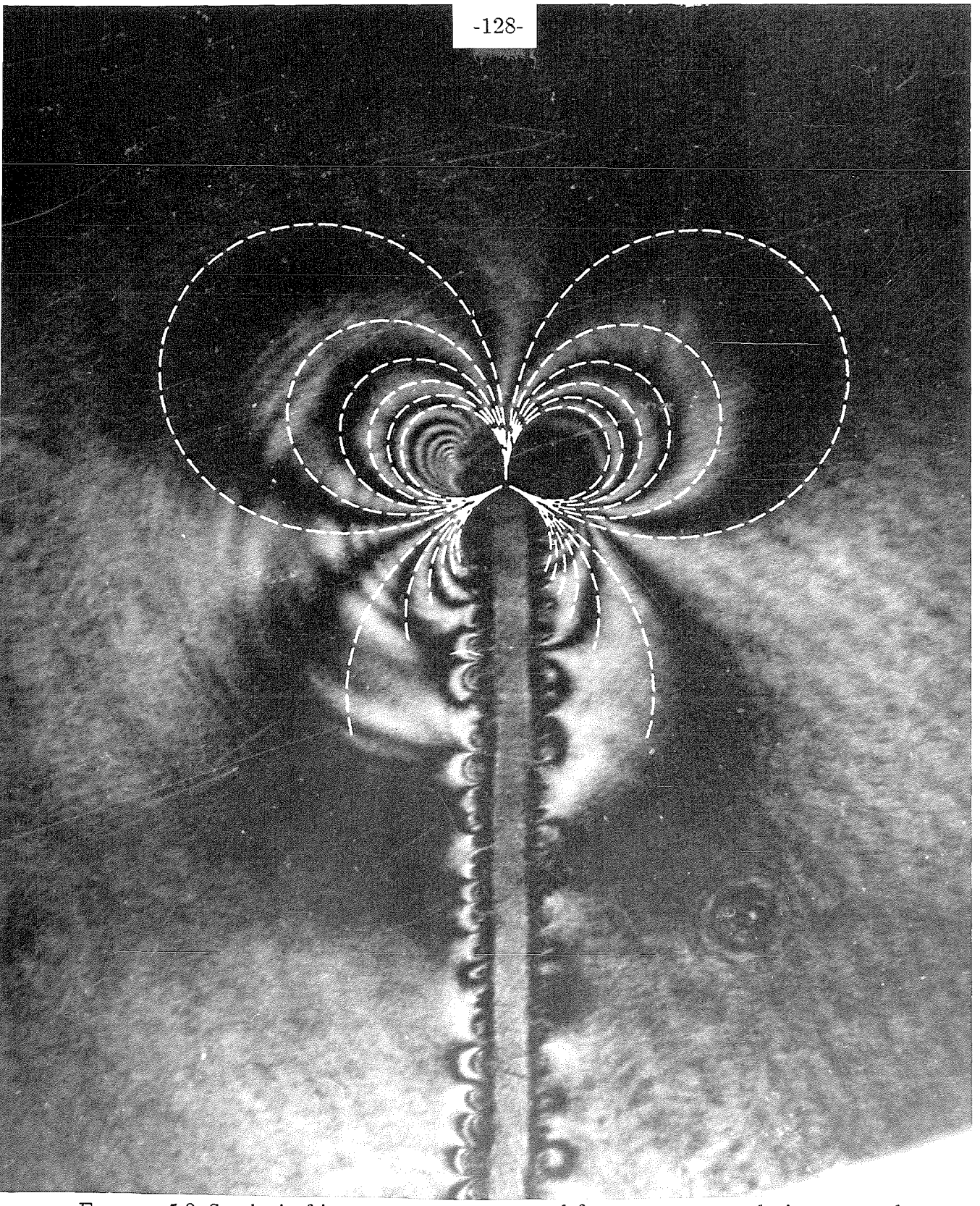

FIGURE 5.9 Synthetic fringe pattern reconstructed from one term analysis compared with experimental transmission mixed mode CGS interferogram.

Fitting of the theoretical fringes to the digitized points was carried out for a K-dominant field, and an example of such fits is shown in Figure 5.9. In this figure the theoretical fringe pattern from the fit has been superimposed on the interferogram from the experiment. It can be seen that the experimental interferogram matches the theoretical fringe pattern quite well. The resulting K values from all the fits are shown in Figure 5.10 plotted with the analysis of Lee and Freund (1990a) and the numerical calculations by Lee and Freund (1990b). Normalization of the experimental data was achieved using the plane stress values for K', see equation (5.1). As can be seen, good agreement between the experiment and the analysis is found. In Figure 5.10a the mode I experimental results follow the numerical simulation closely, but most deviate from the theoretical analysis. This is expected since the theoretical loading has an infinite area of contact while the finite element analysis models our specimen more closely. (In this experiment, the area of contact is small, 1.5 times the crack length; the finite element analysis is carried out for loading area equal to the crack length. This effect also explains the large difference between numerical and analytical predictions.) The good agreement of mode I results indicates that the method is sensitive enough to measure both K_I and K_{II} even when the ratio, K_I/K_{II} is small. In Figure 5.10b, the mode II results agree well with both the theoretical and numerical analysis.

It is noted that experimentally determining the time of impact, i.e., $c_d t/l = 0$ is difficult. Simply watching the tup impact the specimen is not sufficient because in the time between two exposures the tup moves a distance $\approx 1\mu m$. The magnification is ≈ 1; thus, detecting such small motions is impossible. However, at 5 m/s impact velocity, it is possible for the CGS to detect the initial compression wave traveling from the contact area to the crack tip, (see the interferograms in Figure 5.11) and, thus, determine the time of impact. Measurement of the velocity of this wave ($c_d = 1750$ m/s) agrees well with the expected plane stress velocity in PMMA for a dilatational

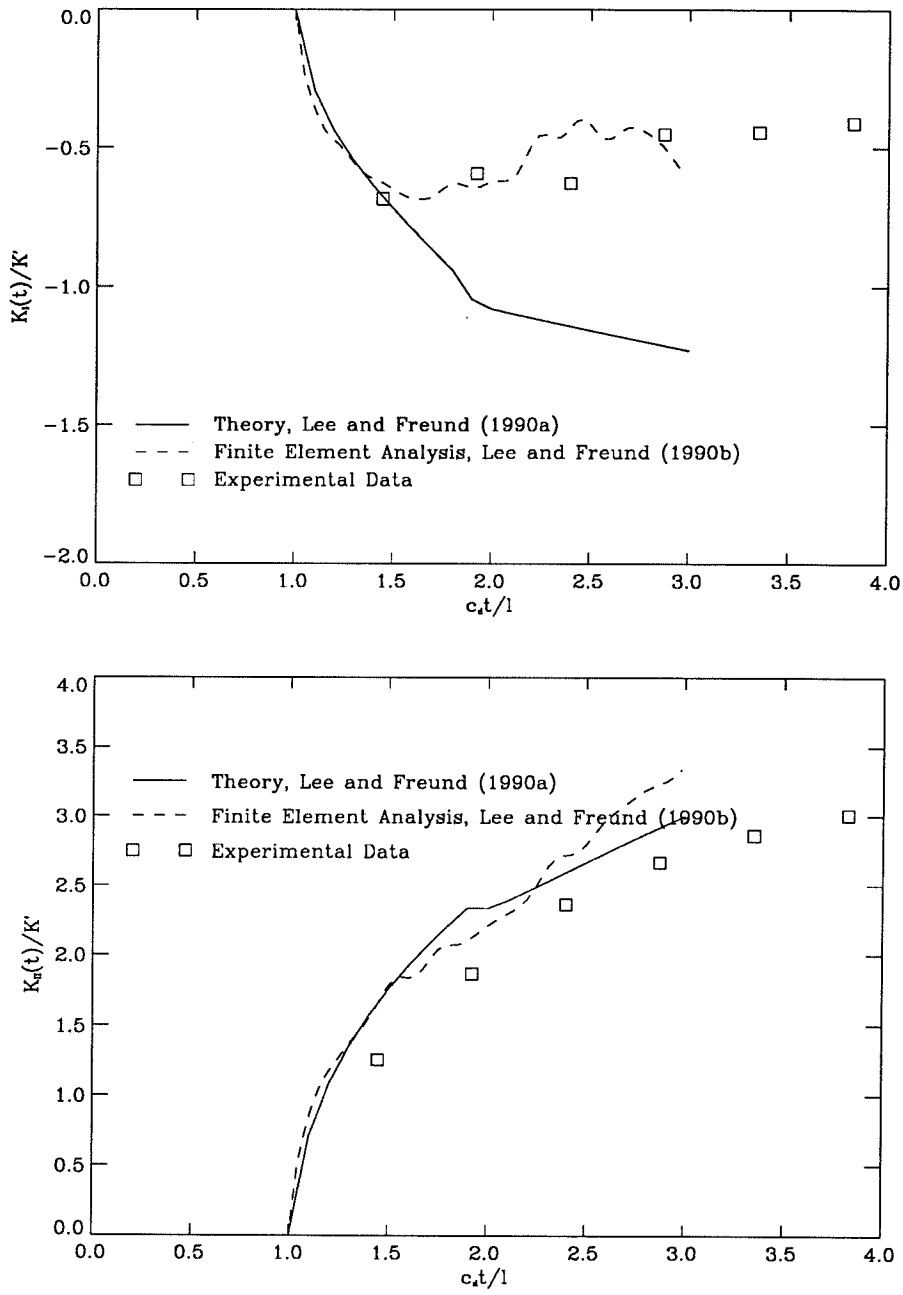

FIGURE 5.10 (a)Normalized stress intensity factor as a function of normalized time for "short" times, ($c_d t/l < 3$),. Comparison of theoretical analysis of Lee and Freund (1990a), numerical analysis of Lee and Freund (1990b) and experimental results for mode I. (a)Normalized stress intensity factor as a function of normalized time for "short" times, ($c_d t/l < 3$),. Comparison of theoretical analysis of Lee and Freund (1990a), numerical analysis of Lee and Freund (1990b) and experimental results for mode II.

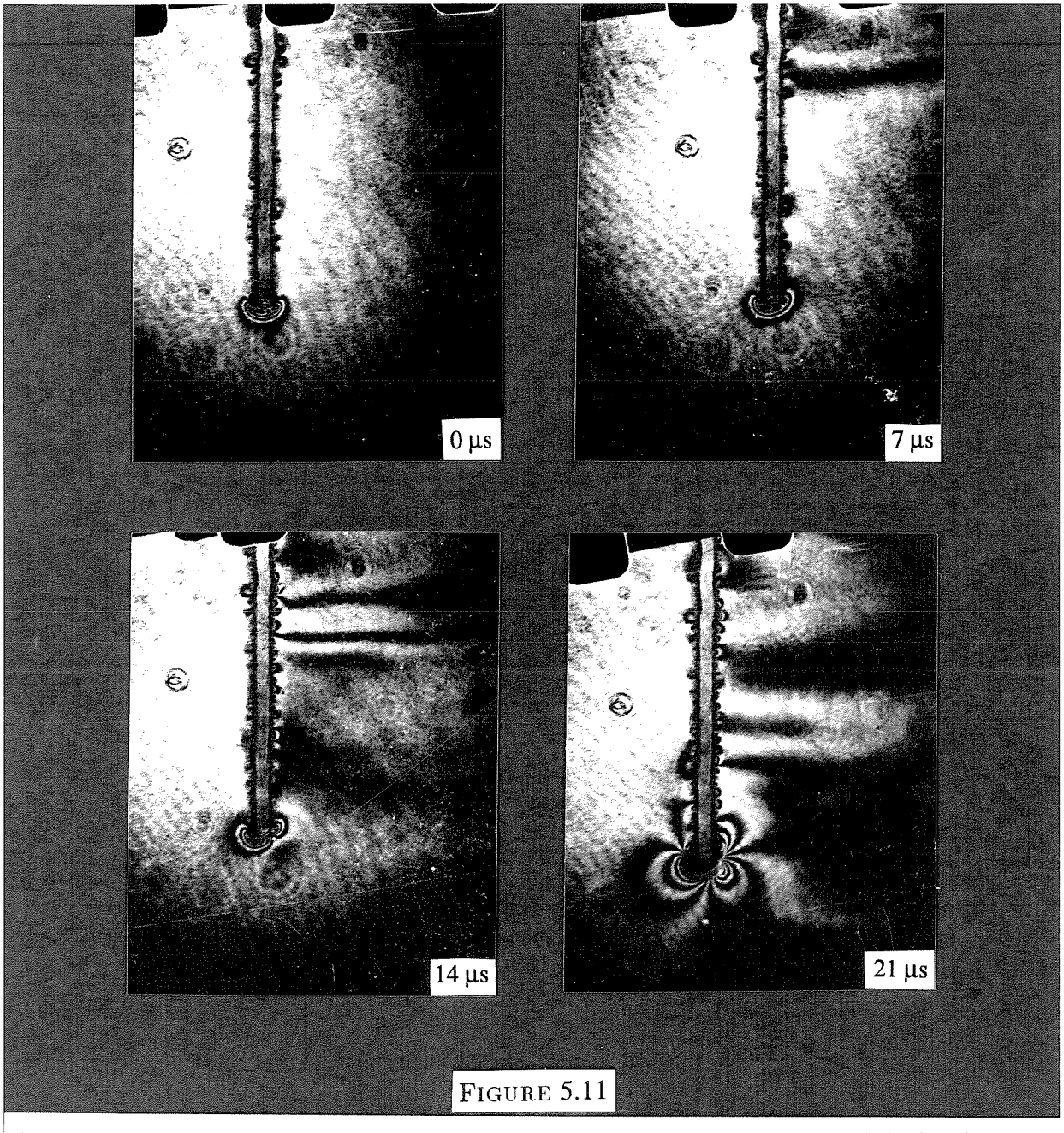

FIGURE 5.11

A sequence of high speed images showing compressive waves generated during impact

wave. By extrapolating the wave propagation back to the contact area, the time of impact was found satisfactorily.

In the CGS interferograms at later times, Figure 5.12, it can be qualitatively seen that a shift from primarily mode II in Figure 5.7 to primarily mode I deformation occurs. The fit of K-dominant fringes in this time domain gives the results shown in Figure 5.13. The time of the initiation of a mode change, the time when K_{II} reaches a maximum, coincides with the arrival time of the reflected dilatational wave from the opposite side of the specimen, $c_d t/l \approx 9$.

In conclusion, the ability of CGS to measure mixed-mode stress intensity factors under dynamic conditions has been examined. The good agreement between experimental results and theory demonstrates that even when mode-mixity is not substantial, the method produces acceptable values for both stress intensity factors. A shift of dominant deformation mode from mode II to mode I is observed over $300\mu s$ for this loading and specimen geometry. This fact is important in experiments using this configuration. Depending upon the time of initiation and, as a result, the mode-mixity, crack propagation can occur in many different directions.

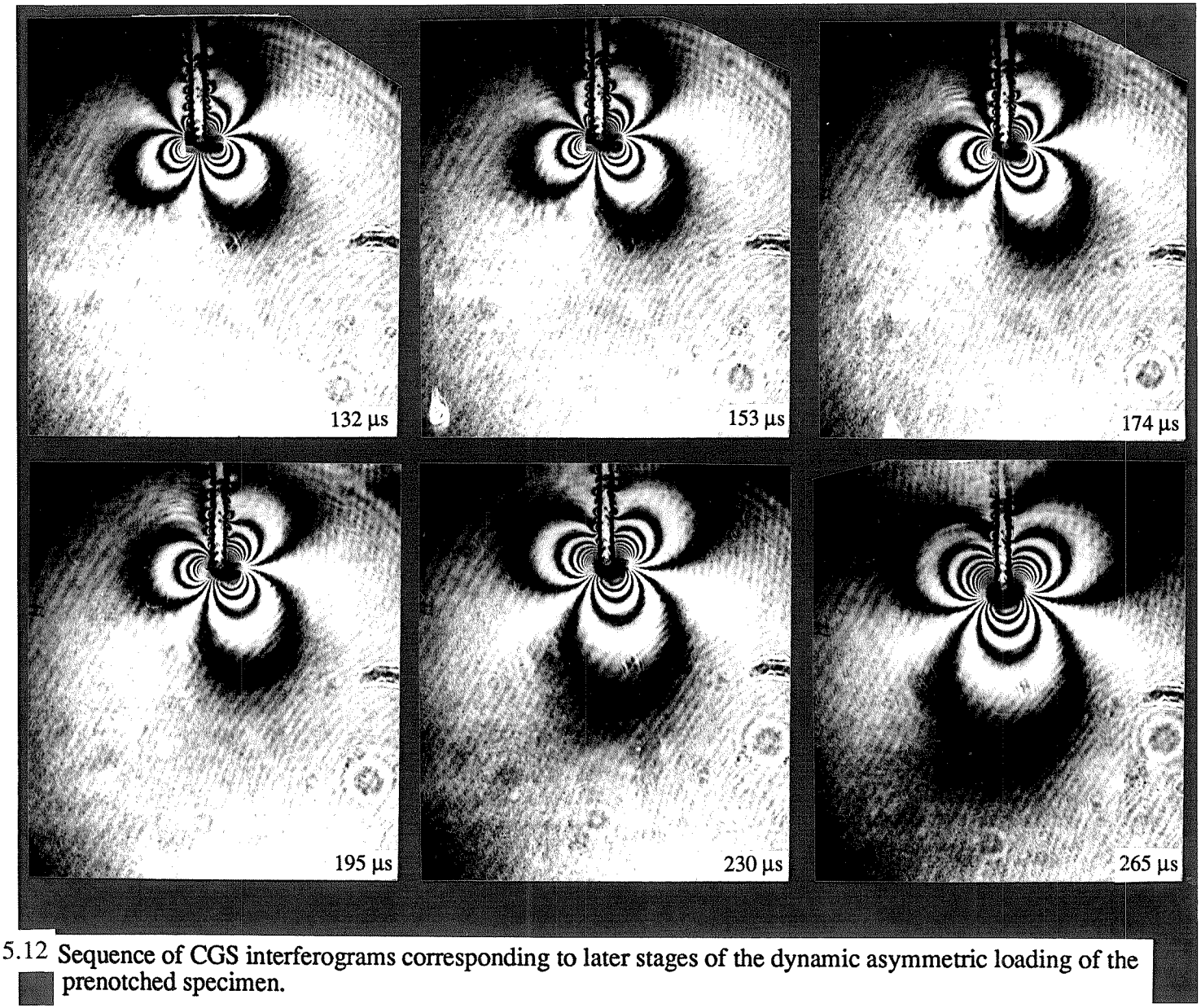

FIGURE 5.12 Sequence of CGS interferograms corresponding to later stages of the dynamic asymmetric loading of the prenotched specimen.

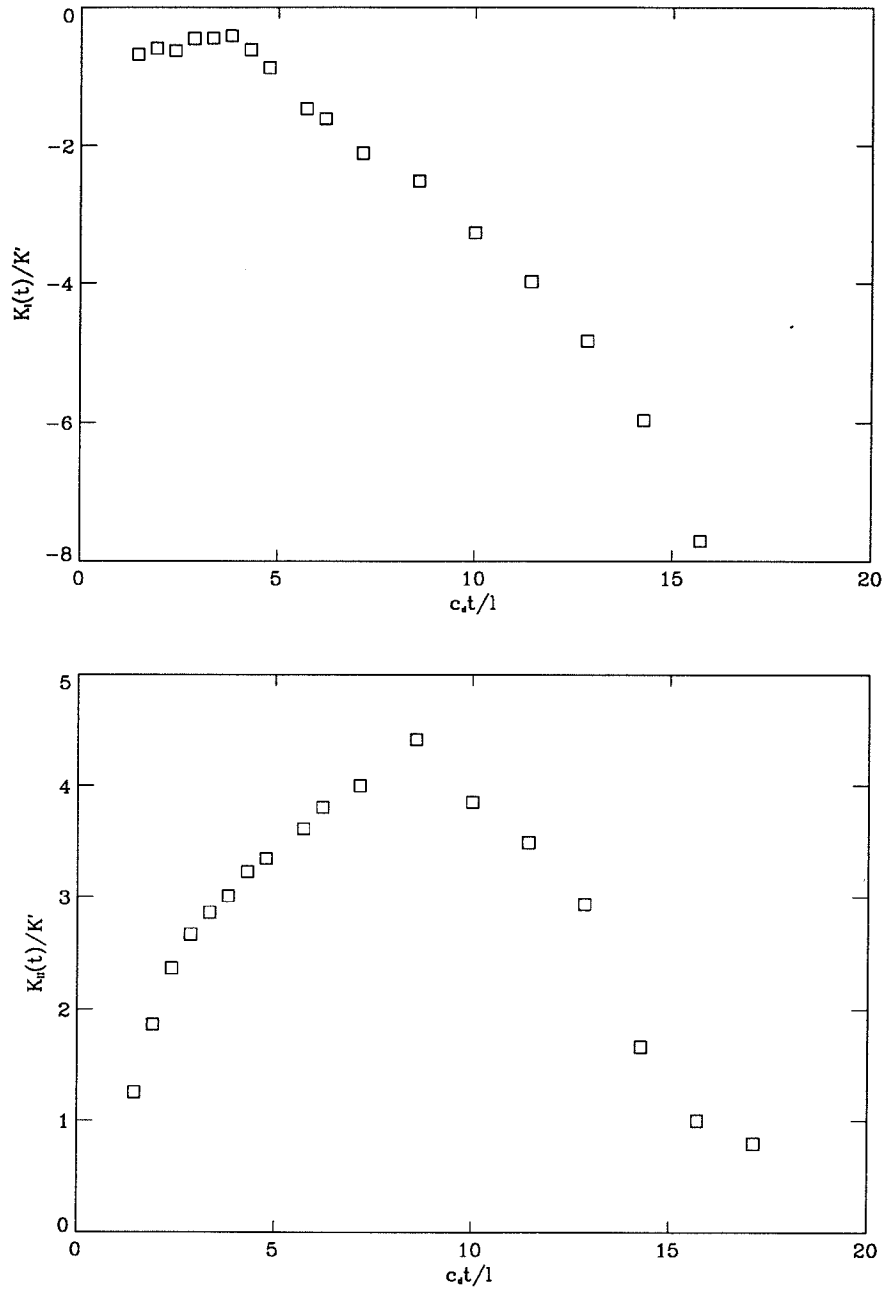

FIGURE 5.13 (a)Normalized stress intensity factors as a function of "long" times, ($c_d t/l > 3$), for mode I.(b)Normalized stress intensity factors as a function of "long" times, ($c_d t/l > 3$), for mode II.

References

1. J. Beinert and J.F. Kalthoff (1981), Experimental determination of dynamic stress intensity factors by shadow patterns, in: G. Sih, ed., *Mechanics of Fracture*, Vol. VII, Sijhoff and Noordhoff, 281

2. C.P. Burger (1987), Photoelasticity, in: A.S Kobayashi, ed., *Handbook on Experimental Mechanics,* Prentice-Hall, Inc., Ch. 5

3. J.W. Dally (1979), Dynamic photoelastic studies of fracture, *Exp. Mech.,* **19**, 349

4. F. Erdogan and G.C. Sih (1963), On the crack extension in plates under plane loading and transverse shear, *J. Basic Engineering,* **85**, 519

5. P. Hariharan, W. H. Steel and J.C. Wyant (1974), Double grating interferometer with variable lateral shear, *Optics Communications,* **11**, no. 3, 317

6. P. Hariharan and Z. S. Hegedus (1975), Double grating interferometers II. Application to collimated beams, *Optics Communications* **14**, no 1, 148

7. J.F. Kalthoff (1987a), Shadow optical analysis of dynamic shear fracture, in: *SPIE Vol. 814 Photomechanics and Speckle Metrology,* 531

8. J.F. Kalthoff (1987b), Shadow optical method of optics, in: A.S Kobayashi, ed., *Handbook on Experimental Mechanics,* Prentice-Hall, Inc., Ch. 9

9. J.F. Kalthoff and S. Winkler (1987), Failure mode transition at high rates of shear loading, in: C.Y. Chiem, H.-D. Kunze and L.W. Meyer, eds., *Impact Loading and Dynamic Behaviour of Materials,* Verlag, Vol. 1, 185

10. S. Krishnaswamy, A.J. Rosakis and G. Ravichandran (1988), On the extent of dominance of asymptotic elastodynamic crack-tip fields 2. Numerical investigation of 3-dimensional and transient effects, Caltech Report SM88-21, (*J. Appl. Mech.,* **58**, 95)

11. Y.J. Lee and L.B. Freund (1990a), Fracture initiation due to asymmetric impact loading of an edge cracked plate, *J. Applied Mechanics,* **57**, 104

12. Y.J. Lee and L.B. Freund (1990b), Private Communication

13. M.V.R.K. Murty (1978), Lateral shearing interferometers, in: D. Malacara, ed., *Optical Shop Testing,* J. Wiley & Sons, Ch. 4.

14. K. Ravi-Chandar and W.G. Knauss (1984), An experimental investigation into dynamic fracture: I. Crack initiation and arrest, *Int. J. Fracture,* **35**, 247

15. A.J. Rosakis and K. Ravi-Chandar (1986), On crack-tip stress state: an experimental evaluation of three-dimensional effects, *Int. J. Solids & Structures,* **22**, 121

16. A.J. Rosakis and A.T. Zehnder (1985), On the method of caustics: exact analysis based on geometrical optics, *J. Elasticity,* **15,** 347

17. P.S. Theocaris and E. Gdoutos (1972), An optical method for determining opening mode and edge sliding mode stress intensity factors, *J. Applied Mechanics* **39,** 91

18. H.V. Tippur, S. Krishnaswamy and A.J. Rosakis (1989a), A coherent gradient sensor for crack tip deformation measurements: analysis and experimental results, Caltech SM-Report 89-1, (*Int. J. Fracture,* **48,** 193)

19. H.V. Tippur, S. Krishnaswamy and A.J. Rosakis (1989b), Optical mapping of crack tip deformations using the methods of transmission and reflection coherent gradient sensing: a study of crack tip K-dominance, Caltech Report SM89-11, (*Int. J. Fracture,* **52,** 91).

CHAPTER 6

Full Field Measurements of the Dynamic Deformation Field Around a Growing Adiabatic Shear Band at the Tip of a Dynamically Loaded Crack or Notch

Overview

The method of Coherent Gradient Sensing (CGS) is used to record the deformation field around an adiabatic shear band emanating from a pre-crack or pre-notch tip in C-300 steel loaded dynamically in mode-II. At early times after impact, the resulting fringe pattern is seen to exhibit the characteristics of a mode-II Dugdale crack under small scale yielding conditions, and, as a result, the experimental fringe patterns are fitted to the theoretical Dugdale crack deformation field by using a least squares fitting scheme. In the fitting procedure it is assumed that the time history of $K_{II}^{d}(t)$, the dynamic mode-II stress intensity factor, follows the analysis of Lee and Freund (1990). This results in values for the shear band length and the average shear stress acting on the shear band as functions of time. The shear band is observed to initiate when $K_{II}^{d}(t)= 140\ MPa\sqrt{m}$ and subsequently propagate with an average speed of 320 m/s. The shear stress on the shear band decreases from 1.6 GPA at initiation to 1.3 GPa during this propagation. Shear band arrest is not recorded for the given experiment.

6.1 Introduction

The formation of adiabatic shear bands has recently received renewed attention following the experimental measurements of the temperature rise in adiabatic shear bands by Duffy (1984). In the past ten years these measurements have helped motivate a considerable amount of modelling of adiabatic shear band growth which has recently appeared in the open literature. Without presenting an extensive review, it is helpful to recall some of the salient and common features of the many models that have been made available.

Commonly, the formation or growth of an adiabatic shear band is modelled as the competition between thermal softening and strain and/or strain-rate hardening of a material under shear loading. Usually an approximate model of thermal softening is added to the constitutive equation for a material, the temperature is treated as an additional unknown and the heat conduction equation is added to the field equations. Invariably, the heat conduction equation contains a term that links plastic deformation of the material to the production of heat (see Chapter 4), and a temperature rise in the material is predicted for the deformation. The net effect of the assumptions of the model is the introduction of a mathematical mechanism by which instabilities in the deformation can be formed. When thermal softening is greater than strain and/or strain-rate hardening, the material deforms, heats and becomes softer. Then, further deformation occurs due to the lower strength generating more heat which in turn softens the material more producing a "self-feeding" mechanism by which an instability is formed. The purpose of this work is to examine the deformation field around an adiabatic shear band as it forms and, hopefully, extract more information about the shear band formation process itself.

Kalthoff (1987) and Kalthoff and Winkler (1987) have observed the formation of adiabatic shear bands at the tip of dynamically loaded, stationary, pre-manufactured

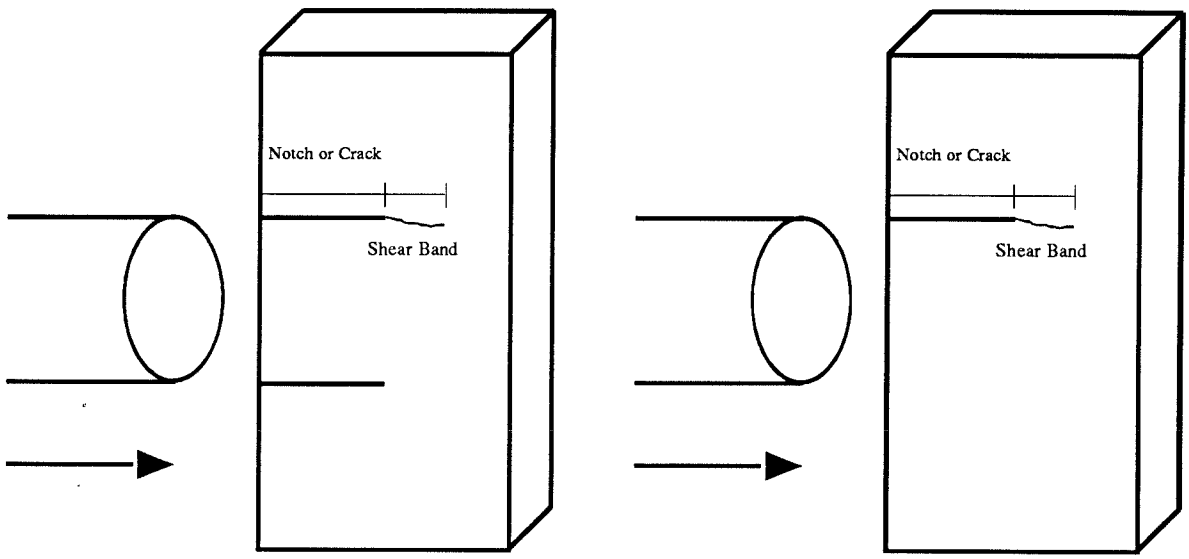

FIGURE 6.1 (a) The loading geometry observed by Kalthoff (1987) and Kalthoff and Winkler (1987) to generate shear bands in C-300 steel at a pre-notch or pre-crack tip. (b) The modified pre-notched geometry used in the present investigation.

notches in plates made of C-300 steel. The pre-manufactured notches are loaded dynamically in nearly pure mode-II loading conditions by an asymmetric impact in the area between the two pre-notches on the edge of the plate. See Figure 6.1(a). When sufficient impact velocity is used, an adiabatic shear band is formed directly ahead of

the pre-notch as shown schematically in the figure. In the work described here, a similar configuration is used. This configuration involves the dynamic asymmetric loading of only *one* pre-notch and is schematically shown in Figure 6.1(b). The use of only one pre-notch provides a simple loading geometry by which one may observe the formation of adiabatic shear bands.

The method of Coherent Gradient Sensing (CGS) [Tippur et al. (1989a) and (1989b) and Rosakis (1993)] is used here in reflection on pre-notched steel plates loaded dynamically in mode-II as described above. It is important to note that CGS has never before been used in a reflection arrangement to study deformations such as these. However, it has been used successfully in *transmission* for the study of dynamic crack growth [Tippur et al. (1989a) and (1989b)] and for the study of the given loading geometry [Chapter 5].

It is proposed here that the shear band formation at a dynamically loaded mode-II pre-notch may be modelled by the Dugdale strip yield model. In such a model the shear band is assumed to be a one-dimensional line of yielded material extending directly ahead of the stationary pre-notch or pre-crack with a uniform shear stress acting upon it. Implicit in this approach to modelling are a number of assumptions about the mechanisms of the nucleation and growth of adiabatic shear bands. For example, the following assumptions are made; the width of the shear band is assumed negligible, the shear band is assumed to grow straight ahead of the pre-notch or pre-crack, the shear stress is not allowed to vary over the length of the shear band, the effects of inertia are neglected, and the length of the shear band is determined by the far field $K_{II}^{d}(t)$ that is acting on the pre-notch (small scale yielding is implied and the magnitude of the shear stress on the yielded zone is chosen to nullify the highest order stress singularity at the shear band tip).

The last of these assumptions is perhaps the most restrictive, however it is useful

because it gives a relation between the stress intensity factor, the shear stress on the yield zone and the length of the yield zone. In addition it is also motivated by numerical investigations of dynamic shear band growth [Lee (1990)] where no singularity is found to exist at the growing shear band tip. For a pure $K_{II}^{d}(t)$ field with a Dugdale zone having a uniform shear stress, $\tau_0(t)$, acting on it, the length of the yield zone, $R(t)$, is given by Rice (1968)

$$R(t) = \frac{\pi}{8}\left(\frac{K_{II}(t)}{\tau_0(t)}\right). \tag{6.1}$$

Although the assumptions and approximations of the model are somewhat limiting, the model is used here as a first attempt at analyzing the results, and it should be emphasized that the quantitative conclusions are reported as *first estimates* .

6.2 Experimental Procedure

6.2.1 The Method of CGS

The coherent gradient sensor may be used both in a transmission configuration for transparent materials or in a reflection configuration for opaque materials. The basic governing equation for the formation of fringes is the same either each case. In Chapter 5 the following governing equation for fringe formation, Eq (5.5), was derived;

$$\frac{\partial(\delta S(x_1, x_2))}{\partial x_\alpha} = \frac{mp}{\Delta}.$$

For an opaque material reflecting the incident laser light, the phase difference, $\delta S(x_1, x_2)$, in equation (5.5), is given by the difference in optical path length. This change is wholly attributed to changes in specimen thickness due to Poisson's contraction, and, thus, the optical path difference is given by [Tippur et al. (1989a) and

(1989b) and Rosakis (1993)]

$$\begin{aligned}\delta S(x_1,x_2) &= 2h\int_0^{\frac{1}{2}} \epsilon_{33} d\left(\frac{x_3}{h}\right) \\ &= 2h\int_0^{\frac{1}{2}} \left\{(\sigma_{11}+\sigma_{22})\left[1-\frac{\sigma_{33}}{\nu(\sigma_{11}+\sigma_{22})}\right]\right\} d\left(\frac{x_3}{h}\right)\end{aligned} \tag{6.2}$$

where h is the thickness and the factor of 2 accounts for the light travelling the surface displacement twice, once on the way in and once on the way out. The integral represents the optical path difference due to changes in the plate thickness caused by the strain component, ϵ_{33}.

Assuming the material is isotropic and linearly elastic and using the plane stress assumption, Eq (6.2) may be integrated giving the following result;

$$u_3 = -\frac{\nu h}{2E}(\hat{\sigma}_{11}+\hat{\sigma}_{22}) \tag{6.3}$$

where the term in brackets in Eq (6.2) has been neglected for plane stress conditions and $\hat{\sigma}_{11}$ and $\hat{\sigma}_{22}$ are plane stress thickness averages of stress components in the material while $\hat{\sigma}_{33}=0$. Hence, inserting Eq (6.3) into Eq (6.2) gives

$$\delta S(x_1,x_2) \approx 2u_3 = -\frac{\nu h}{E}(\hat{\sigma}_{11}+\hat{\sigma}_{22})\,. \tag{6.4}$$

Finally, substituting (6.4) into (5.5) gives the result,

$$2\frac{\partial u_3}{\partial x_\alpha} = -\frac{\nu h}{E}\frac{\partial(\hat{\sigma}_{11}+\hat{\sigma}_{22})}{\partial x_\alpha} \approx \frac{mp}{\Delta}. \tag{6.5}$$

All interference images produced by the CGS apparatus in this work are interpreted using equation (6.5). Notice that a rigid body rotation does not effect the results since the derivative of u_3 of such a motion results in a constant that has no effect upon fringe pattern formation. The method of using an incident beam at a small angle to the undeformed-surface normal is made possible by this result. Angling the incident illumination is identical to a rigid body rotation. This fact precludes the need for a beam splitter in the set-up of CGS for use in reflection on opaque materials. In the experiments reported here the specimens were illuminated at a small angle to the undeformed-surface normal.

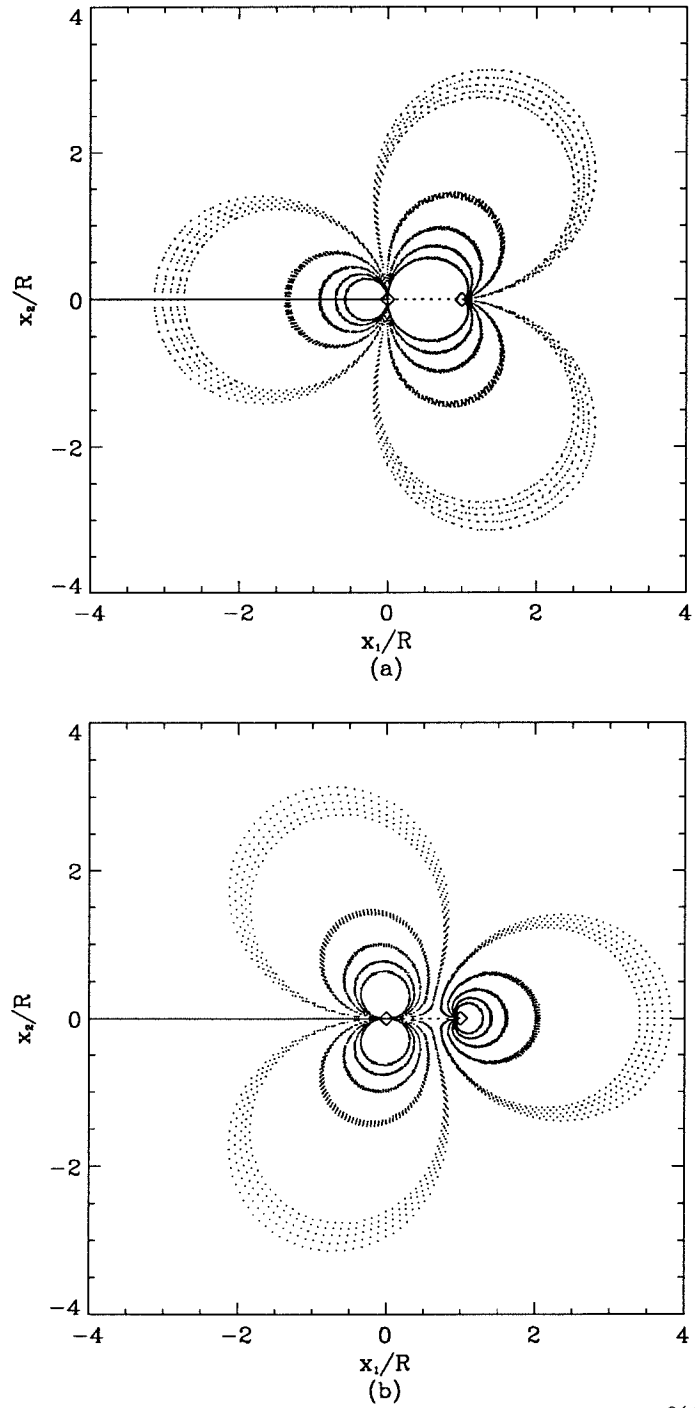

FIGURE 6.2 (a) Numerical predictions of CGS fringes (constant $\frac{\partial(\hat{\sigma}_{11}+\hat{\sigma}_{22})}{\partial x_1}$ values) constructed on the basis of a pure K_{II}^{d} field with a Dugdale shear zone of length R ahead of the pre-crack tip. (b) Predictions of CGS fringes for constant $\frac{\partial(\hat{\sigma}_{11}+\hat{\sigma}_{22})}{\partial x_2}$ values and the same assumptions as (a).

For the case of a semi-infinite Mode-II Dugdale crack with a yield zone of length $R(t)$ the solution for the elastic stresses around the yield zone may be found [Rice (1968)],

$$\hat{\sigma}_{11}(t)+\hat{\sigma}_{22}(t)=\frac{4\tau_0(t)}{\pi}\mathrm{Im}\left[\tan^{-1}\left(\sqrt{\frac{R(t)}{z-R(t)}}\right)\right] \tag{6.6}$$

where $\tau_0(t)$ is the shear stress on the yield zone and $z=x_1+ix_2$ is a complex number. Taking the derivative of this function gives

$$\begin{aligned}\frac{\partial\{\hat{\sigma}_{11}(t)+\hat{\sigma}_{22}(t)\}}{\partial x_1}&=-\frac{2\tau_0(t)}{\pi}\mathrm{Im}\left[\frac{1}{z}\sqrt{\frac{R(t)}{z-R(t)}}\right],\\ \frac{\partial\{\hat{\sigma}_{11}(t)+\hat{\sigma}_{22}(t)\}}{\partial x_2}&=-\frac{2\tau_0(t)}{\pi}\mathrm{Re}\left[\frac{1}{z}\sqrt{\frac{R(t)}{z-R(t)}}\right].\end{aligned} \tag{6.7}$$

Inserting this result in the governing equation for the CGS apparatus, Eq (6.5), results in an equation for the formation of fringes around a semi-infinite Mode-II Dugdale crack. This equation has been solved here numerically for partial differentiation in both directions, x_1 or x_2, and the results may be seen in Figure 6.2. For very large distances (when compared to the Dugdale zone size) away from the pre-crack tip the fringe pattern resembles the pattern for a pure mode-II K dominant field. (See the fringe patterns in Chapter 5 and Mason et al., 1992.) Also, when partial differentiation with respect to x_1 is performed the fringe pattern gives a clear indication of the location of both the original pre-crack tip and the tip of the Dugdale zone. For this reason all experiments reported here are performed with differentiation parallel to the pre-crack tip, i.e., differentiation with respect to x_1. And quick estimates of the Dugdale zone size are made by measuring the distance between the point where the rear lobe converges to the x_1 axis and the point where the front lobes converge to the x_1 axis.

6.2.2 Apparatus

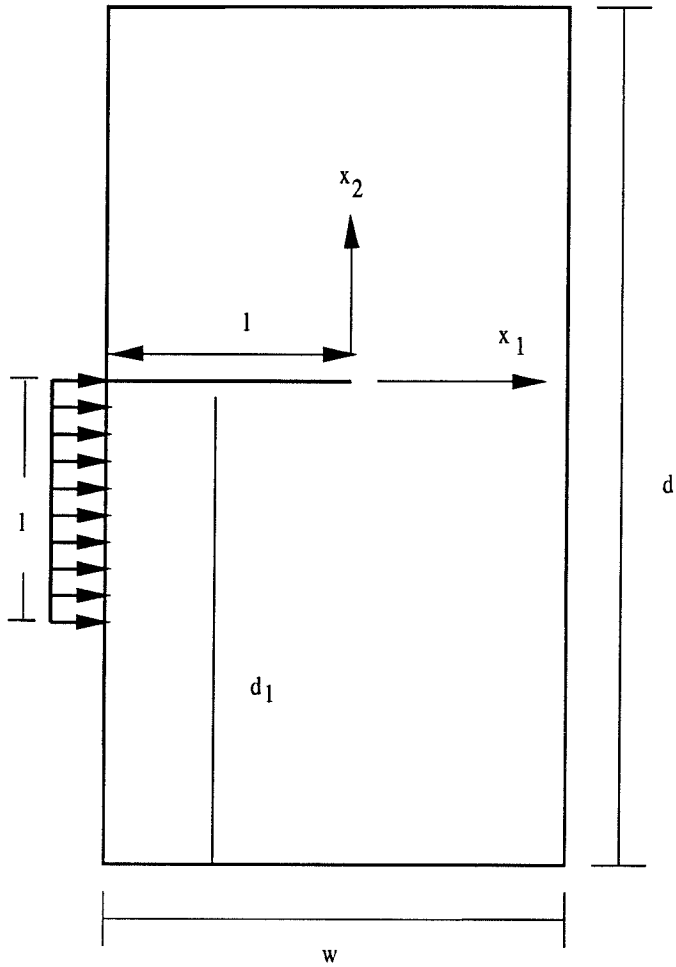

Dimensions of specimen:
l=50 mm
w=100 mm
d=200 mm
d_1=113 mm
thickness=6 mm

Mechanical Properties of specimen:
E=200 GPa
v=.3
c_d^{pl-o}=5430 m/s

FIGURE 6.3 Specimen geometry, loading configuration and material constants.

The exact specimen geometry is shown in Figure 6.3. Specimens are made of C-300 maraging steel in the peak aged condition. Impact of the specimens is achieved using an air gun and a 75 mm long, 50 mm diameter projectile made of C-350 maraging steel in the peak aged condition. Two types of test were performed; first, round tip pre-notches $\approx .5mm$ thick machined by wire EDM as per the figure were impact loaded, and, second, pre-cracks approximately 10 mm in length grown at the tip of a 50 mm long, .5 mm thick pre-notch by loading the specimen in dynamic shear were impact loaded.

Set up of the CGS apparatus follows Figure 5.4. A high-speed framing camera manufactured by Cordin Co., Salt Lake City, UT, is used as the imaging system. The CGS interferograms are generated using an Argon-Ion laser synchronized with the high-speed camera and pulsed for 50 ns at 1.4 μs intervals as the light source. The total length of the record of the event is $\approx$ 110 μs resulting in approximately 80 CGS interferograms per test.

The fringe patterns are digitized by hand. A ray of constant angle ϕ from the x_1 axis is followed; points at the center of fringes are digitized along the way. The effective crack tip was chosen by estimating the point where the rear lobe converged to the x_1 axis. See Figure 6.2(a). Most of the uncertainty in digitization arises from locating the effective crack tip and choosing the center of the fringe.

6.2.3 Data Reduction

Deviation of experimental results from the fringe patterns predicted by a mode-II Dugdale crack field are expected for many reasons. These include the existence of a zone around the pre-notch tip where plane stress assumptions break down (the 3-D zone) [Rosakis and Ravi-Chandar (1986) and Krishnaswamy et al. (1988)], the interference of propagating waves from the loading with the crack tip field and violation of the assumptions used in the derivation of the Mode-II Dugdale model. Consequently, the

results are analyzed by *fitting* the Dugdale crack solution to the digitized fringes of the experiment by a least squares fitting scheme. Digitization is carried out only on the points above the pre-crack line (impact occurs on the side of the specimen *below* the pre-crack line) in order to avoid confusion caused by the interaction between the Dugdale zone pattern and the pattern generated by the propagating waves. The fit is produced by minimizing the error function

$$\chi(\tau_0, R) = \sum_{i=1}^{N} (m_i - f(r_i, \theta_i))^2 , \tag{6.8}$$

where

$$f(r_i, \theta_i) = -\frac{\Delta}{p}\frac{\nu h}{E}\frac{\partial(\hat{\sigma}_{11} + \hat{\sigma}_{22})}{\partial x_\alpha} \tag{6.8a}$$

and

$$\begin{aligned} r_i &= \sqrt{x_1^2 + x_2^2} \\ \theta_i &= \tan^{-1}\left(\frac{x_2}{x_1}\right) \end{aligned} . \tag{6.8b}$$

The expression for the partial derivative in Eq (6.8) is given by Eq (6.7), and N is the total number of points. The minimization of equation (6.8) was performed numerically. First, the dynamic stress intensity factor was taken from the solution of Lee and Freund (1990). When the solution of Lee and Freund (1990) is no longer applicable, at longer times, a fit of the results in Chapter 5 for long times is used. This is justified by the agreement between the model and the experimentally measured $K_{II}^{d}(t)$ for PMMA loaded under the same conditions as demonstrated in Chapter 5. Then the function χ was minimized numerically with respect to the shear stress $\tau_0(t)$ while holding the stress intensity factor constant.

6.3 Results and Discussion

As a first investigation of the shear band formation, lines were etched on the steel, and it was impacted at 40 m/s. The resulting deformation can be seen in Figure 6.4.

The shear band zone width is small, 200 μm, and the average shear strain in the band is roughly 100%. This result is repeatable, so the numbers quoted here represent the shear bands formed in each of the series of photographs to follow. Note that the deformation is mostly elastic outside the shear band and that the etched lines above and below the shear band are still aligned as they were before the deformation. This fact indicates that during the shear band formation the lower, impacted plane of material is compressed elastically moving the lower half of the etched lines to the right while the upper plane of material remains approximately stationary with the shear band absorbing the resultant mismatch deformation. After a crack forms along the shear band elastic unloading occurs allowing the lines to realign. This observation justifies the use of an elastic constitutive equation in the Dugdale crack model to predict the material deformation around the forming adiabatic shear band in future experiments.

The recorded fringe patterns for a dynamically loaded pre-notch may be seen in Figure 6.5 where zero time, $t = 0$, is taken as the time of impact on the plate edge. Waves generated at impact take approximately 10 μs to reach the pre-notch tip and begin loading. The fringe pattern has a dark line down the middle which is a remnant of the camera. This line of light is removed from the image by the camera and recorded elsewhere in order to provide a means of double-checking the pulsing rate and correctly recording the time of exposure. In general the result has several shortcomings. First, it is noted that the deformation field does not resemble the Dugdale zone or the K_{II} dominant zone in any way at the times of interest. Although the deformation is elastic around the adiabatic shear zone, there is considerable interaction between the incoming waves from impact and the pre-notch tip. Second, there is a dark region below the original pre-notch where no image is formed. This is due to the limitations of the experimental apparatus. Light that is reflected from highly angled surface elements is lost because of the finite aperture size of the system. The reflected light simply never

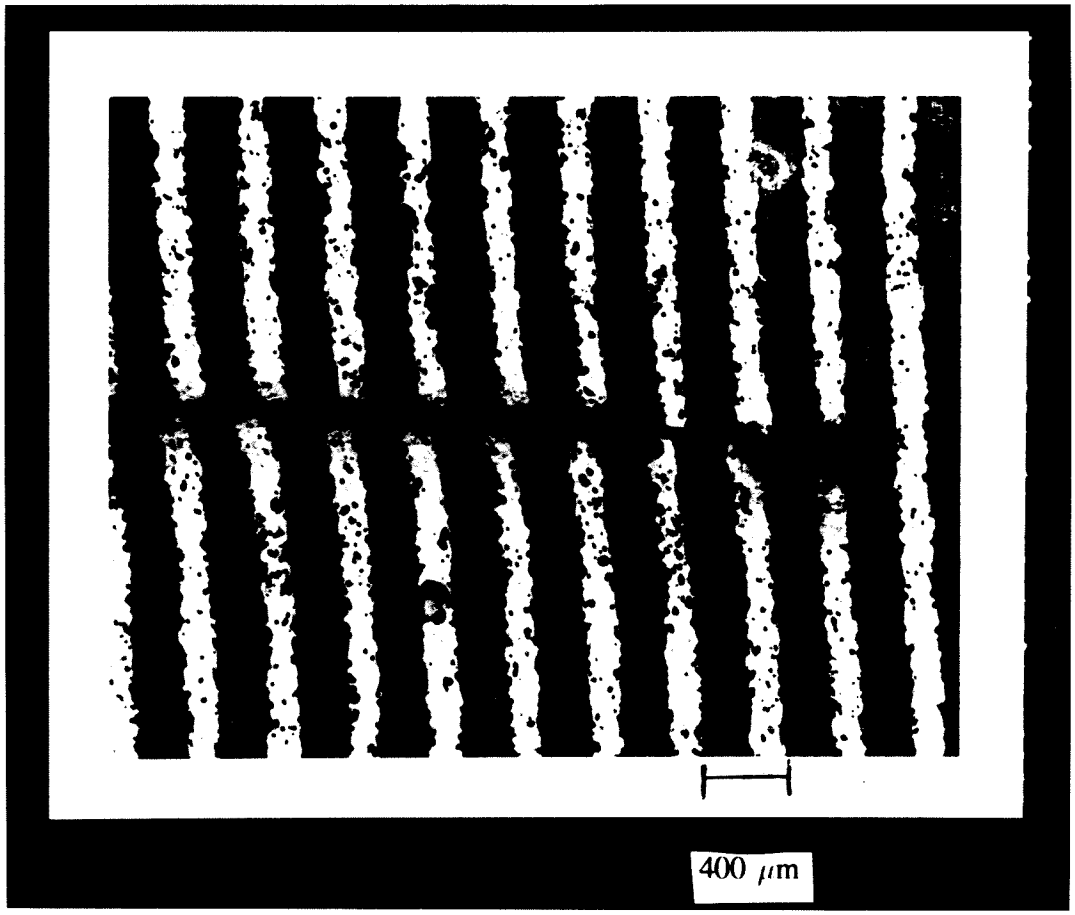

FIGURE 6.4 Example of a shear band formed by asymmetric loading of a pre-notch. The lines were etched before loading. Shear localization is observed.

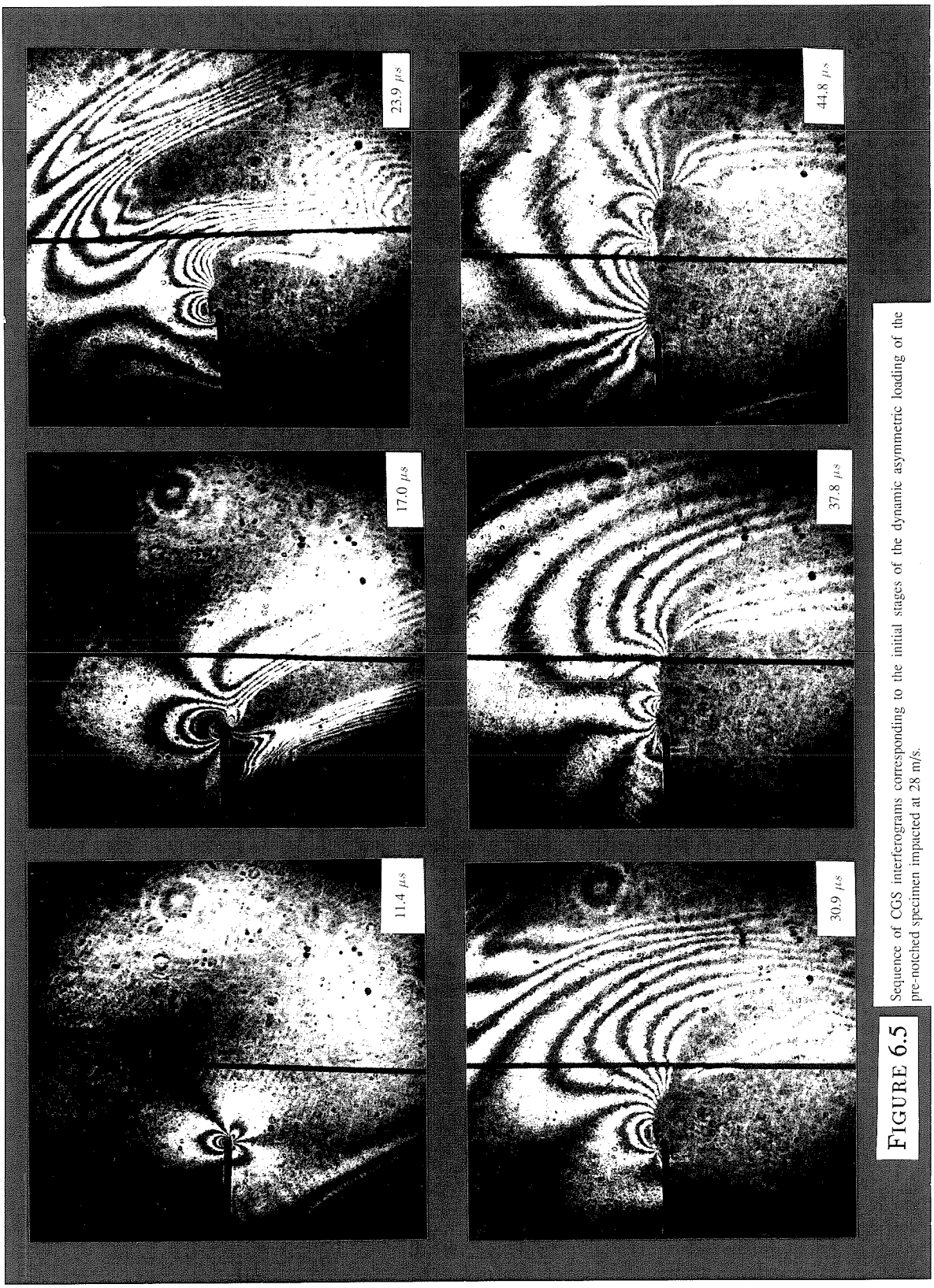

FIGURE 6.5 Sequence of CGS interferograms corresponding to the initial stages of the dynamic asymmetric loading of the pre-notched specimen impacted at 28 m/s.

intersects the focussing lens or diffraction gratings and therefore is not focussed on the film. This vignetting results in an aperture spot, a dark region on the film where no light has been focussed. The aperture spot indicates that regions of extreme out of plane deformation are located below the initial pre-notch and at the pre-notch tip. Last, note that the loading waves in this experiment are slightly askew with respect to the pre-notch faces. This effect is probably due to a mis-alignment at impact. Although, this mis-alignment appears to have little effect on the loading of the pre-notch tip; the fringes shown here are very much the same as tests that were better align at impact.

In spite of the obvious shortcoming of the test, the results have some merit because the initiation and propagation of a shear band may be seen in the figures and a change of failure propagation mode occurs at later times. A photograph of the specimen after the experiment is shown in Figure 6.6. The initial growth directly ahead of the pre-notch tip is a shear band dominated failure growth. No shear lips are observed and the fracture surface resembles that reported by Kalthoff (1987) and Kalthoff and Winkler (1987) for shear failure. This growth is observed in Figure 6.5 and, in agreement with the report of Kalthoff (1987) and Kalthoff and Winkler (1987) the growth proceeds at a small negative angle to the x_1 axis. By examining the pictures recorded at later times than those shown in Figure 6.5, it can be seen that crack/shear-band growth arrested at approximately 40 μs after impact of the specimen. This time corresponds roughly to the time required for an unloading wave from the rear of the projectile to reach the pre-notch or shear band tip. After the shear growth arrested, a different mode of crack growth at an angle to the shear growth can be seen in Figure 6.6. This growth is mode-I dominated. Shear lips are present, and the fracture surfaces resemble that reported by Kalthoff (1987) and Kalthoff and Winkler (1987) for mode-I failure. Initiation and growth of this latter crack occurs long after the recorded loading, and, unfortunately, the exact details of its formation are not known.

FIGURE 6.6 Photograph of the crack path taken after dynamic loading. The crack propagates forward parallel to the pre-notch in a shear dominated mechanism then arrests. At later times the crack propagates at an angle to the pre-notch in a locally symmetric (mode-I) mode of failure.

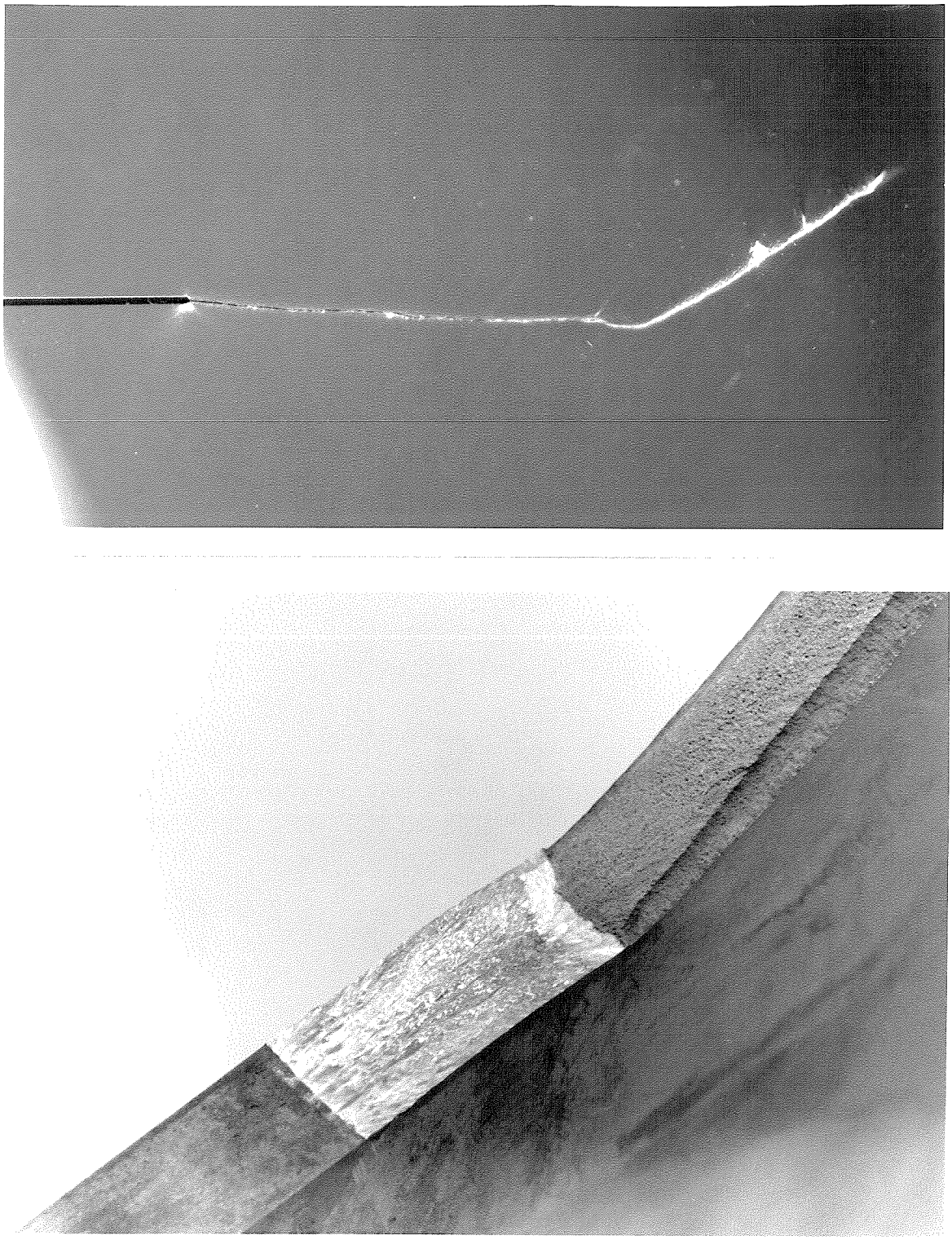

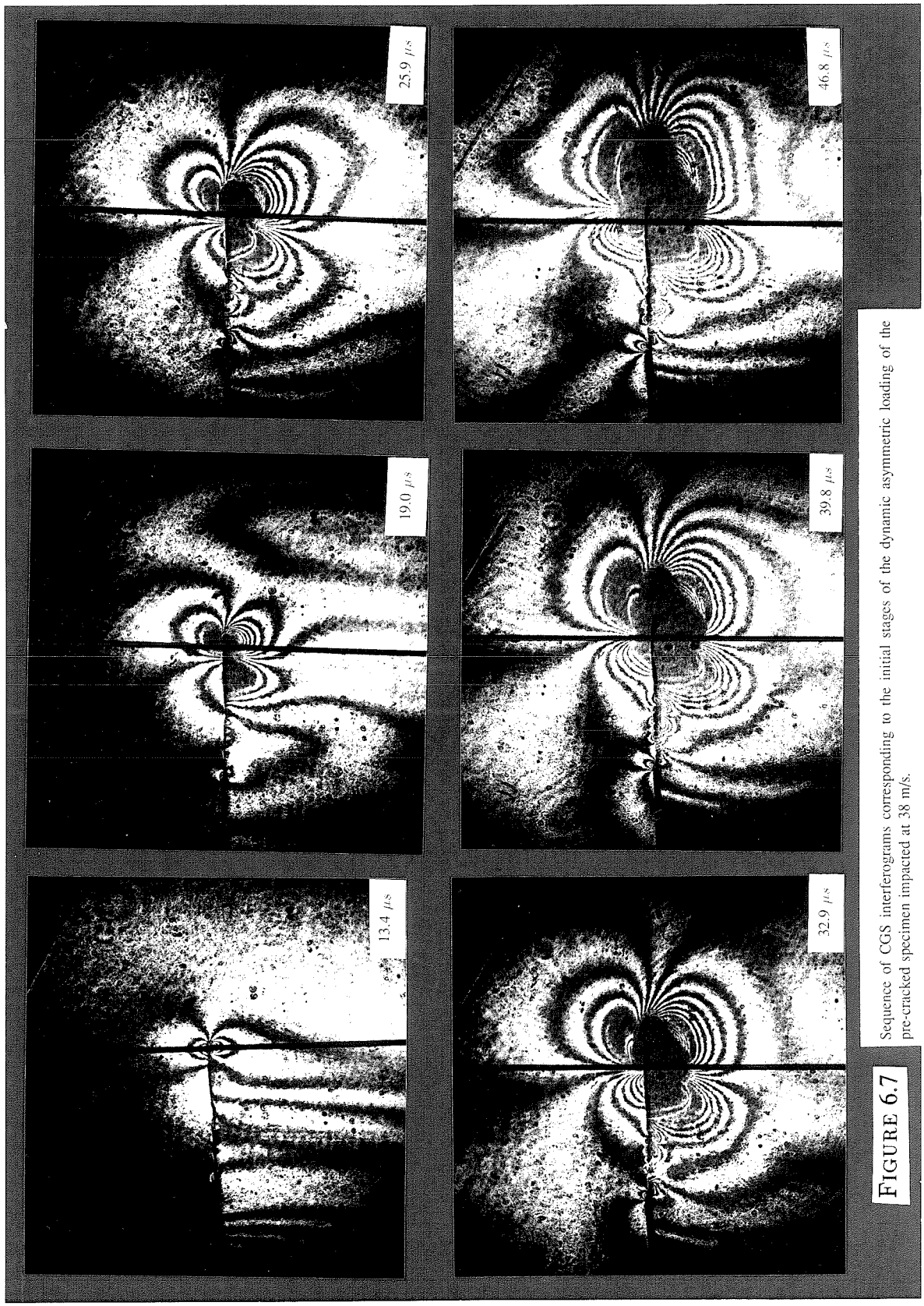

FIGURE 6.7 Sequence of CGS interferograms corresponding to the initial stages of the dynamic asymmetric loading of the pre-cracked specimen impacted at 38 m/s.

In Figure 6.7 a record of fringes may be seen for a dynamically loaded stationary *pre-crack*. The deformation has a resemblance to the theoretical fringe pattern shown in Figure 6.2(a). The "effective" crack tip and zone tip can be located by the fringe pattern in the upper half plane quite easily. However, the waves in the lower half plane considerably complicate the fringe pattern there at various times during the recorded deformation. Consequently, in order to simplify the digitization procedure, only the fringes on the upper half plane were digitized. It is felt that the upper fringes more closely resemble the small scale yielding, Dugdale pattern throughout the recorded deformation because extensive interaction of the upper fringes with the incoming stress wave is not observed. Note, however, that the fringe pattern on the upper half-plane becomes less and less similar to the Dugdale pattern as time goes on. At 47 μs deviations between the measured fringe pattern and the theoretical pattern become too large to warrant further fitting of the theoretical Dugdale deformation field to the experimentally measured deformation field. Furthermore, the aperture spot forming around the shear zone continues to grow making it more and more difficult to see the fringe pattern.

In Figure 6.7 there is an aperture spot around the Dugdale zone and crack tip at longer times. Inside this spot a very faint picture of the initial pre-crack tip may be seen. This image comes as a result of leakage laser light exposing the film before the impact and subsequent high powered laser pulsing. The exposure is easily alleviated, but in this case it proves helpful not to prevent it. It can be seen in the figure that the region of the pre-crack near the tip is curved downward. One can select a point where the downward curvature begins, somewhere near the intersection of the pre-crack and the dark stripe. See Figure 6.8. Looking at the initial photo in Figure 6.7, it can be seen that the initial fringe pattern is actually formed around the point where the pre-crack begins to curve rather than at the pre-crack tip. That is, the fringe pattern indicates

that there is an initial "effective" crack tip where the initial pre-crack begins to curve downward rather than at the location of the actual intial pre-crack tip. The pre-crack faces are coming into contact, and the curved pre-crack faces are being forced together by compressive loads acting in the x_1 direction. Consequently, the effective crack tip at early times is where the two faces initially come into contact and not at the actual initial pre-crack tip.

Because of the existence of the contact zone in this experiment, the shear band length, $R_{sb}(t)$ is defined here as the length of the fit Dugdale zone size, $R(t)$, less the contact zone length, $R_{cz}(t)$, which can be measured directly from the photographs. Hence,

$$R_{sb}(t) = R(t) - R_{cz}(t)$$

where the contact zone length is found by measuring the distance between the zero point indicated by the fringe pattern and the initial pre-crack tip and $R(t)$ is produced by the fit indicated in Eq (6.8). The pre-crack faces are in contact at t=26 μs ($c_d t/l = 2.3$), and the Dugdale fringe pattern indicates that the shear zone extends to the initial pre-crack tip at that time. Consequently, at time t=26 μs, $R_{sb}(t) = 0$, and from then on a shear band is observed.

Fits were performed for photos taken at the times 17–47 μs after impact. Photographs taken at earlier times either showed no loading or did not show enough loading to warrant a useful fit. An example of one of the fits (performed at 31.5 μs) can be found in Figure 6.9. Acceptable agreement between the theoretical Dugdale field and the experimentally measured field is seen.

The results of the fit for the shear stress on the shear band, $\tau_0(t)$, and for the shear band length, $R_{sb}(t)$ are plotted in Figure 6.10. The shear band length increases with time, and a linear fit of the growth provides an estimate of the shear band growth velocity of 320 m/s. The initiation occurs at approximately 26 μs, $c_d t/l = 2.3$, well

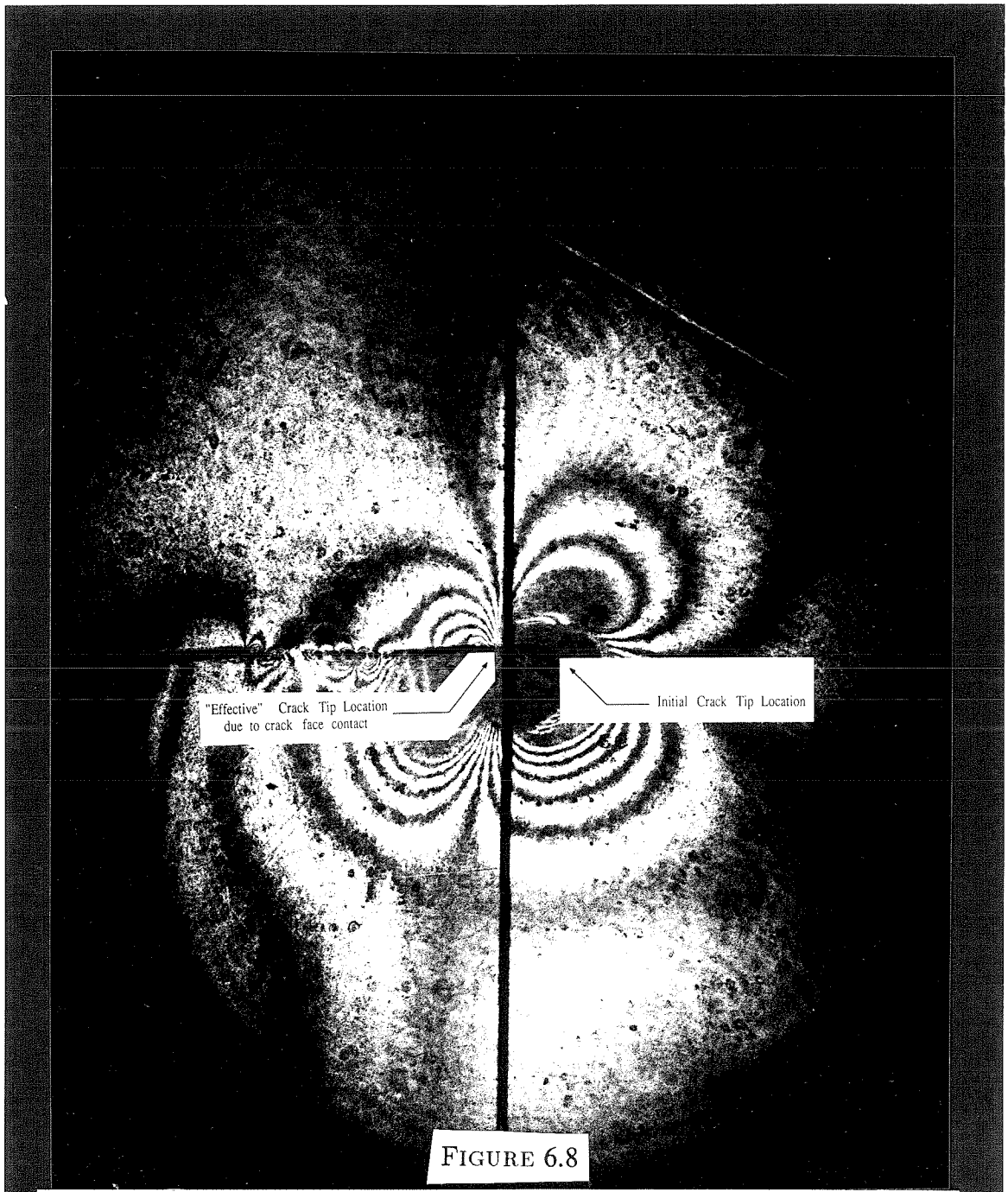

FIGURE 6.8

The actual initial crack tip, as indicated, and the "effective" initial crack tip can be seen in this photograph

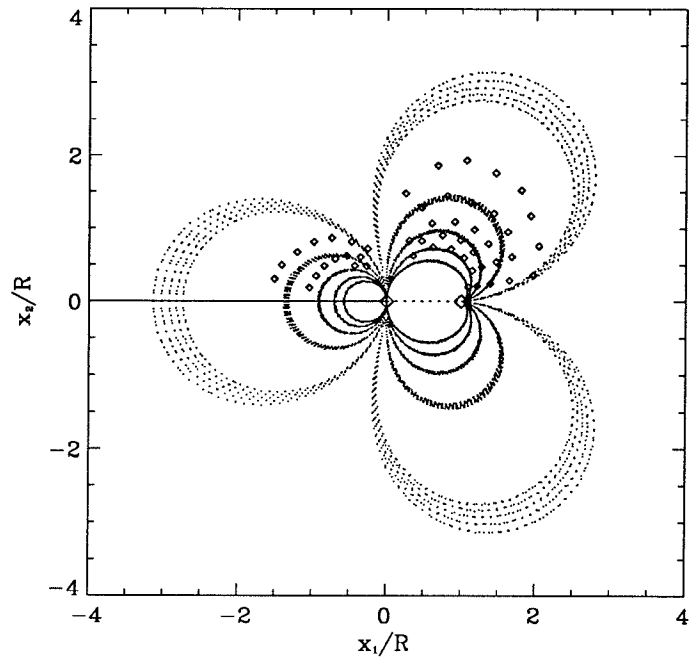

FIGURE 6.9 A check of the fitting procedure for t=31.5 μsData points should fall alternately on light and dark fringes in the figure. It can be seen that the fit is reasonably good for the forward fringe with less agreement found for the rear fringe.

within the domain of the Lee and Freund (1990) solution. At this time the stress intensity is roughly 140 $MPa\sqrt{m}$. The shear stress increases initially with time from 0.6 GPa to 1.6 GPa before the shear band initiation. It is assumed that this effect is due to increasing load on the pre-crack faces that are already in contact. After the shear band is initiated, the shear stress decreases from 1.6 GPa to 1.3 GPa. This type of behavior is expected since thermal softening is the acting mechanism by which the shear band forms. As the shear band grows it is expected that the shear stress decreases due to thermal softening. The value of the shear band length obtained from the fit described by equation (6.8) is compared to the estimated shear band length. This length is estimated from the photographs by comparing the recorded CGS fringe pattern to the predicted fringe pattern in Figure 6.2 as described in Section 6.2.1. Acceptable agreement is seen.

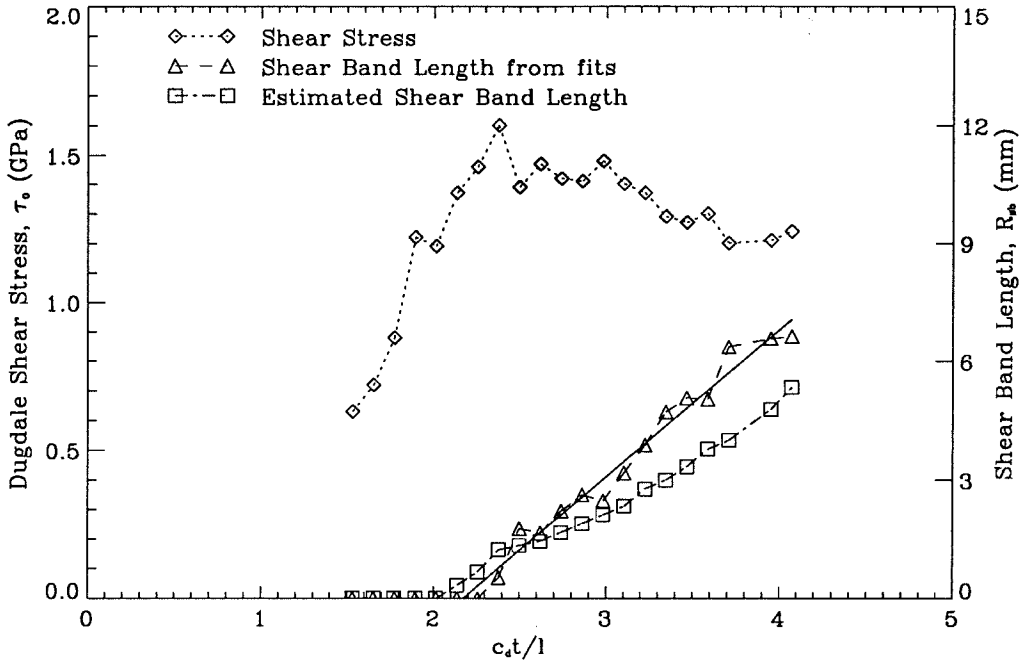

FIGURE 6.10 A plot of $\tau_0(t)$ and $R(t)$ as found from the fitting procedure in equation (6.8). The shear band length is compared to the length as estimated by comparing the fringe patterns in Figure 6.7 to the theoretical fringe pattern in Figure 6.2.

For comparison, the constitutive behavior of this material was measured and is shown in Figure 6.11 for various strain rates. The curves were measured in uniaxial compression, but, for ease of comparison, the equivalent shear stress is plotted using the Von Mises criterion. In high strain rate tests, the formation of shear bands in the specimen is observed. The material hardens with strain initially, but at higher strains thermal softening becomes dominant and the measured stress decreases with strain. This is typical observed behavior for the formation of instabilities in a uniaxial test. Examination of the specimens after testing shows unmistakable evidence of shear band failure. The maximum stress measured in the steel is 1.6 GPa for a test performed at 1000 s^{-1}, and good agreement is found between the measured shear stress for the shear band emanating from a pre-crack tip and the measured shear stress for a shear

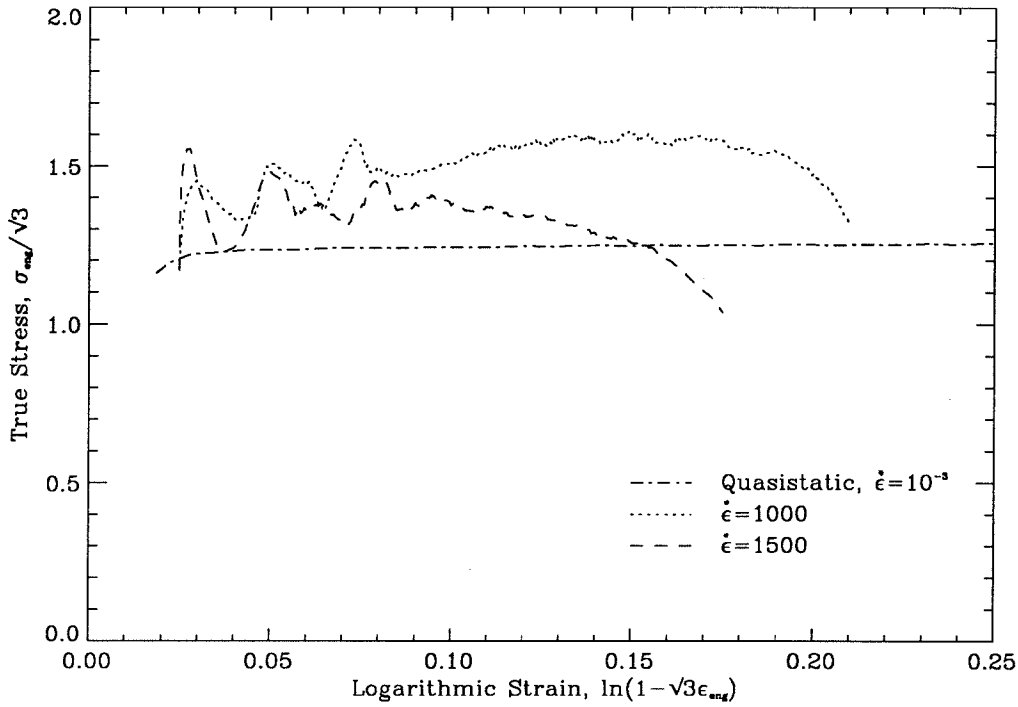

FIGURE 6.11 The constitutive behavior of C-300 at various strain rates as measured in compression. High strain rate data was measured using a Kolsky bar apparatus as shown in Chapter 4.

band formed in uniaxial dynamic compression.

6.4 Conclusions

The formation of a shear band at the tip of a pre-crack loaded dynamically in mode-II has been recorded using high-speed photography and the method of CGS to examine the stress field around the pre-crack tip. It is seen that the recorded fringe patterns around the pre-crack correspond well with the theoretical pattern for a mode-II Dugdale crack. Consequently, a fit of the digitized experimental fringe field is made to the Dugdale crack solution with the shear stress on the shear band as a variable parameter. The stress intensity factor is assumed to follow the model of Lee and Freund (1990). The results of the fits are used to extract the time evolution of the shear stress on the shear band and the length of the shear band with the following results:

It is seen that the shear band initiates within the regime of the Lee and Freund (1990) solution for this problem. However, it does not initiate at the first loading of the pre-notch tip. There is a time delay of approximately 11 μs before shear band growth is observed. The shear band initiates when $K_{II}^{d} = 140 MPa\sqrt{m}$.

The shear band propagates into the material with a speed of roughly 320 m/s while at the same time the shear stress on the shear band decreases from 1.6 GPa at initiation to 1.3 Gpa. The arrest of the shear band is not recorded.

References

1. J.Duffy (1984), Temperature measurements during the formation of shear bands in a structural steel, G.J. Dvorak and R.T. Shields, eds., *Mechanics of Material Behavior,* Elsevier Science Pub. B.V., Amsterdam, 75

2. F. Erdogan and G.C. Sih (1963), On the crack extension in plates under plane loading and transverse shear, *J. Basic Engineering,* **85**, 519

3. P. Hariharan, W. H. Steel and J.C. Wyant (1974), Double grating interferometer with variable lateral shear, *Optics Communications,* **11**, no. 3, 317

4. P. Hariharan and Z. S. Hegedus (1975), Double grating interferometers II. Application to collimated beams, *Optics Communications* **14**, no 1, 148

5. J.F. Kalthoff (1987), Shadow optical analysis of dynamic shear fracture, in: *SPIE Vol. 814 Photomechanics and Speckle Metrology,* 531

6. J.F. Kalthoff and S. Winkler (1987), Failure mode transition at high rates of shear loading, in: C.Y. Chiem, H.-D. Kunze and L.W. Meyer, eds., *Impact Loading and Dynamic Behaviour of Materials,* Verlag, Vol. 1, 185

7. S. Krishnaswamy, A.J. Rosakis and G. Ravichandran (1988), On the extent of dominance of asymptotic elastodynamic crack-tip fields 2. Numerical investigation of 3-dimensional and transient effects, Caltech Report SM88-21, (*J. Appl. Mech.,* **58,** 95)

8. Y.J. Lee (1990), Problems associated with dynamic fracture under high strain rate loading, Ph.D. Thesis, Division of Engineering, Brown University, Providence, RI

9. Y.J. Lee and L.B. Freund (1990), Fracture initiation due to asymmetric impact loading of an edge cracked plate, *J. Applied Mechanics,* **57**, 104

10. J.J. Mason, J. Lambros and A.J. Rosakis (1992), The use of a coherent gradient sensor in dynamic mixed-mode fracture mechanics experiments, *J. Mech. Phys. Sol.*, **40,** No. 3, 641

11. M.V.R.K. Murty (1978), Lateral shearing interferometers, in: D. Malacara, ed., *Optical Shop Testing,* J. Wiley & Sons, Ch. 4.

12. J. R. Rice (1968), *Fracture,* Volume II, Academic Press, New York, Ch. 3, 264

13. A.J. Rosakis (1993), Two optical techniques sensitive to gradients of optical path difference: The method of caustics and the coherent gradient sensor (CGS), in *Experimental Techniques in Fractures III,* J.S. Epstein, Ed., Society for Experimental Mechanics, Inc., Bethel, CT, Ch. 10

14. A.J. Rosakis and K. Ravi-Chandar (1986), On crack-tip stress state: an experimental evaluation of three-dimensional effects, *Int. J. Solids & Structures,* **22,** 121

15. H.V. Tippur, S. Krishnaswamy and A.J. Rosakis (1989a), A coherent gradient sensor for crack tip deformation measurements: analysis and experimental results, Caltech SM-Report 89-1, (*Int. J. Fracture,* **48,** 193)

16. H.V. Tippur, S. Krishnaswamy and A.J. Rosakis (1989b), Optical mapping of crack tip deformations using the methods of transmission and reflection coherent gradient sensing: a study of crack tip K-dominance, Caltech Report SM89-11, (*Int. J. Fracture,* **52,** 91).